Measurement of Tensile Forces in *Xenopus laevis* Neural Tissue

by

Paul Lee

A thesis

presented to the University of Waterloo

in fulfillment of the

thesis requirement for the degree of

Master of Science

in

Biology

Waterloo, Ontario, Canada, 2009

©Paul Lee 2009

I hereby declare that I am the sole author of this thesis. This is a true copy of the thesis, including any required final revisions, as accepted by my examiners.

I understand that my thesis may be made electronically available to the public.

Abstract

Neurulation is critical for the proper development of the central nervous system during embryogenesis. This process requires coordinated morphogenetic movements driven by localized cell movements. The key morphogenetic process responsible for lengthening the neural plate is convergent extension. During convergent extension medially oriented cell polarity, protrusive activity, and motility are thought to generate forces through cell intercalation resulting in stiffer elongating tissues. My research determines that forces that help shape the neural plate arise from morphogenetic movements in the neural tissue and determines PCP signaling regulates tissue stiffness in the neural ectoderm. We have established an experimental system sensitive enough to evaluate the stiffness of *Xenopus* neural tissue. Stiffness is measured by gluing two fine wires onto neural explants from an early gastrula stage *Xenopus laevis* embryo. The wires stretch the tissue at a constant strain rate using a real-time image-based feedback system and stiffness is determined by measuring the deflection of one wire. Measurements obtained from control embryos prior to neurulation estimate tissue stiffness at approximately 12.7 ± 0.53 mN/m in both mediolateral and anteroposterior directions. Stiffness measurements double in early neurula embryos ($P < 0.05$). Mediolateral stiffness, 24.9 ±6.2 mN/m, is significantly greater than anteroposterior stiffness, 21.4 ±5.3 mN/m ($P < 0.05$). These trends are strengthened in normalized data to reduce clutch-to-clutch variation. Expressions of dominant-negative *Wnt11*, *Fz7*, and *Dsh* constructs successfully disrupt neurulation by interfering with the PCP pathway. Changes in stiffness of the neural plate were measured and show reduced stiffness at early neurula stage in both mediolateral and anteroposterior directions suggesting mechanical forces are generated within the neural plate.

Acknowledgements

I am sincerely thankful to my supervisor, Dr. Mungo Marsden, for giving me the opportunity to work in his laboratory. I am grateful for your knowledge, support, and utmost patience during my project. Thank you for your guidance as my supervisor in life and in the lab. I will cherish our friendship - thank you for all the laughs. It has been a wonderful experience.

I am also thankful to my co-supervisor, Dr. Wayne Brodland, for giving me the opportunity to experience such a unique research project with engineering. Thank you for your knowledge and support.

I am grateful to my committee members, Dr. Brian Dixon and Dr. Heidi Engelhardt, for their time and patience. Thank you for your valuable suggestions and guidance.

A huge thank you to Caleb Horst for guiding me every step of the way during my project especially in designing the device as well as helping with data analysis. Thank you for your patience in my endless questions. You have really helped me grasp engineering concepts that were alien to me.

I also thank my lab mates, especially Catherine Suckert for her friendship. You always made my day enjoyable in the lab. Thank you for your motivation and guidance in teaching courses and learning new concepts.

I thank my family for their love and support, including the constant worries. I thank my parents-in-law who have been very loving and trusting. I especially thank my newlywed wife, Sunny Cho, who I love dearly and has made my life so memorable especially during these past couple years. Thank you for your love and support always.

Table of Contents

Author's Declaration ii

Abstract iii

Acknowledgements iv

Table of Contents v

List of Figures vii

List of Tables ix

List of Abbreviations xi

Chapter 1: Introduction 1

  1.1 Biomechanics and Morphogenesis 1

  1.2 *Xenopus laevis* Neurulation 1

    1.2.1 Cell Shape Change: Apical Constriction 2

    1.2.2 Cell Movement: Convergent Extension 7

  1.3 Biomechanics of Convergent Extension 15

  1.4 Molecular Control of Convergent Extension: The Planar Cell Polarity (PCP) Pathway 19

  1.5 Experimental Rationale 23

Chapter 2: Methods and Materials 24

  2.1 *Xenopus laevis* Embryos 24

  2.2 Microinjection and Dominant-negative Injected Emrbryos 24

  2.3 Microsurgery 25

  2.4 Apparatus Design and Tensile Measurement 29

  2.5 Data Analysis 33

Chapter 3: Results 35

  3.1 Device Modifications 35

3.1.1 Selection of Adhesives 35
3.1.2 Types of Wires 38
3.2 Preliminary Tests 41
3.3 Sources of Error and Variability 46
3.3.1 The Effects of Wound Healing 46
3.3.2 Slope Determination 53
3.3.3 Clutch-to-Clutch Variability 55
3.3.4 Limitations of TissueGUI 55
3.4 Results 62
3.4.1 TissueGUI2 62
3.4.2 Phase A Stiffness Measurements in Wild Type Emrbyos 65
3.4.3 Phase B Stiffness and Decay 68
3.4.4 Regulation of Tissue Stiffness by the PCP Signaling Pathway 74
Chapter 4: Discussion 95
4.1 Device Optimization 95
4.2 Experimental Parameters 97
4.3 Directional Stiffness of the Neural Plate 101
4.4 PCP Affects Neural Plate stiffness 105
4.5 Conclusion 109
4.6 Future Directions 109
Appendix A: Raw Data 110
References 129

List of Figures

Figure 1.1 Morphogenetic movements of *Xenopus laevis* neurulation 3

Figure 1.2 Mechanisms for cell wedging during apical constriction 5

Figure 1.3 Radial and mediolateral cell intercalation 9

Figure 1.4 Cell intercalation in the dorsal mesoderm 11

Figure 1.5 Cell intercalation in the neural plate 13

Figure 1.6 Biomechanics of tractive and stiffening adhesions during cell intercalation 17

Figure 1.7 Canonical and Non-canonical Wnt pathways 21

Figure 2.1 Isolation of deep neural over mesoderm explants 27

Figure 2.2 Experimental equipment and setup 31

Figure 3.1 Patterns of cured cyanoacrylate glue on tungsten wires versus stainless steel wires 39

Figure 3.2 Calculation of stiffness with stress (tensile) versus strain graphs. 42

Figure 3.3 Average stiffness of *Xenopus* deep neural and neural tissue explants at different development stages. 44

Figure 3.4 Wound healing 47

Figure 3.5 Tisues stiffness during wound healing 49

Figure 3.6 High programmed strain rates remove the effects of wound healing 51

Figure 3.7 Determining slope on stress versus strain plots 56

Figure 3.8 Evidence for clutch-to-clutch variability 58

Figure 3.9 Directional stiffness of stage 11 and 13 embryos 60

Figure 3.10 Sample data obtained using TissueGUI2 63

Figure 3.11 Tissue stiffness increases with developmental stage 66

Figure 3.12 Phase B tissue stiffness measured at 190 seconds 70

Figure 3.13 Tissue stiffness decay in phase B 72

Figure 3.14 Phenotypes of early neurula stage embryos expressing dominant-negative PCP pathway constructs 75

Figure 3.15 Phenotypes of late neurula stage embryos expressing dominant-negative PCP pathway constructs 77

Figure 3.16 The effects of a dn*XDsh* construct on tissue stiffness 87

Figure 3.17 The effects of a dn*XFz7* construct on tissue stiffness 89

Figure 3.18 The effects of a dn*XWnt11* construct on tissue stiffness 91

Figure 3.19 Average ML and AP stiffness of explants obtained from embryos with disrupted PCP signaling 93

Figure A1.1 Average Phase A stiffness of explants at stage 11 and 13 in ML and AP directions 111

Figure A1.2 Average Phase B (190 seconds) stiffness of explants at stage 11 and 13 in ML and AP directions 114

Figure A1.3 Average decrease in stiffness between 45 and 190 seconds of explants at stage 11 and 13 in ML and AP directions 117

Figure A2.1 Average stiffness measured from dn*XDsh* injected embryos compared to sibling controls 121

Figure A2.2 Average stiffness measured from dn*XFz7* injected embryos compared to sibling controls 124

Figure A2.3 Average stiffness measured from dn*XWnt11* injected embryos compared to sibling controls 127

List of Tables

Table 3.1 Relative viscosity, cure time, and strength of attachment of wires to tissue explants of several types of adhesives 37

Table 3.2 Average stiffness from 0 to 2% strain and 2 to 8% strain of tests run at a strain rate of 200%/hr 54

Table 3.3 Average and normalized phase A stiffness measurements of explants at stage 11 and 13 in ML and AP directions 65

Table 3.4 Average and normalized phase B stiffness measurements taken at 190 seconds of explants at stage 11 and 13 in ML and AP directions 68

Table 3.5 Average and normalized decrease in stiffness between 45 and 190 seconds of explants at stage 11 and 13 in ML and AP directions 69

Table 3.6 The effects of a dn*XDsh* construct on tissue stiffness 80

Table 3.7 The effects of a dn*XFz7* construct on tissue stiffness 81

Table 3.8 The effects of a dn*XWnt11* construct on tissue stiffness 83

Table 3.9 Average ML stiffness of explants obtained from embryos with disrupted PCP signaling 84

Table 3.10 Average AP stiffness of explants obtained from embryos with disrupted PCP signaling ... 86

Table A1.1 Average Phase A stiffness of explants at stage 11 and 13 in ML and AP directions by clutch 110

Table A1.2 Average Phase B (190 seconds) stiffness of explants at stage 11 and 13 in ML and AP directions by clutch 113

Table A1.3 Average decrease in stiffness between 45 and 190 seconds of explants at stage 11 and 13 in ML and AP directions by clutch 116

Table A2.1 The effects of a dn*XDsh* construct on tissue stiffness by clutch 119

Table A2.2 The effects of a dn*XFz7* construct on tissue stiffness by clutch 123

Table A2.3 The effects of a dn*XWnt11* construct on tissue stiffness by clutch 126

List of Abbreviations

AP	Anteroposterior, referring to the anterior-posterior or rostral-caudal axis
CE	Convergent extension, the active medial-lateral intercalation of neuroepithelium and dorsal mesoderm that extends the embryo in the anterior-posterior axis
DFA	Danilchik's for Amy solution
MBS	Modified Barth's Solution
ML	mediolateral, referring to the medial-lateral axis
PCP	Planar Cell Polarity (Non-canonical Wnt signaling)
Stiffness	The ability to resist deformation, specifically the ability of a material to resist changes in length when under lengthwise tension or compression, used generically to encompass both structural and material stiffness ***Structural stiffness*** – a geometry dependent term calculated as the change in force over the change in length. Used to compare different structures of the same type ***Material stiffness*** – a geometry independent term generally referring to Young's Modulus. Used to compare different materials regardless of the type and geometry of the structures they are part of
Strain (ε)	A geometry independent measure of deformation, calculated as the change in length divided by original length for uniaxial tests. This term is expressed as a percentage or decimal fraction

Strain Rate	The rate of change of strain, calculated as the change in strain divided by the elapsed time
Stress (σ)	A geometry independent term calculated as the magnitude of the applied force divided by the area of the surface over which the force is applied. The SI unit for stress is Pascals (Pa) which is equivalent to one Newton of force per square meter (N/m^2)
Tension (tensile force)	The magnitude of pulling force on a material imposed by an outside object, measured in Newtons and is always parallel to the object on which it applies (opposite of compression)
Young's Modulus (*E*, modulus of elasticity)	A measure of stiffness that describes the elastic properties of a solid undergoing uniaxial compression or tension measured in Pa or N/m^2. It is the ratio of the uniaxial stress over the uniaxial strain and can be experimentally determined from the slope of a stress-strain curve created during tensile tests conducted on a sample of material

Chapter 1

Introduction

1.1 Biomechanics and Morphogenesis

Morphogenesis is the rearrangement of cells and tissues to generate embryonic form. Morphogenesis is driven by changes in cell shape, cell adhesion, and cell migration. Cell rearrangements generate physical forces that lead to the mechanical deformations and bulk movement of tissues necessary for shaping the embryo (Trinkaus, 1984). The mechanical properties of tissues determine how tissues deform or resist deformation in response to generated forces. Biomechanics studies how these forces are generated and how they affect the mechanical properties of tissues. By studying the mechanical properties of tissues in conjunction with molecular manipulations that disrupt development we can describe how individual molecules contribute to the process of morphogenesis.

1.2 *Xenopus laevis* Neurulation

During chordate embryogenesis, neurulation is the major morphogenetic event crucial for development of the central nervous system. In *Xenopus* neurulation begins with the thickening of the neuroepithelium, the inner layer of the dorsal ectoderm, to form the neural plate (Fig. 1.1A). Bending of the neural plate along the lateral margins, the lateral hingepoints, elevates the neural folds (Fig. 1.1B). Cell intercalation then draws the neural folds toward the midline, assisted by bending along the medial hingepoint (Fig. 1.1C). As the neural folds move medially, the neural plate and dorsal mesoderm narrow and lengthen along the anterior-posterior axis. The neural folds subsequently meet at the midline and fuse to form a hollow neural tube (Wallingford, 2005, Fig.

1.1D). Apical constriction and cell intercalation are the primary morphogenetic processes responsible for generating the forces that bend, narrow, and lengthen the neural plate.

1.2.1 Cell Shape Change: Apical Constriction

Neural plate bending requires apical constriction of epithelial cells at the lateral and medial hingepoints. The molecular mechanism behind apical constriction is best described in *Drosophila melanogaster.* In *Drosophila* ventral mesoderm apical constriction is coordinated by actin-myosin contractile rings in conjunction with increased cell-cell adhesion at the apical surface (Fig. 1.2 A, B) (Barmchi et al, 2005; Kolsch et al, 2007). As the apical surface of the cells shrink, the cells become wedge shaped. Increased apical lateral adhesion keeps the cells tightly adherent and the changes in cell shape bend the tissue. While the molecular basis of apical constriction is not well characterized, there is evidence in vertebrates that both the contraction of the cytoskeleton and accumulation of actin at the apical surface are tightly regulated. In mouse neural tissue, integrin activation activates *p190Rho*GAP regulation of the small GTPase *Rho* through GTPase activating proteins (GAPs) leading to actin polymerization and cadherin-mediated cell-cell adhesions. S*hroom* is an actin binding protein required for apical actin accumulation. The over-expression of *shroom* induces ectopic apical actin accumulation and subsequent apical constriction (Haigo et al, 2003). Deletion mutations of *p190Rho*GAP and *shroom* genes result in the failure of neural plate bending and neural tube closure in *Xenopus* (Brouns et al, 2000; Haigo et al, 2003). In addition, basal localization of nuclei and active apico-basal microtubule elongation may also contribute to apical constriction by allowing cytoplasm to bulge basally away from the shrinking apical surface (Fig. 2 C) (Lawson et al, 2001; Wallingford, 2005).

Figure 1.1 **Morphogenetic movements of *Xenopus laevis* neurulation.** (A) Thickening of the neuroepithelium to form the neural plate with overlying epithelium and underlying prenotochord mesodermal cells (pink). (B) Lateral hingepoint bending and elevation of the neural folds. (C) Neural folds migrate medially toward the midline assisted by medial hingepoint bending. (D) Neural folds meet at the midline and fuse to form a hollow neural tube. (modified from Wallingford, 2005)

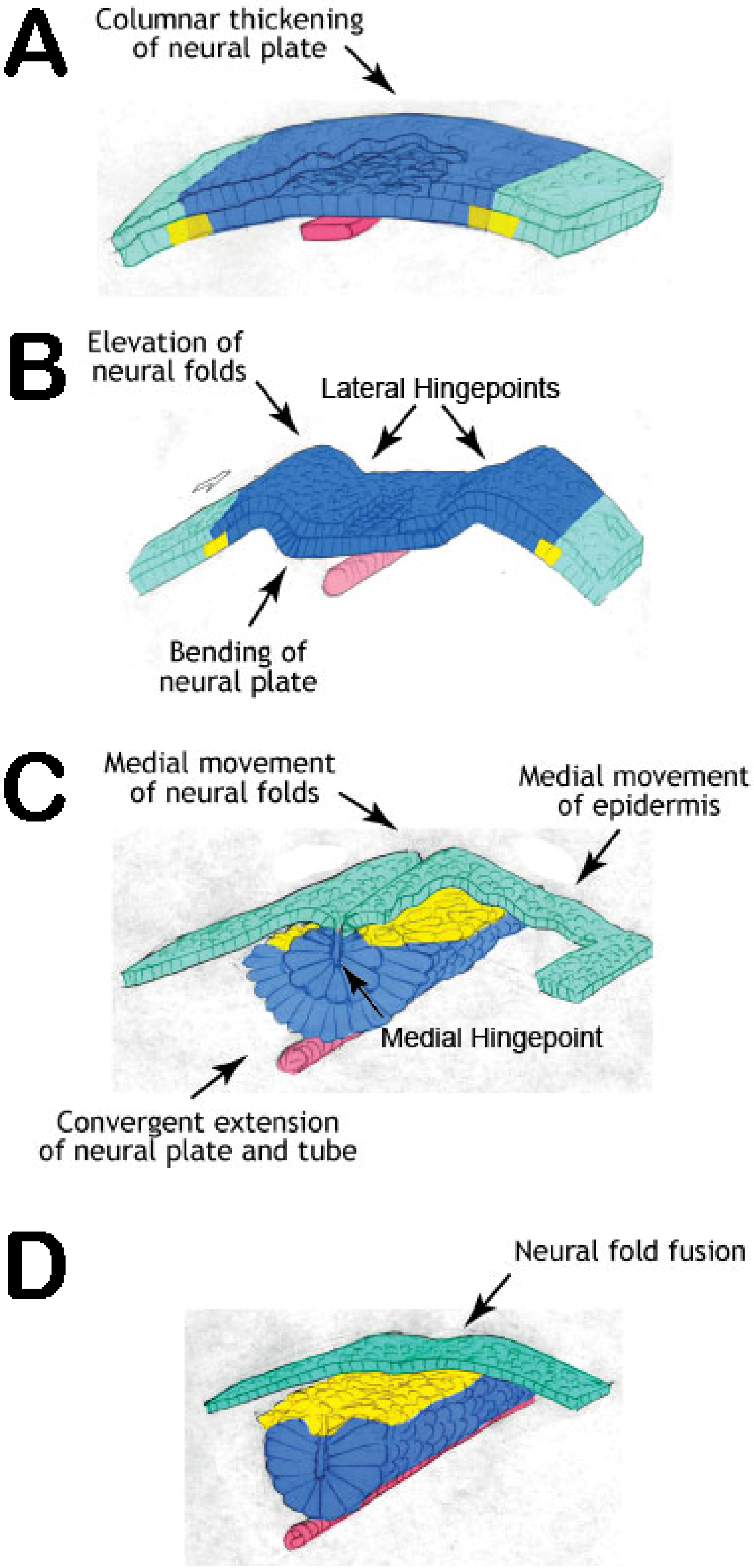
A
Columnar thickening of neural plate
B
Elevation of neural folds
Lateral Hingepoints
Bending of neural plate
C
Medial movement of neural folds
Medial movement of epidermis
Medial Hingepoint
Convergent extension of neural plate and tube
D
Neural fold fusion

Figure 1.2 Mechanisms for cell wedging during apical constriction. (A) Apical constriction occurs through actin-myosin contraction (green) at the apical surface. (B) Tissue bending may be assisted by increased inter-cellular adhesion (red) at the apical lateral surface as cells change shape. (C) Increases in cell height may also assist in cell wedging as apico-basal microtubules elongate (blue) to shift the nuclei and cytoplasm basally. (Wallingford, 2005)

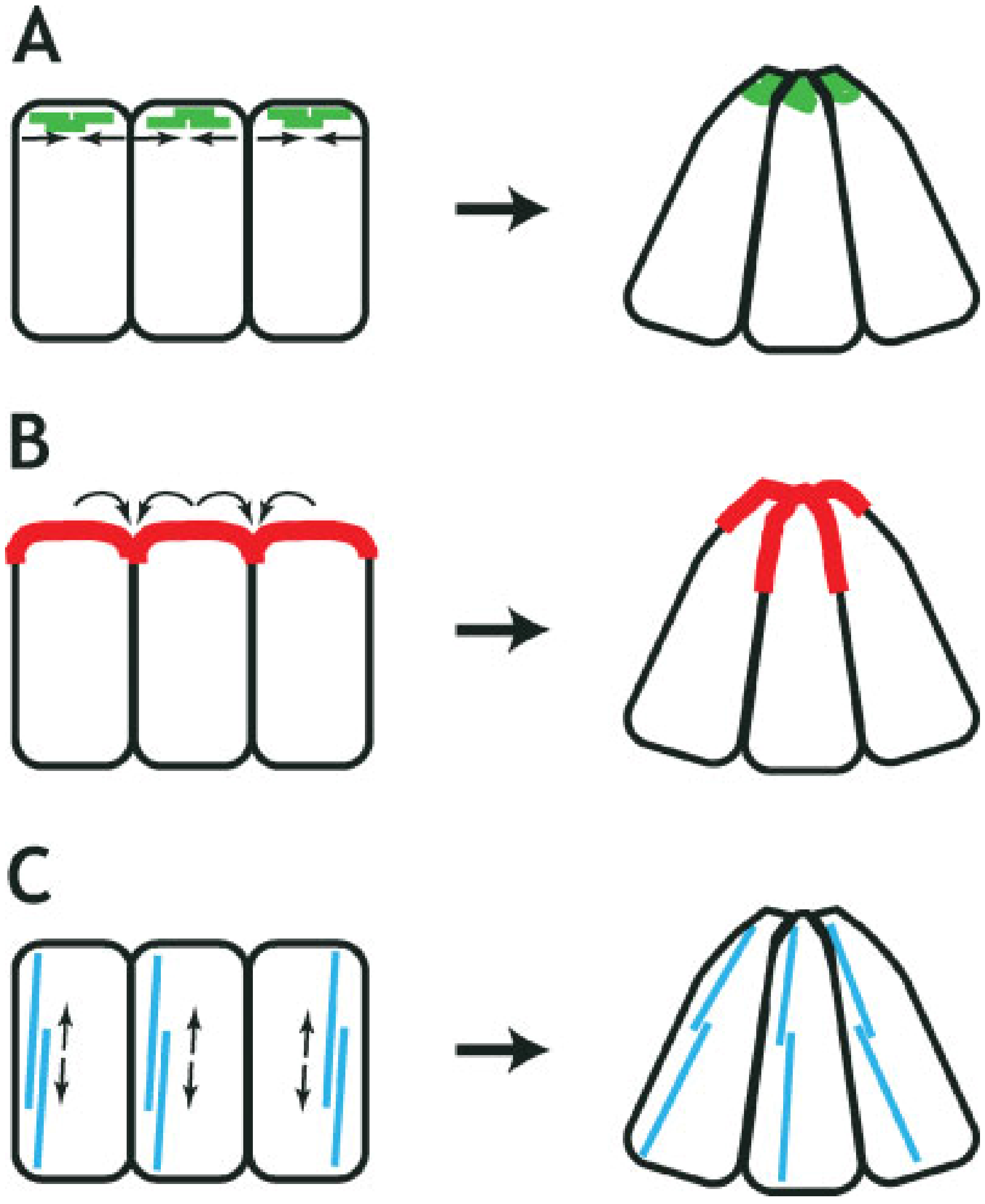
A
B
C

1.2.2 Cell Movement: Convergent Extension

Convergent Extension (CE) is the morphogenetic process responsible for drawing the neural folds towards the midline. CE occurs by the active intercalation of cells to narrow and lengthen a tissue (Fig. 1.3). During CE, cells intercalate in both radial and mediolateral directions (Fig. 1.3). Radial intercalation drives epiboly, the thinning of multilayered tissues, and is responsible for increasing the area of the ectoderm during early *Xenopus* gastrulation (Fig. 1.3A) (Marsden and DeSimone, 2001; Keller et al, 2008). Radial intercalation precedes mediolateral intercalation in both the mesoderm and the neural plate, but both processes cannot be identified as a distinct morphogenetic process in these tissues. During mediolateral CE, an oriented field of cells intercalates to form a mediolateral narrow (convergent) and elongated (extension) tissue (Fig. 1.3B).

In *Xenopus*, CE is well described in the dorsal mesoderm where cells develop bipolar mediolateral lamellipodial protrusions (Fig. 1.4). The lamelliform protrusions bind to adjacent cells and through traction pull the lateral margins of the field of cells medially. During this process cells intercalate among their neighbours, resulting in axial extension. CE in the dorsal mesoderm is thought to be primarily responsible for the forces that drive axial extension of the embryo.

In the lateral neural plate, CE occurs via a slightly different mechanism. Cells are monopolarized and intercalate towards the embryonic midline. Similar to what is observed in the mesoderm, this process results in mediolateral (ML) narrowing and anteroposterior (AP) axial elongation (Fig. 1.5) (Davidson and Keller, 1999; Elul and Keller, 2000). Interestingly, cells at the neural plate midline are pleomorphic. Pleomorphic cells exhibit randomized lamelliform protrusions and do not undergo CE (Fig. 1.5). This region is known as the notoplate and during neurulation neural plate and notoplate cells do not mix. The notoplate has been observed to undergo dramatic axial elongation in association with CE in the underlying mesoderm (Ezin et al, 2003, 2006). At this time, it remains unclear if CE in the neural tissue produces the forces that result in axial extension of the neural plate.

Figure 1.3 Radial and mediolateral cell intercalation. (A) Radial intercalation of multi-layered cells increases surface area of tissues. (B) Mediolateral intercalation of cells mediolaterally narrows tissues causing anteroposterior extension. (modified from Keller et al, 2008)

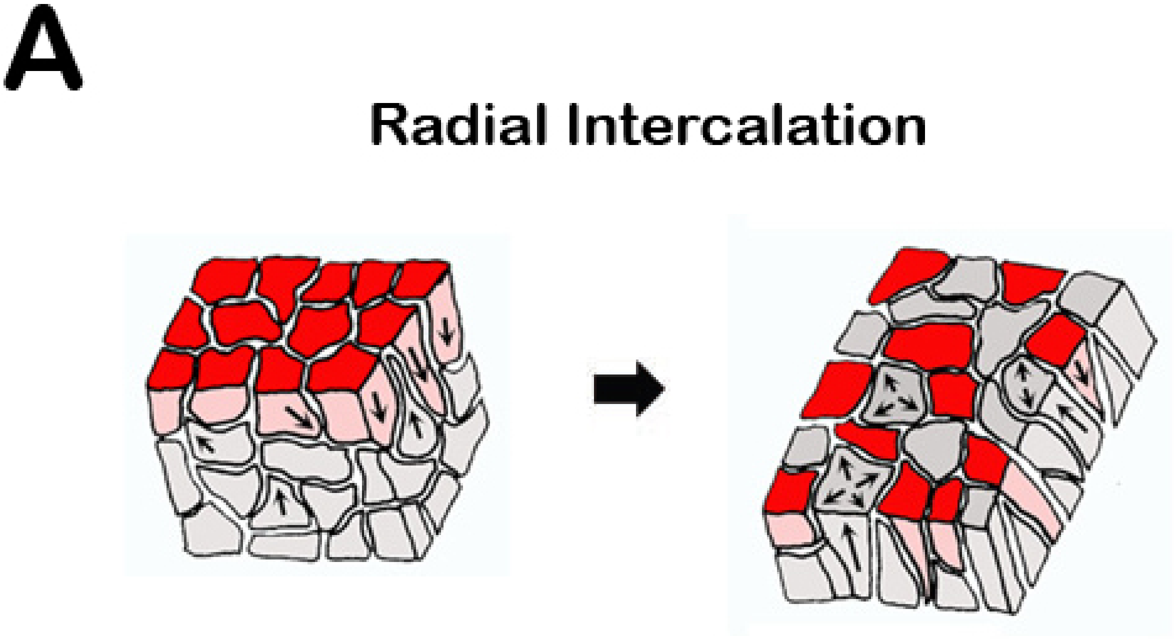
A
Radial Intercalation

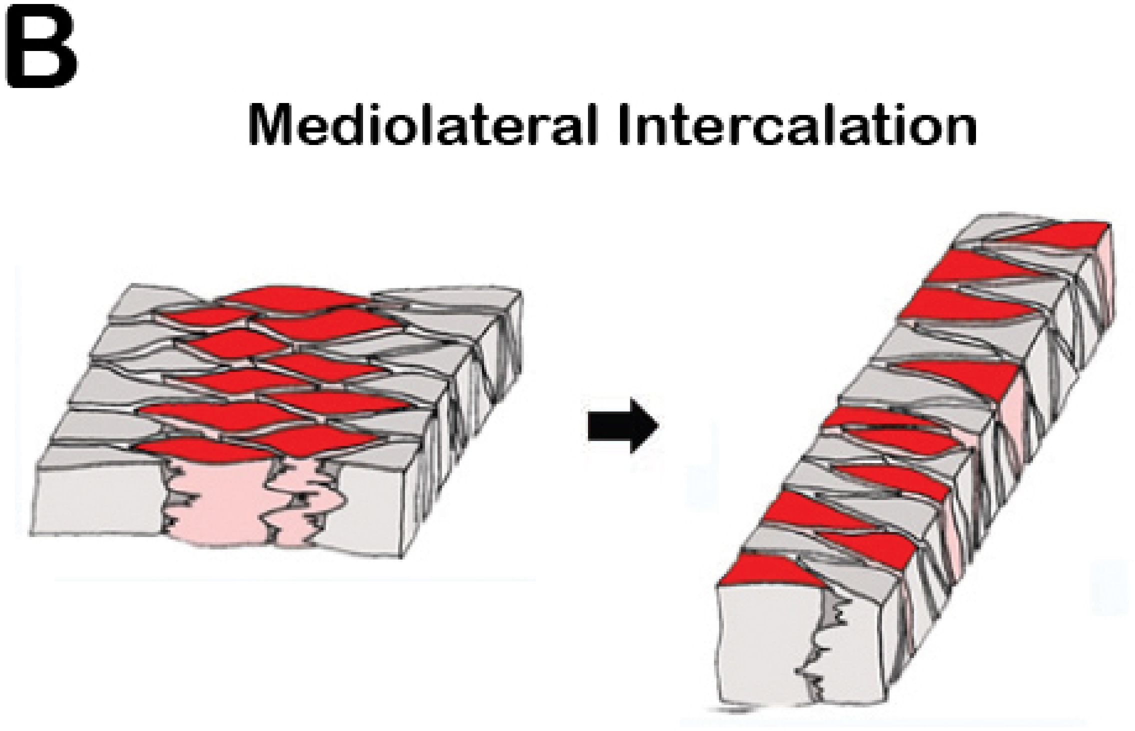
B
Mediolateral Intercalation

Figure 1.4 Cell intercalation in the dorsal mesoderm. (A)Multi-directional lamellipodia (red) of pleomorphic cells before polarization. (A) Bipolarized lamellipodia (red) concentrate at the mediolateral ends of dorsal mesodermal cells. The dark arrows indicate the direction of mediolateral convergence that causes anteroposterior extension (large grey arrows). (modified from Keller et al, 2000)

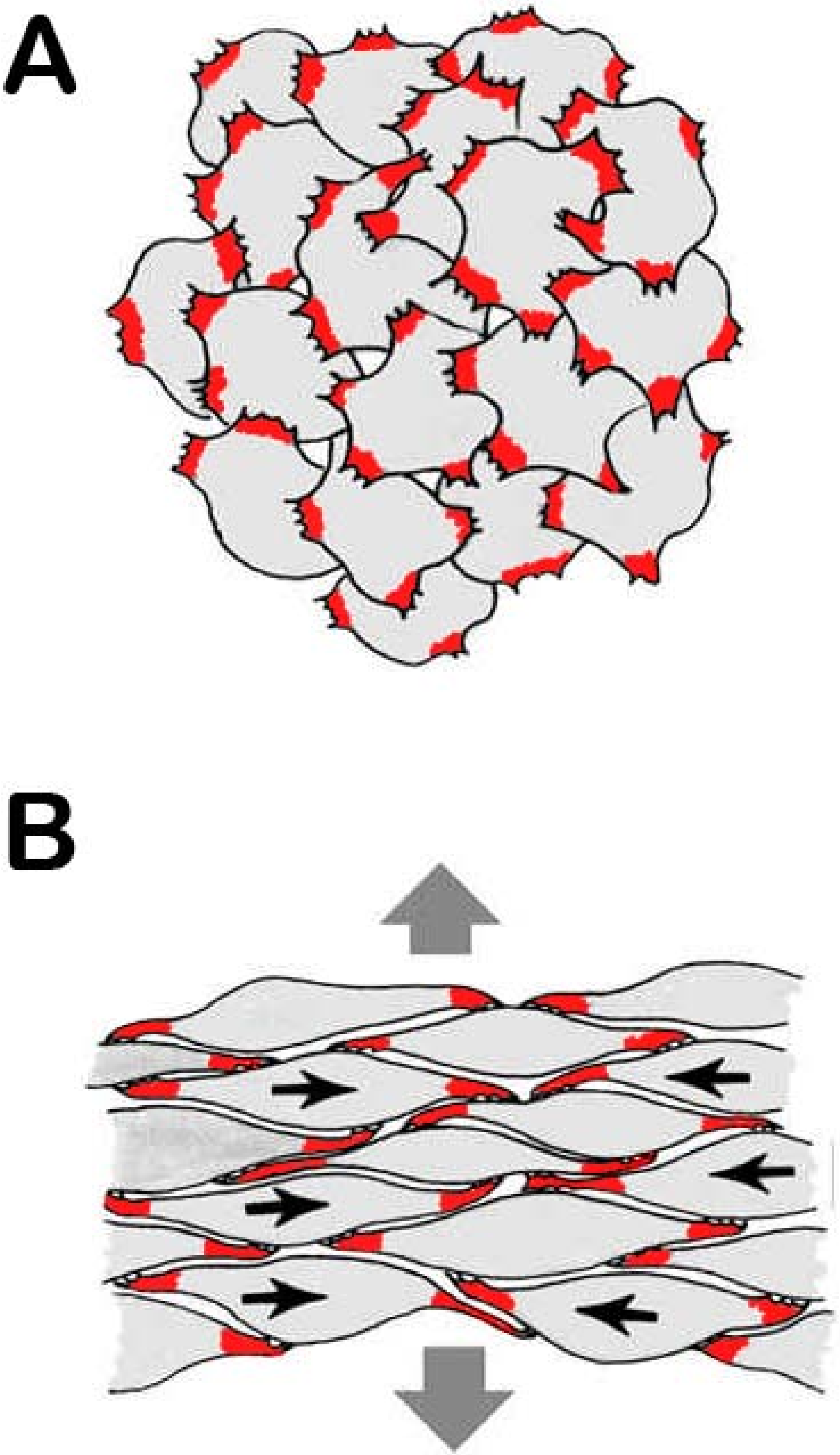
A
B

Figure 1.5 Cell intercalation in the neural plate. Lamellipodia (red) of neural plate cells are monopolarized and move toward the notoplate where cells remain pleomorphic. The dark arrows indicate medial migration of the cells causing anteroposterior extension (large grey arrows). (modified from Keller et al, 2000)

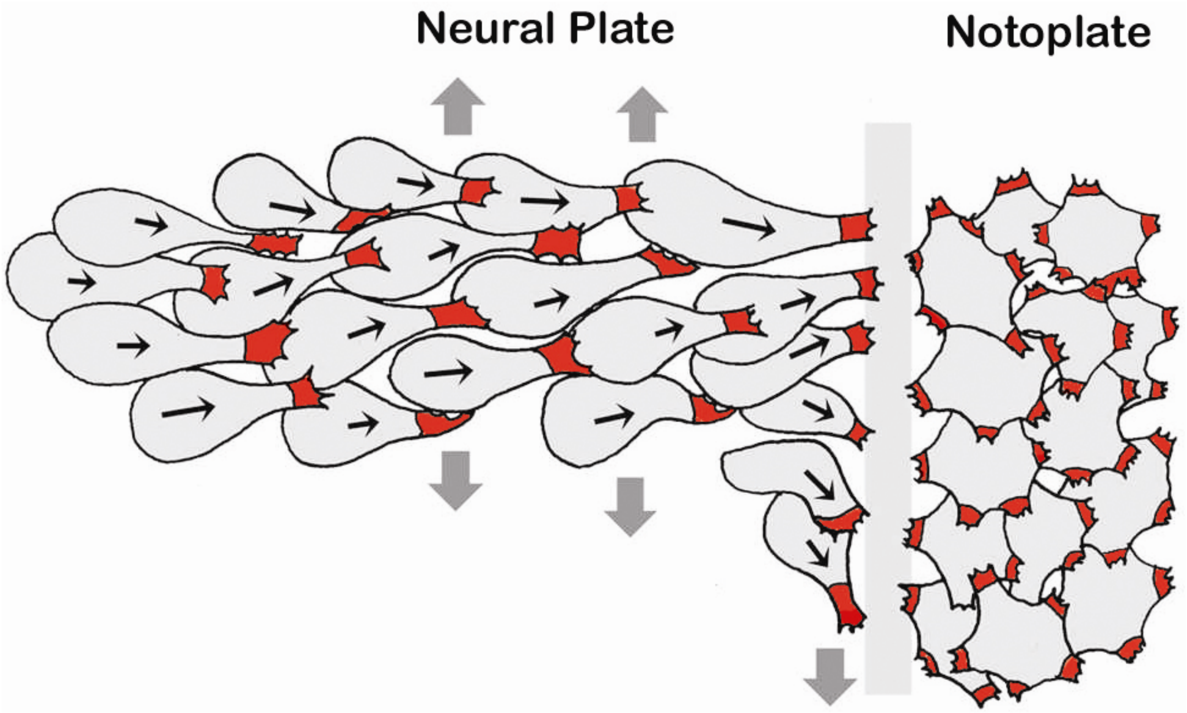
Neural Plate
Notoplate

1.3 Biomechanics of Convergent Extension

It has been demonstrated that tissues undergoing CE produce considerable pushing forces (Moore et al, 1994). The biomechanical forces resulting from CE are generated only through the intercalation of cells (Keller and Danilchik, 1988). Biomechanical investigations on tissues during neurulation are focused on only those tissues that exhibit CE.

In tissues undergoing CE, cells send out lamellipodia that adhere and pull against neighboring cells. As a consequence of these pulling forces, dorsal mesodermal cells have been observed to elongate with an aspect ML ratio of about 2.5 to 3 (Shih and Keller, 1992). Indeed, complex computational modeling has shown that lamellipodia have the mechanical capacity to cause cell intercalation and give rise to cell elongation (Brodland, 2006; Brodland and Veldhuis, 2006). Cells undergoing CE are under considerable tensile stress. The elastic properties of the cellular cytoskeleton generate tension by resisting elongation of the cell (depicted as springs, Fig. 1.6 A, B). Actin-myosin mediated contraction of the cytoskeleton is also believed to further limit elongation and increase tension. Recent research shows that Myosin IIB, a cytoskeletal non-muscle myosin II, not only cross-links actin filaments to maintain cortical integrity and stiffness, but also generates contraction by moving along the cortical actin cytoskeleton in the dorsal mesodermal cells of *Xenopus* embryos (Skoglund et al, 2008; Rolo et al, 2009). Cortical contraction resists stretching during CE and creates tension. The proposed model that interfacial tension of tissues is attributed to cell-cortex tension is coined as the 'Differential Interfacial Tension Hypothesis' (Brodland, 2002). The summation of the tension in these cells results in an increase in the mechanical stiffness (the ability to resist deformation) of the tissue. Dorsal mesoderm explants undergoing CE increase in stiffness by a factor of 3 to 4 times in the anterior-posterior axis during early gastrulation, between stage 10+ and 11.5, from 3 N/m^2 to 10 N/m^2 (Moore et al, 1995) and increases of more than six-fold from 13 to

85 N/m^2 between the late-gastrula (stage 13) and early neural tube stage (stage 22) (Zhou et al, 2009).

One of the puzzles of CE is how tissue stiffness increases while cells are actively intercalating. This can be explained through the dynamic turnover of cell adhesions. Lamellipodia bind to the rigid surface of adjacent cells through small contact points called ‘tractive protrusions’ (red, Fig. 1.6C). Turnover of tractive protrusions on adjacent cells allow lamellipodia to pull cells past one another. These adhesions generate tension in the cells and stiffness the tissues. At the same time, turnover of cell-cell ‘stiffening adhesions’ (green, Fig. 1.6A, B, D) allow cells to shear past each other and maintain stiffness throughout the entire tissue (Keller et al, 2000). These cell-cell adhesions may actually be downregulated (not in amount) by decreases in the dominant cadherin, C-cadherin, activity and if the decrease is blocked, CE fails (Brieher and Gumbiner, 1994; Zhong et al, 1999). The difference in tissue tension attributed to the quantitative and qualitative differences in intercellular adhesion is known as the ‘Differential Adhesion Hypothesis’ (Foty and Steinberg, 2005). The dynamic turnover of both the tractive protrusions and stiffening adhesions allows the intercalation of cells while increasing the stiffness of tissues undergoing CE.

Figure 1.6 Biomechanics of tractive and stiffening adhesions during cell intercalation. (A) Dorsal mesodermal cells are held in an array of bipolarized lamelliform 'tractive protrusions' (red) and cell to cell 'stiffening adhesions' (green). Tension held within the elastic properties of the cytoskeleton of the cells is depicted as springs. (B) Similarly, neural plate cells are held in an array of monopolarized lamelliform tractive protrusions (red) and cell to cell stiffening adhesions (green). Tension held within the elastic properties of the cytoskeleton of the cells is depicted as springs. (C) The tension is generated by the polarized protrusive activity (grey arrow) of the lamelliform protrusion (light red) on adjacent cells. Tension is transmitted across the cell membrane to the cytoskeleton. Dynamic turnover of the tractive protrusions (dark red) allow cells to shear past each other while sustaining tensions throughout the tissue. (D) The dynamic turnover of stiffening adhesions (green) between cells also allows cells to pass each other during intercalation in a stiffening tissue. (modified from Keller et al, 2003)

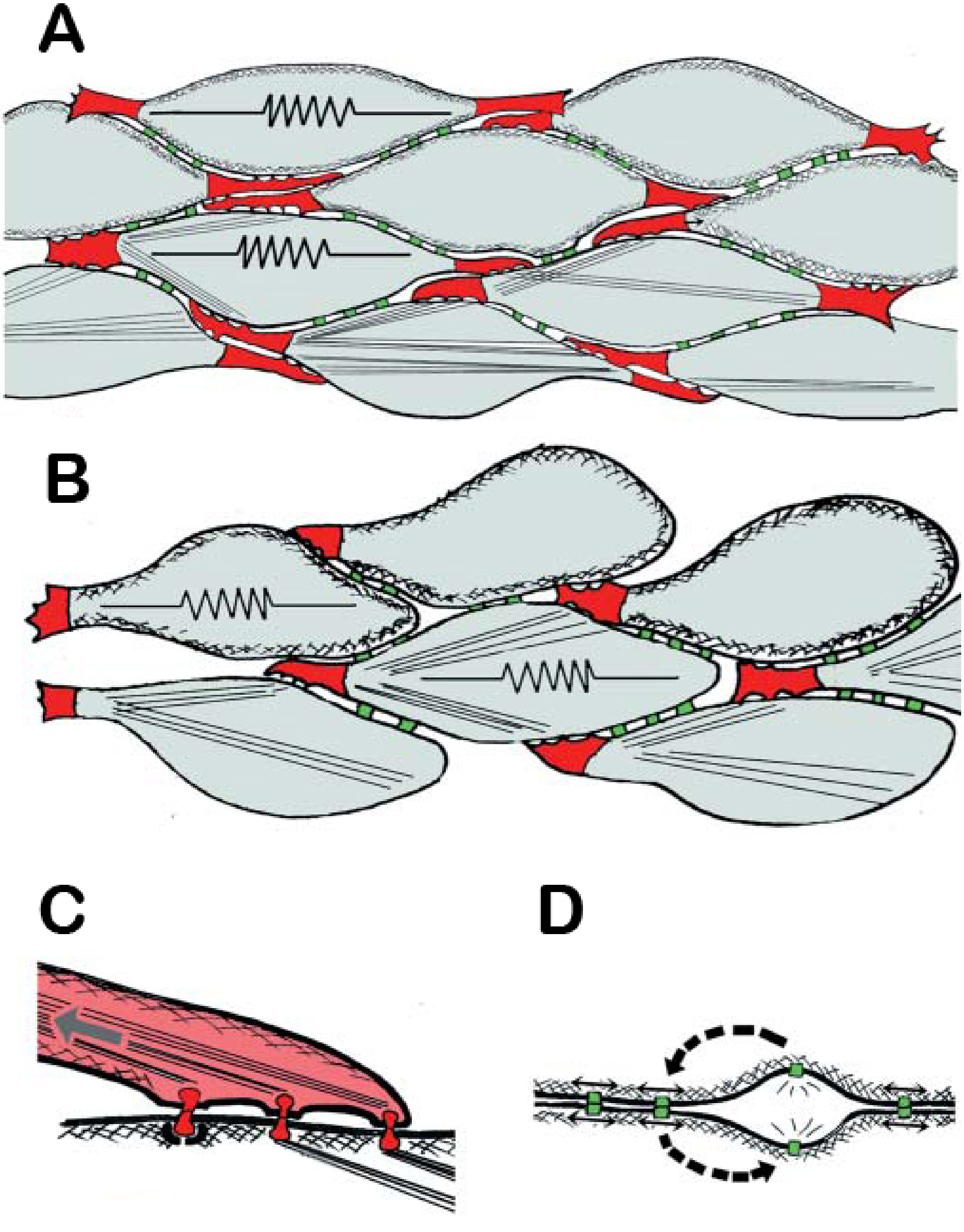
A
B
C
D

1.4 Molecular Control of Convergent Extension: The Planar Cell Polarity (PCP) Pathway

The Planar Cell Polarity (PCP) pathway, also known as non-canonical Wnt signaling, regulates cell intercalation behaviours during neural tube closure. Wnt signaling is initiated when secreted Wnt proteins interact with their cognate Frizzled (*Fz*) receptor (Bhanot et al, 1996; Yang-Synder et al, 1996). *Fz* recruits the cytoplasmic scaffolding protein Dishevelled (*Dsh*) to a juxtamembrane compartment for activation (Djiane et al, 2000). *Dsh* acts as a branch point in Wnt signaling, with pathways being well characterized in the canonical and non-canonical/PCP pathways (Fig. 1.7). Pathway specificity is determined through DIX, PDZ, and DEP domains of *Dsh* (Fig. 1.7). The DIX and PDZ domains function in the canonical, or Wnt/β-catenin signaling, pathway resulting in the stabilization of cytoplasmic β-catenin that translocate into the nucleus where it initiates gene transcription (Itoh et al, 2005).

The PDZ and DEP domains function in the non-canonical or PCP pathway to activate the small GTPases Rho and Rac that modulate the actin cytoskeleton and are required for cadherin mediated cell-cell adhesion (Fig. 1.7) (Wallingford and Habas, 2005; Fukata and Kaibuchi, 2001; Dzamba et al, 2009). The PCP signaling pathway was first discovered in *Drosophila melanogaster*, where it acts to orient wing hairs (Wong and Adler, 1993; Turner and Adler, 1995).The PCP is now recognized to consist of a core cassette of Frizzled (*Fz*), Strabismus (*Stbm*), Diego (*Dgo*), and Prickle (*Prk*), and Dishevelled (*Dsh*) (Wallingford et al, 2002; Wallingford and Habas, 2005). In *Drosophila* wing cells, PCP establishes distal-proximal cell polarity through the asymmetric distribution of core PCP molecules. In vertebrates, these same molecules work downstream of a Wnt signal to establish cell polarity.

In *Xenopus* neural tissue, PCP signaling is regulated through *XWnt11* and *XFx7* and acts to polarize lamellipodia required for CE through Rac and Rho activation (Habas et al, 2001, 2003). In the chordamesoderm, *Xenopus Brachyury* (*Xbra*) inhibits cell migration by promoting CE through activation of downstream target *XWnt11* (Kwan and Kirschner, 2003). *XWnt11* interacts with *XFz7*, predominantly localized to the neuroectoderm and dorsal mesoderm, to activate *XDsh* and regulate the actin cytoskeleton and consequently cadherin mediated adhesion between embryonic blastomeres through *Rac* and *Rho* (Habas et al, 2003). Disruption of the PCP pathway by mutations of *XDsh* randomizes mesodermal cell lamellipodia protrusions and inhibits CE (Wallingford and Harland, 2001; Wallingford, 2006). Mutation or deletion of the PDZ and DEP domains of *Dsh* can also disrupt CE, while over expression of the DEP domain can rescue downstream of Wnt and *Fz* (Wong et al, 2000). In the *Xenopus* neural tube, expression of an *XDsh* mutant that deletes the PDZ and DEP domains cause neural folds to elevate abnormally farther apart and are unable to effectively migrate toward the midline (Wallingford and Harland, 2002). The data indicates that PCP signaling can control the protrusive activity and adhesive properties of cells in tissues undergoing CE. How the PCP affects the biomechanical properties of the neural plate during neurulation has not been clearly studied and is one of the goals of my thesis work.

Figure 1.7 Canonical and Non-canonical Wnt pathways. (A) Canonical Wnt signaling mediates gene transcription by stabilization and accumulation of β-catenin in the nucleus. (B) Non-canonical Wnt or PCP signaling activates GTPases Rho and Rac to mediate actin cytoskeleton reorganization. (modified from Wallingford and Habas, 2005)

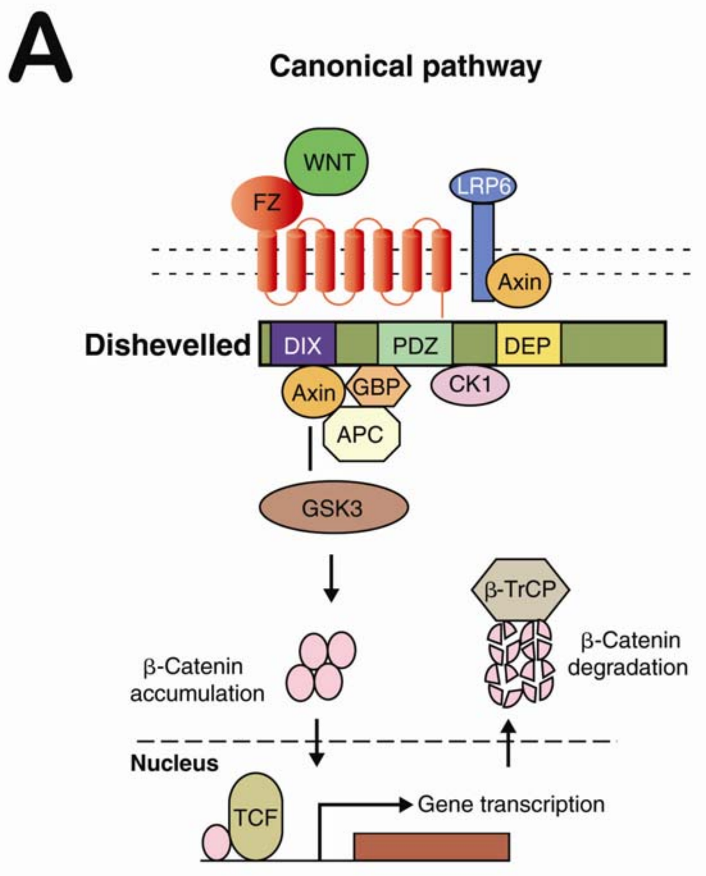
A

Canonical pathway

WNT
FZ
LRP6
Axin
Dishevelled
DIX
PDZ
DEP
Axin
GBP
CK1
APC
GSK3
β-TrCP
β-Catenin accumulation
β-Catenin degradation
Nucleus
TCF
Gene transcription

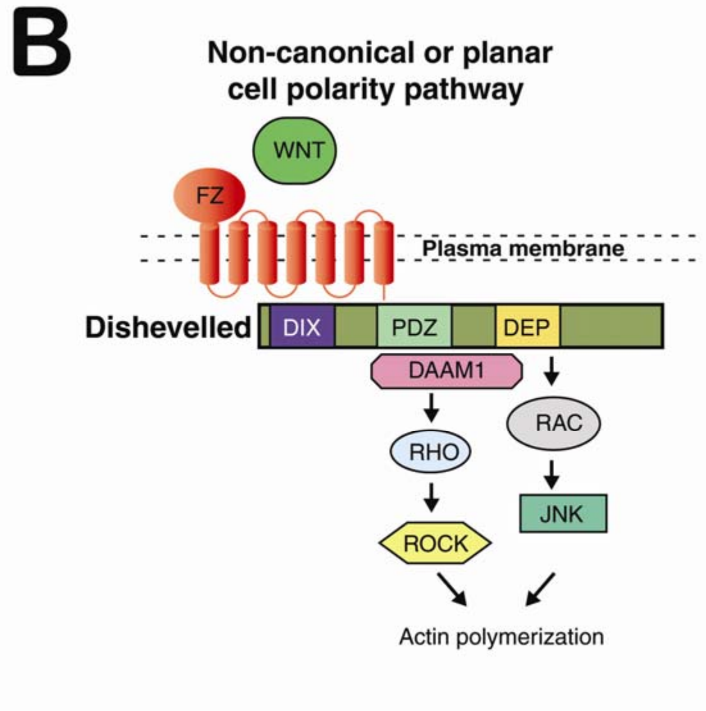
B

Non-canonical or planar cell polarity pathway

WNT
FZ
Plasma membrane
Dishevelled
DIX
PDZ
DEP
DAAM1
RAC
RHO
JNK
ROCK
Actin polymerization

1.5 Experimental Rationale

While both mesoderm and the neural plate undergo CE, current biomechanical studies describe the notochord as the primary source of force production during neurulation (Zhou et al, 2009). However, previous evidence suggest that *Xenopus* explants without notochords can converge, extend, and elongate nearly as well as explants with notochords (Malacinski and Youn, 1981; Malacinski and Youn, 1981). This suggests that other tissues contribute to axial elongation in *Xenopus*. As the neural plate also undergoes CE, the possibility exists that this tissue contributes to axial elongation. This would suggest that the cell rearrangements in the neural plate can generate force.

My hypothesis is that the forces that help shape the neural plate arise from morphogenetic movements in the neural tissue. I will test this hypothesis by measuring the biomechanical properties of *Xenopus* neural tissue at various stages of development. I will also measure these properties under experimental conditions that disrupt neurulation. *Xenopus laevis* embryos are well suited to this form of experimental approach as tissues can be easily excised and cultured *ex vivo*. Also, molecular manipulation that induces failed neural tube closure *in vivo* is easily established in *Xenopus laevis* embryos.

The objectives of my research were to establish an experimental system to evaluate the stiffness of *Xenopus* neural tissue and then determine what the control mechanisms are that regulate tissue stiffness in the neural ectoderm. In this study, neurulation was disrupted by interfering with the PCP pathway and changes in stiffness of the neural plate were measured. Dominant-negative *Wnt11* constructs were expressed to interfere with PCP signaling outside the cell. PCP signaling was also blocked at the cell membrane by expressing a dominant-negative *Fz7*, the receptor of *Wnt11*, and inhibited in cytoplasm using a dominant-negative *Dsh* construct.

Chapter 2

Methods and Materials

2.1 *Xenopus laevis* Embryos

Sexually mature *Xenopus laevis* were purchased from Nasco (Fort Atkinson, Wisconsin) and housed in the Department of Biology Aquatic Facility at the University of Waterloo. Female frogs were injected with 400 units of human chorionic gonadotropin (HCG) (Sigma, Oakville, Ontario) to induce spawning. Eggs were obtained from spawning females and fertilized *in vitro* by standard methods (Sive, 1996). Fertilized embryos were dejellied in 2% cysteine (EMD, Mississauga, Ontario) in water and cultured in 0.1X Modified Barth's Saline (MBS) (1X MBS; 88mM sodium chloride (NaCl), 1mM potassium chloride (KCl), 0.7mM magnesium sulphate ($MgSO_4$), 1mM HEPES, 5mM sodium bicarbonate ($NaHCO_3$), 0.1mM calcium chloride ($CaCl_2$), at pH 7.6.

2.2 Microinjection and Dominant-negative Injected Embryos

An *XDsh*-delta PDZ construct (XE123), was obtained as a gift from R Moon (University of Washington) in the CS2+ vector (Miller et al, 1999b). The construct was linearized with the NotI restriction enzyme. A dn*XFz7*, or *XFz7*ΔT, construct consisting of a cytoplasmic tail deletion was obtained as a gift from S Sumanas (University of Minnesota) in the pT3Ts vector. The *XFz7*ΔT-T3TS plasmid was linearized using the BamHI restriction enzyme. The dn*XWnt11* construct was as a gift from J Smith (Cambridge University) in the pSP64TXB vector. The plasmid was linearized using the BamHI restriction enzyme. RNA was made by in vitro transcription using mMessage mMachine kit (Ambion) according to manufacturer's instructions (SP6 promoter for *XE123* and dn*XWnt11*, T3 promoter for dn*XFz7*).

Microinjection needles were formed using a Narishige PC-10 pipette puller (East Meadow, New York). Embryos were placed in 0.5X MBS with 4% Ficoll 400 (Sive, 1996) and microinjected with a Narishige EM300 pressure injector (East Meadow, New York) with 2ng of either dn*XDsh*, dn*XFz7*, or dn*XWnt11* RNA at the one cell stage (Sive, 1996). Embryos were cultured in 0.1X MBS following microinjection.

2.3 Microsurgery

Explants were taken from stage 11 (early gastrula), 12 (mid gastrula), or stage 13 (late gastrula), *Xenopus laevis* embryos. Embryos were staged according to Nieuwkoop and Faber (1967). These stages were chosen to compare stiffness in the neural plate prior to the onset of CE at stage 11, at the onset of CE, stage 12, and when CE is actively occurring at stage 13. Embryos were dissected in Danilchik's for Amy (DFA) solution (53 mM sodium chloride (NaCl), 32 mM sodium gluconate ($NaC_6H_{11}O_7$), 5 mM sodium carbonate (Na_2C0_3), 4.5 mM potassium chloride (KCl), 6mM HEPES ($C_8H_{18}N_2O_4S$), 1 mM calcium chloride ($CaCl_2$), 1 mM magnesium sulphate ($MgSO_4$), at pH 8.1), plus bovine serum albumin (BSA, 1 mg/ml) to minimize wound healing (Sater et al, 1993). Vitelline membranes were removed manually with forceps and eye lash hair knives and hairloops (Keller et al, 1999) were used to remove dorsal ectoderm. After the epithelium was removed and discarded (Fig. 2.1 A), the neural ectoderm and mesodermal cell layers were explanted away from the underlying endodermal epithelium. This is known as a deep neural over mesoderm explant or neural tissue explant (Fig. 2.1 B; Keller et al, 1999). A similar explant that excludes the underlying mesoderm, known as deep neural explants, was also made but was more difficult to excise. Since there was no significant difference in measured stiffness between deep neural and neural explants (deep neural over mesoderm explants), the more easily explanted neural explants were used for experiments (Keller et al, 1999).

Figure 2.1: Isolation of deep neural over mesoderm explants. The dorsal epithelial layer is removed first (A) followed by removal of the deep neural ectoderm attached to the mesoderm from the underlying endoderm (B).

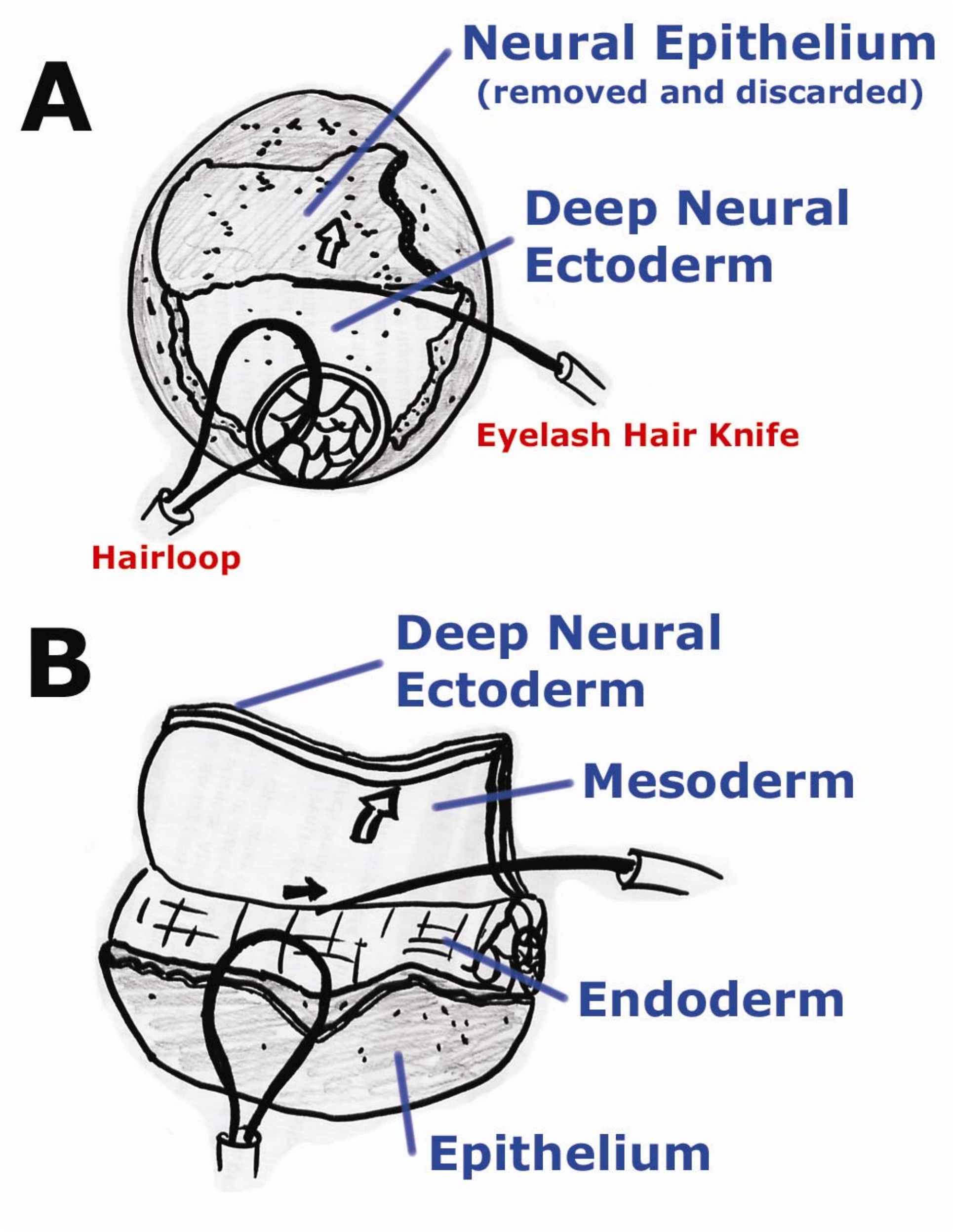
A
Neural Epithelium
(removed and discarded)
Deep Neural Ectoderm
Eyelash Hair Knife
Hairloop
B
Deep Neural Ectoderm
Mesoderm
Endoderm
Epithelium

2.4 Apparatus Design and Tensile Measurement

The apparatus used for measuring stiffness was a redesign of an instrument built for measuring tensile forces in *Ambystoma mexicanum* embryos (Wiebe and Brodland, 2005). After dissection, explants were transferred to a plexiglass chamber filled with DFA. Explants were situated on a removable platform located at one end of the plexiglass chamber. Two fine parallel stainless steel wires, 63 µm in diameter and 50 mm in length, fixed at the opposite end of the chamber ran horizontally toward the explant platform (Fig. 2.2 B). The free ends of the wires were glued with FLASH brand Thick viscosity cyanoacrylate glue (NorPak Inc, Lolley, Massachusetts) onto the lateral ends of explants. The chamber had a wire lifting mechanism where an outside dial controls two prongs to lift and lower the free ends of the wires in and out of solution (Fig. 2.2 B). Once the wires adhered to the explant, the explant platform was removed allowing the attached explants to float free. A vertical fine tungsten needle attached to a staged computer controlled actuator (Zaber Technologies Inc., Vancouver, British Columbia) (Fig. 2.2 A) was lowered between the two stainless steel wires (Fig. 2.2 C). During testing, the actuator pushed the tungsten needle against the "active wire" near the glued explant and stretched the explant placing it under tension (Fig. 2.2 D). The actuator was controlled by the "TissueGUI" program (Wiebe and Brodland, 2005). The original TissueGUI program moved the active wire slowly at a strain rate of 30% per hour, stretching the tissue in approximately 0.1 µm increments while recording images every 15 seconds. An image-based feedback system ensured the tissue was being stretched at a constant strain rate of 30% per hour by tracking the wire movements to compare the measured distance between the wires of the most recent image taken with the preceding image to control the actuators movements in the next 15 seconds. The TissueGUI2 program was reprogrammed to run in two phases. Phase A runs similarly to the original program except it quickly pushes the active wire displacing it 200 µm in 8 seconds while taking multiple images. Tracking is completed later and reveals that tissues are stretched with an average strain rate of about 200% strain per hour. Phase B continues from the end of Phase A and uses a similar image-based feedback system to sustain a constant strain in the stretched tissue for 5 minutes.

Figure 2.2: Experimental equipment and setup. (A) The plexiglass chamber is placed under the microscope and the staged computer controlled actuator is placed to the right. (B)The plexiglass chamber allows quick lowering of the fine wires to be glued onto the explant. (C) A fine tip tungsten needle attached to the actuator is placed between the two wires. (D) An image captured through the microscope of the glued explant by the TissueGUI program. The active wire is pushed by the tungsten needle while the fixed wire is pulled along by the stretching tissue.

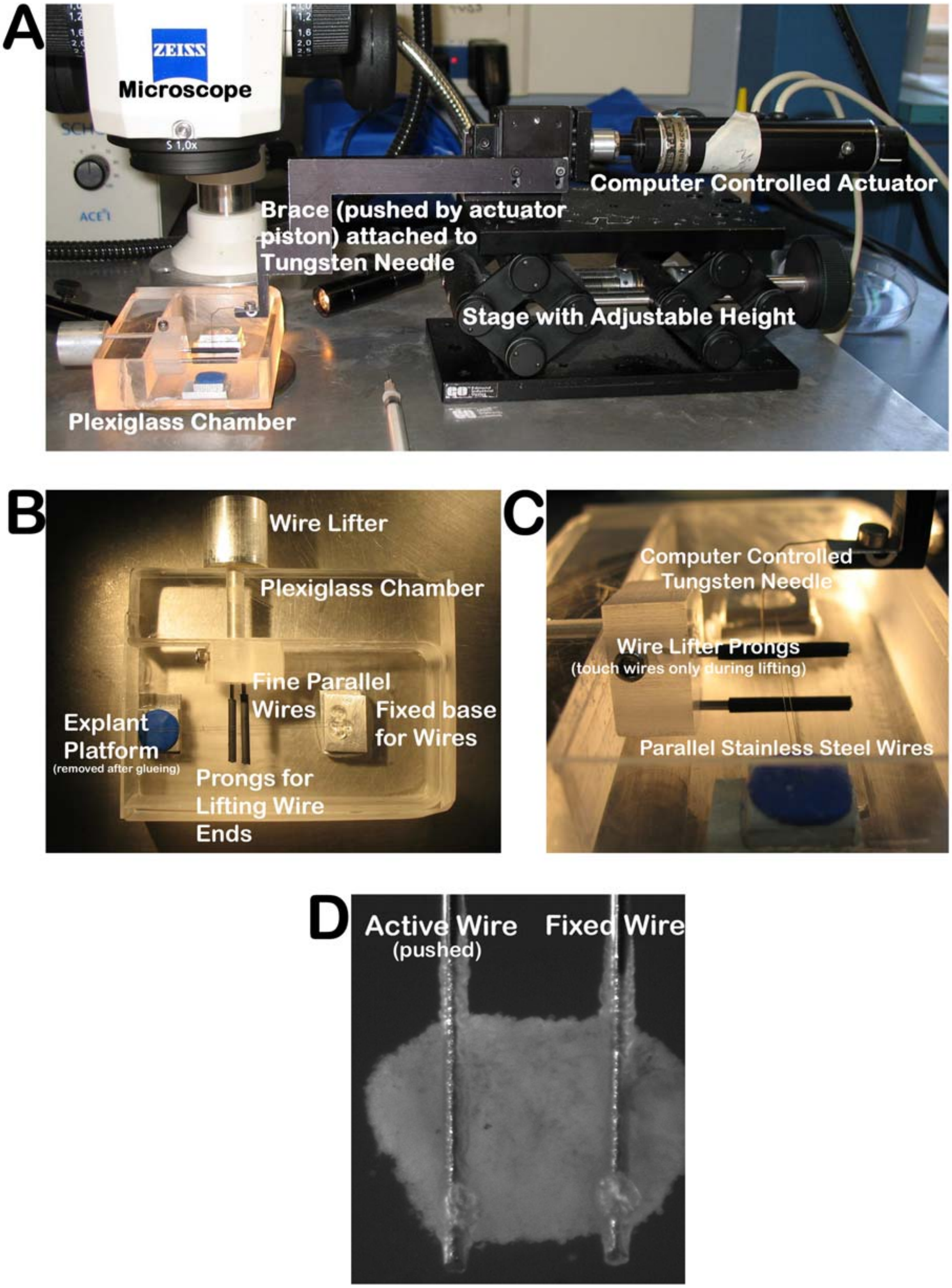
A
Microscope
Computer Controlled Actuator
Brace (pushed by actuator piston) attached to Tungsten Needle
Stage with Adjustable Height
Plexiglass Chamber
B
Wire Lifter
Plexiglass Chamber
Fine Parallel Wires
Fixed base for Wires
Explant Platform
(removed after glueing)
Prongs for Lifting Wire Ends
C
Computer Controlled Tungsten Needle
Wire Lifter Prongs
(touch wires only during lifting)
Parallel Stainless Steel Wires
D
Active Wire
(pushed)
Fixed Wire

2.5 Data Analysis

The tensile force of explants was calculated from the unpushed “fixed wire” by treating it as a cantilever beam with a load at its free end. The ‘beam equation’ was rearranged to calculate tensile force:

$$\Delta d = \frac{F \cdot L^3}{3 \cdot E_{steel} \cdot I} \quad \rightarrow \quad F = \frac{3 \cdot \Delta d \cdot E_{steel} \cdot I}{L^3}$$

Where F is the tensile force, L is the length of the fixed wire, Δd is the displacement of the fixed wire, E is the cantilever material’s elastic modulus that is constant, and I is the second moment of inertia which is a property of the beam shape and is a constant.

According to ‘beam theory’, the “active wire” is significantly stiffer than the other fixed wire due to needle placement and does not bend due to its shorter length. Tensile stress, the magnitude of tensile forces in an area, was calculated by dividing the total tensile force F by the initial cross-sectional area ‘A_0’ of the tissue. Tensile strain, the amount of stretch in the tissue, was calculated by dividing the change in length ΔL by the original length L_0. Young’s modulus ‘E’, or the modulus of elasticity, representing tissue stiffness, was determined by the slope of a stress verses strain curve expressed by the equation:

$$E \equiv \frac{tensile\ stress}{tensile\ strain} = \frac{F/A_0}{\Delta L/L_0}$$

Our method did not measure explant thickness and limited our analysis to calculating tensile stress using surface area rather than cross-sectional area (A_0). This exclusion accounts for my stiffness measurements represented in N/m rather than in N/m^2 or Pa which are used normally. However, when an average explant thickness of 40-60 microns (personal observations and Zhou et al, 2009) was included in my calculations, results were very similar to those reported in previous literature.

Data was normalized to stage 11 ML or AP stiffness of control explants, and standard variation was used to calculate error. Student T-tests were used for statistical analysis and the differences between sample averages were considered statistically significant when $P \leq 0.05$.

Chapter 3

Results

3.1 Device Modifications

The greatest challenge was to design a device that could measure the biophysical properties of the small and delicate *Xenopus* embryo. The previous device designed to measure stiffness in larger *Ambystoma mexicanum* embryos (Wiebe and Brodland, 2005) was too bulky to fit under a stereoscope and provided little space to work in. We designed a plexiglass chamber that was small enough to fit under a stereoscope and still left workable space for embryo manipulation. A simplified wire lifting mechanism was incorporated into the chamber that made the gluing process faster and ensured the wires were glued on the explants accurately. The final goal was to optimize the attachment of the cantilever wires to the embryonic tissue in a consistent way that did not cause tissue injury. Two major factors influenced wire attachment: the type of glue and the type of wire.

3.1.1 Selection of Adhesives

The two most important criteria in selecting an adhesive for attaching the cantilever wires onto explanted tissues were bond strength under aqueous conditions and a fast cure time. Several types of adhesives were tested (Table 3.1). In all situations the wires were coated with adhesive and then placed in contact with excised tissue that was immersed in DFA.

Initially, I tried using Loctite brand adhesives that can be cured through exposure to UV light. Loctite UV adhesive 3014 and a related but more viscous adhesive 3016 were used (Table 3.1). When submerged in aqueous solution both the UV adhesives were diluted and provided weak bonding to the explants after curing (Table 3.1). Next, a fusion protein was used as a biological adhesive. In *Xenopus*, C-cadherin is the dominant cell-cell adhesion molecule expressed during early development. C-cadherin can be expressed in vitro as a GST-fusion protein and acts as a functional adhesive molecule (Brieher and Gumbiner, 1994). However, adhesion required a 20 minute contact time and ultimately attachment was too weak to hold the explant under tension (Table 3.1). Mr.Sticky's underwater epoxy is used to attach invertebrates to rock substrates in aquariums and is designed to be able to be applied and cured in aqueous environments. Use of this adhesive proved impractical as it required a 24 hour cure time (Table 3.1).

Cyanoacrylate glue was used in previous experiments (Wiebe and Brodland, 2005) and has the advantages of a strong bond and fast cure times. In our system the use of cyanoacrylate adhesive was complicated by the requirement to attach wires to tissues in an aqueous environment. Since cyanoacrylate glues cure rapidly in the presence of water, I experimented with different viscosities of this adhesive in an attempt to delay cure times. Low viscosity cyanoacrylate glue, such as ZAP PT-08 and ZAP PT-02, exhibited beading on the wires that lead to only partial bonding along the glue length (Table 3.1). FLASH brand cyanoacrylate glue is more viscous and was the most consistent in providing strong attachment (Table 3.1). As such FLASH thick viscosity cyanoacrylate glue was the adhesive used for all tests.

Table 3.1: Relative viscosity, cure time, and strength of attachment of wires to tissue explants of several types of adhesives. '-' represents low viscosity, slow cure times (longer than one hour), and little to no attachment of wires onto explants. '++++' represents high viscosity, fast cure times (less than 3 seconds), strong attachment where explants remained attached to the wires along the entire glue length after stretching.

Adhesive	Viscosity	Cure Time	Attachment
LOCTITE UV Adhesive – 3014	+	++++	+
LOCTITE UV Adhesive – 3016	+	++++	+
Mr. Sticky's Underwater epoxy	+++++	-	-
C-Cadherin	N/A	+	+
ZAP PT-08 (Super Thin Viscosity) Cyanoacrylate	+	++++	++
ZAP PT-02 (Medium Viscosity) Cyanoacrylate	++	++++	++
FLASH Thin Viscosity Cyanoacrylate	++	++++	++
FLASH Medium Viscosity Cyanoacrylate	+++	++++	+++
FLASH Thick Viscosity Cyanoacrylate	++++	++++	++++

3.1.2 Types of Wires

The design of the device relies upon the cantilever properties of two fine wires from which the tissue explants were suspended. As the modulus of the materials that these cantilevers are made from directly influenced my measurements, it was critical that wire selection be optimized. 75 µm diameter tungsten wires were tested first. The hydrophobic oxidized surface of the tungsten wires caused adhesive beading and the glue cured in a crystalline fashion resulting in irregular and weak bonding along the explants (Fig. 3.1A). In an attempt to improve the interaction between the adhesive and the wires the tungsten wires were coated with gold/palladium. However, this had no discernable effect on the performance of the glue-wire combination.

I also tried stretching glass and plastic into fine fibres. There was no beading of adhesive, but it was difficult to consistently make wires of the same thickness and the wires were buoyant and unable to break the surface tension of the solution in the chamber. The original experimental design (Wiebe and Brodland, 2005) used 125 µm diameter stainless steel wires. However, they were too large to fix onto the small *Xenopus* embryo explants, which were about 750 µm in width. The resulting small gap between the large wires often caused cyanoacrylate glue to fix the wire ends together. Therefore, the finest stainless steel wires available, which were 63 µm in diameter, were purchased. Cyanoacrylate glue applied to these stainless steel wires consistently provided a strong attachment along the glue length (Fig 3.1B).

Figure 3.1: **Patterns of cured cyanoacrylate glue on tungsten wires versus stainless steel wires.** (A) Cyanoacrylate glue cured partially along the glue length and in crystallin fashion (red outline) on tungsten wires resulting in weak attachment. This is more visible on the 'fixed' wire, 'F', than the 'active' wire, 'A'. The explant, 'E', is shown glued to these wires. (B) Stainless steel wires provided smooth and uniform gluing (blue outline) resulting in strong attachment.

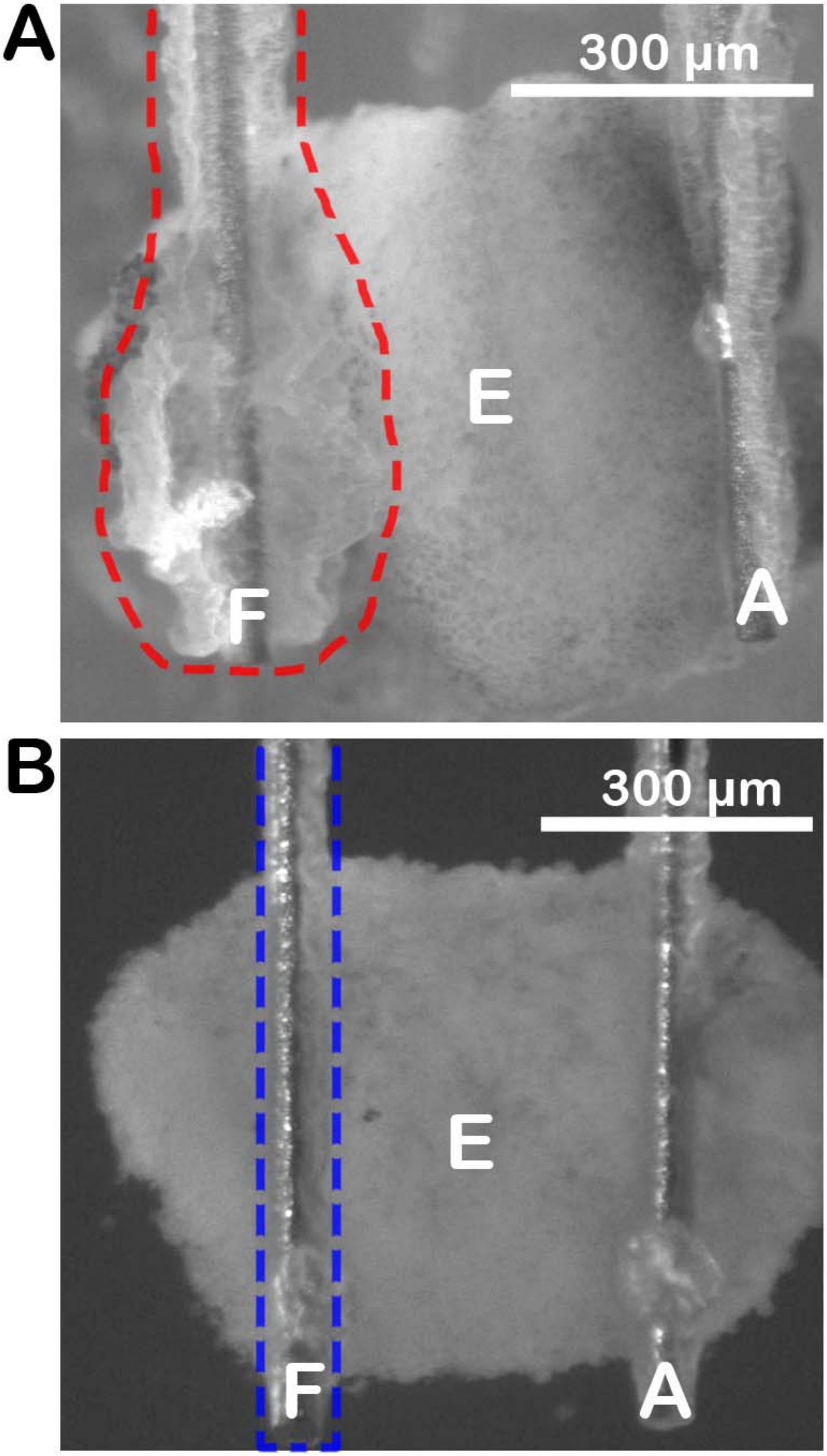
A
300 µm
E
F
A
B
300 µm
E
F
A

3.2 Preliminary Tests

Having developed a device capable of holding and stretching explants from *Xenopus* embryos I then evaluated its performance in preliminary experiments. The original TissueGUI program stretched the tissue at a set strain rate of 30% strain/hour. Figure 3.2A shows a representative example of a tensile stress versus strain graph (Fig. 3.2A). The linear portion of the curve (red box) represents where the tissue was being stretched at a constant strain rate. The slope of this linear segment represents the stiffness in N/m (Fig. 3.2B). Stiffness measurements were calculated from 48 tests comparing stiffness at developmental stages 11, 12, and 13 (Fig. 3.3). Stage 11 deep neural explants had an average stiffness of 0.0119 ±0.0073 N/m (n=7) and stage 11 neural explants had an average stiffness of 0.0133 ±0.0073 N/m (n=8) ($P > 0.05$) (Fig. 3.3). Stage 12 neural explants had an average stiffness of 0.0152 ±0.0077 N/m (n=21), nearly equivalent to average stiffness at stage 13, 0.0151 ±0.0070 N/m (n=12) ($P > 0.05$) (Fig. 3.3). There is no significant difference in the average stiffness measurements between developmental stages ($P > 0.05$).

Figure 3.2: Calculation of stiffness with stress (tensile) versus strain graphs (A) Representative stress versus strain graph. Each dot on the graph represents a data point collected during the test. This particular test was of a neural explant from a stage 11 *Xenopus* embryo and measured ML stifness. The linear portion of the curve is boxed in red. (B) Isolation of the linear portion to calculate tissue stiffness (slope). The black line represents the calculated slope of the curve.

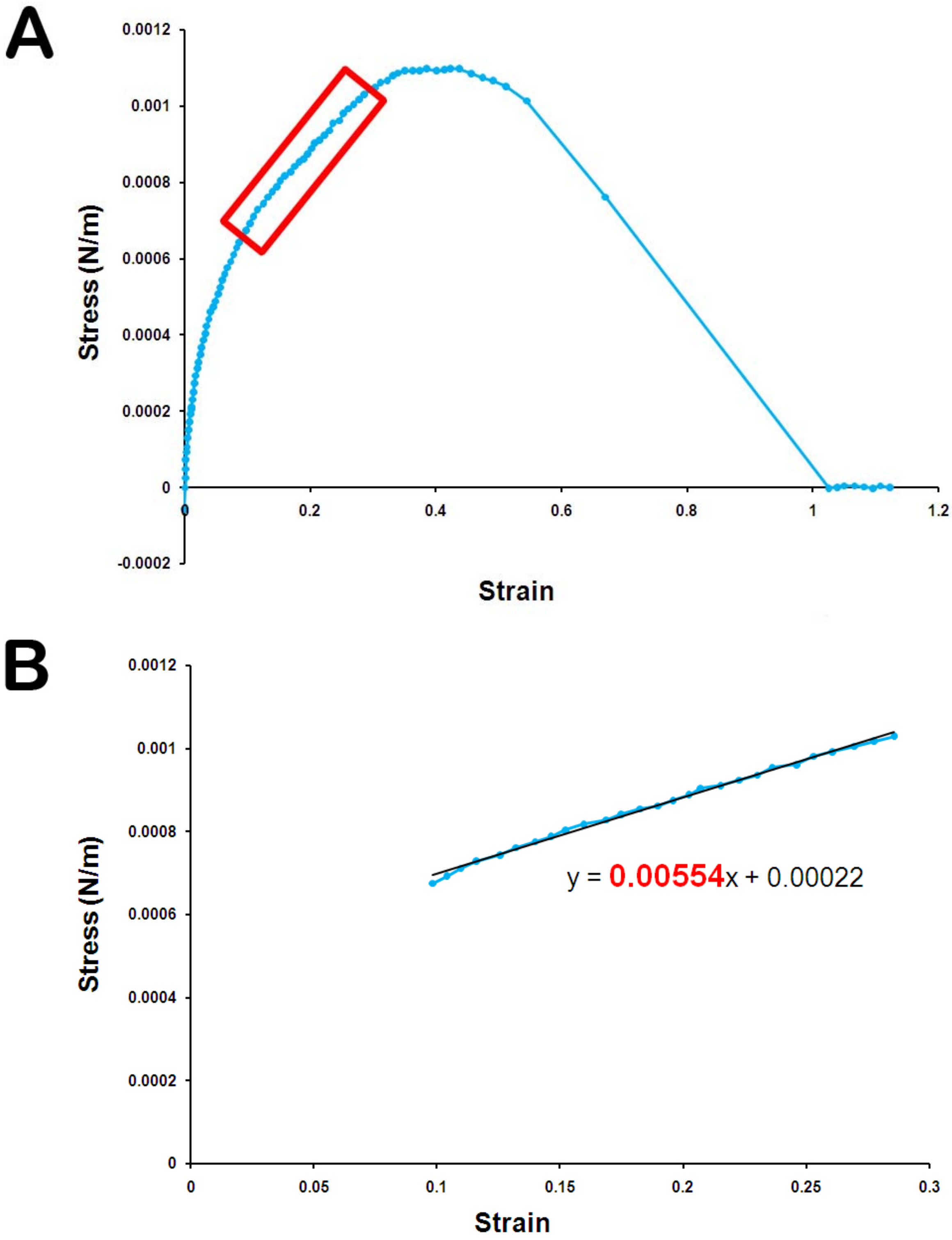
A
0.0012
0.001
0.0008
0.0006
0.0004
0.0002
0
-0.0002
Stress (N/m)
0
0.2
0.4
0.6
0.8
1
1.2
Strain
B
0.0012
0.001
0.0008
0.0006
0.0004
0.0002
0
Stress (N/m)
y = 0.00554x + 0.00022
0
0.05
0.1
0.15
0.2
0.25
0.3
Strain

Figure 3.3: Average stiffness of *Xenopus* deep neural and neural tissue explants at different development stages. Average stiffness with standard deviation of preliminary tests at different stages. Average stiffness of stage 11 deep neural explants, 0.0119 ±0.0073 N/m, were not significantly different from average stiffness of stage 11 neural tissue explants, 0.0133 ±0.0073 N/m, ($P > 0.05$). Average stiffness of neural tissue explants seem to increase from stage 11 to stage 12, 0.0152 ±0.0077 N/m and 13, 0.0151 ±0.0070 N/m. However, these differences are not significant ($P > 0.05$).

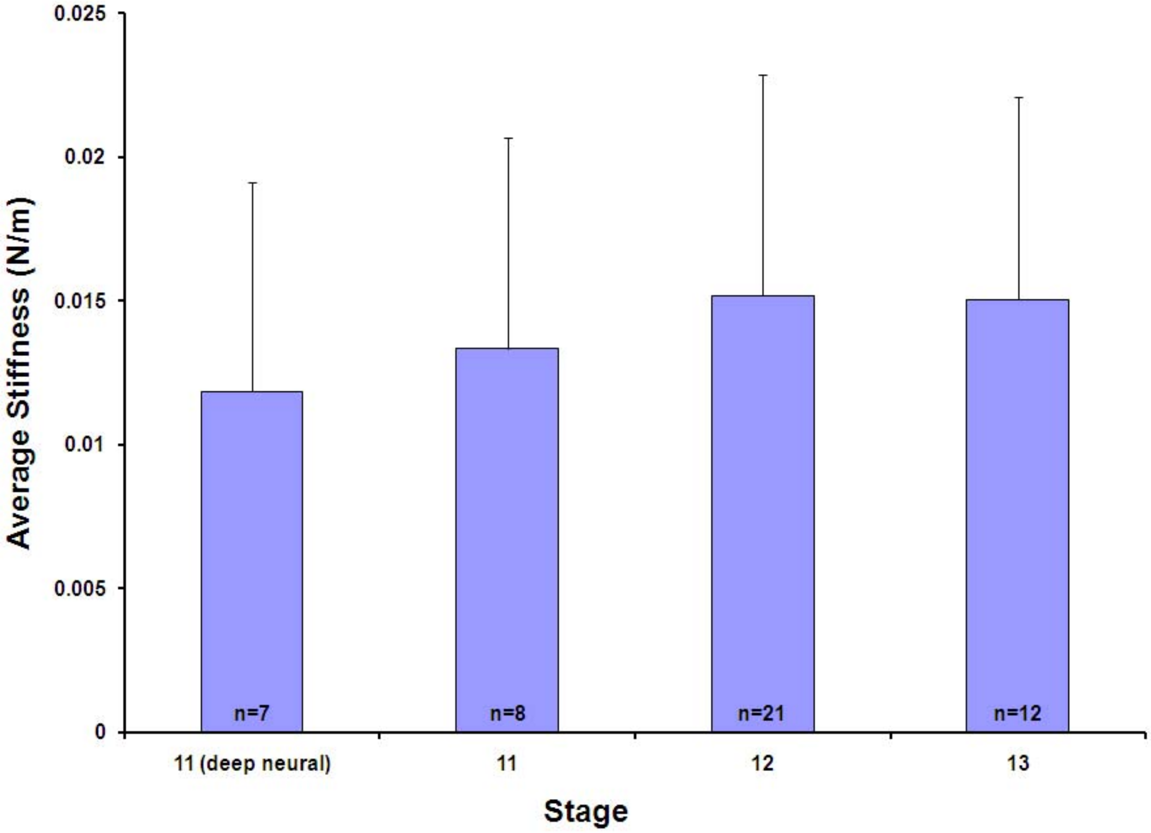
0.025
0.02
0.015
0.01
0.005
0
Average Stiffness (N/m)
n=7
n=8
n=21
n=12
11 (deep neural)
11
12
13
Stage

3.3 Sources of Error and Variability

Based on previous literature it was expected that there would be considerable differences between these stages with stiffness measurements ranging from 3 to 10 N/m^2 (Moore et al, 1995). My data showed no significant differences in stiffness between stages (Fig. 3.3). This suggested that our experimental design may not be sensitive enough to discriminate between small changes in tissue stiffness.

3.3.1 The Effects of Wound Healing

Upon further examination the effects of wound healing, the tendency of explants to curl up as to close ‘a wound’, was discovered to be responsible for skewing my results. This effect was visible as an initial negative sloping curve in the stress versus strain graphs (representative data shown in Fig. 3.4). The negative slope represents a decrease in the gap between the two wires. This was exemplified when tests programmed to run at 0% strain/hour exhibited negatively sloping linear curves clearly demonstrating that wound healing drew the cantilever wires together (Fig. 3.5). Tissue stiffness calculated from the slope was 0.0036 N/m with an average healing rate of 35% strain/hr (representative data shown in Figure 3.5). Reprogramming the TissueGUI program to stretch tissues at strain rates of 200% strain/hour or above successfully removed the negative slope seen at the beginning of graphs limiting the effects of wound healing on my measurements (Fig. 3.6).

Figure 3.4: **Wound healing.** (A) A stress versus strain graph with an initial negative slope (red box) that represents a decrease in the gap between the wires. (B) A close-up of the negative slope boxed in red.

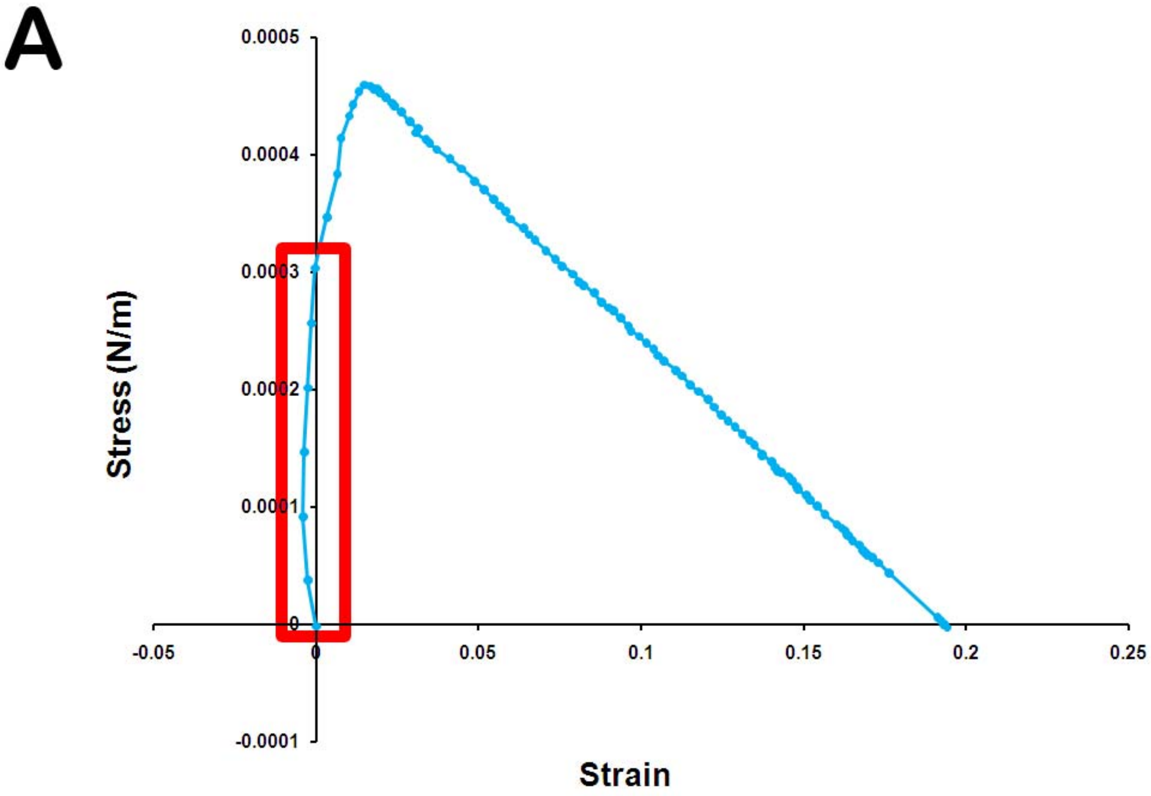
A
Stress (N/m)
0.0005
0.0004
0.0003
0.0002
0.0001
0
-0.0001
-0.05
0
0.05
0.1
0.15
0.2
0.25
Strain

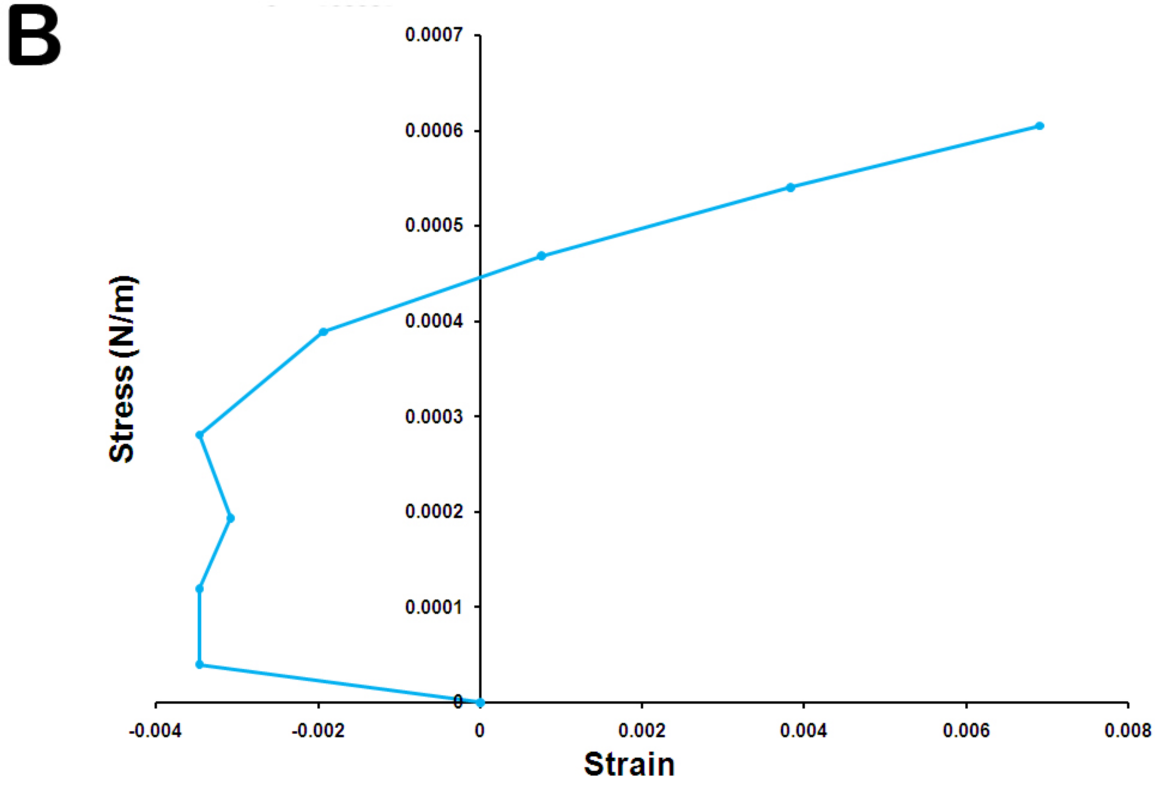
B
Stress (N/m)
0.0007
0.0006
0.0005
0.0004
0.0003
0.0002
0.0001
0
-0.004
-0.002
0
0.002
0.004
0.006
0.008
Strain

Figure 3.5: **Tissue stiffness during wound healing.** Stress versus strain and strain versus time graphs of a test run at 0% strain rate. (A) The negative slope of the curve in this stress versus strain graph represents that the wires were being drawn closer together. A slope of -0.0051 translates into a stiffness of 0.0051 N/m. The black line represents the calculated slope. (B) Strain is plotted against time where the slope is used to calculate strain rate of wound healing. This explants had a wound healing rate 0.72 strain/hr. The black line represents the calculated slope.

A

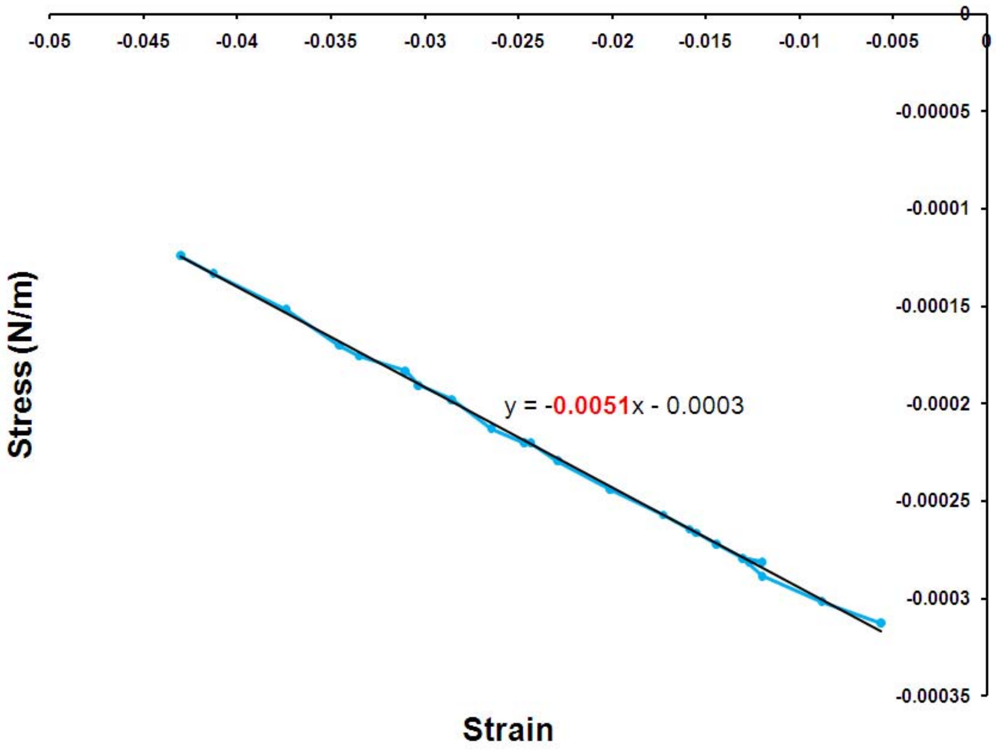
Stress (N/m)
Strain
y = -0.0051x - 0.0003
-0.05
-0.045
-0.04
-0.035
-0.03
-0.025
-0.02
-0.015
-0.01
-0.005
0
0
-0.00005
-0.0001
-0.00015
-0.0002
-0.00025
-0.0003
-0.00035

B

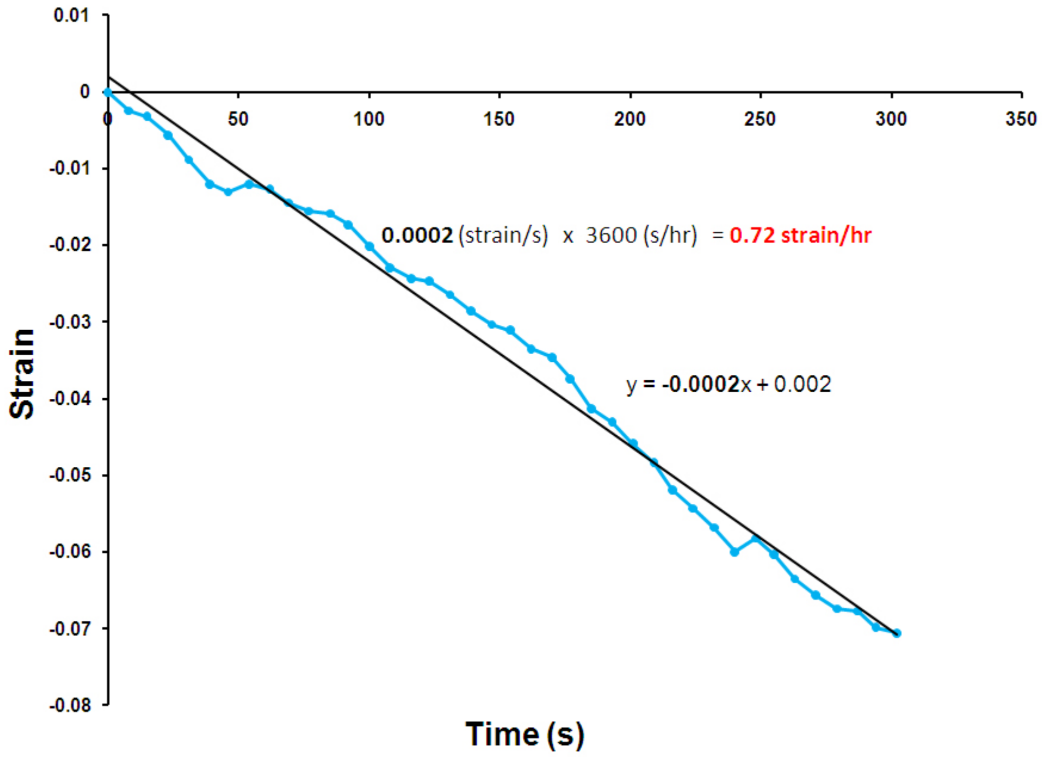
Strain
Time (s)
0.0002 (strain/s) x 3600 (s/hr) = 0.72 strain/hr
y = -0.0002x + 0.002
0.01
0
-0.01
-0.02
-0.03
-0.04
-0.05
-0.06
-0.07
-0.08
0
50
100
150
200
250
300
350

Figure 3.6: High programmed strain rates remove the effects of wound healing. Stress versus strain graph of a test run at 200% strain rate to remove the effects of wound healing. The negative slope of the curve produced from the effects of wound healing observed in figure 3.4 is removed in stress versus strain graphs from tests programmed to run at 200% strain. The increasing strain line does not cross the ordinate axis.

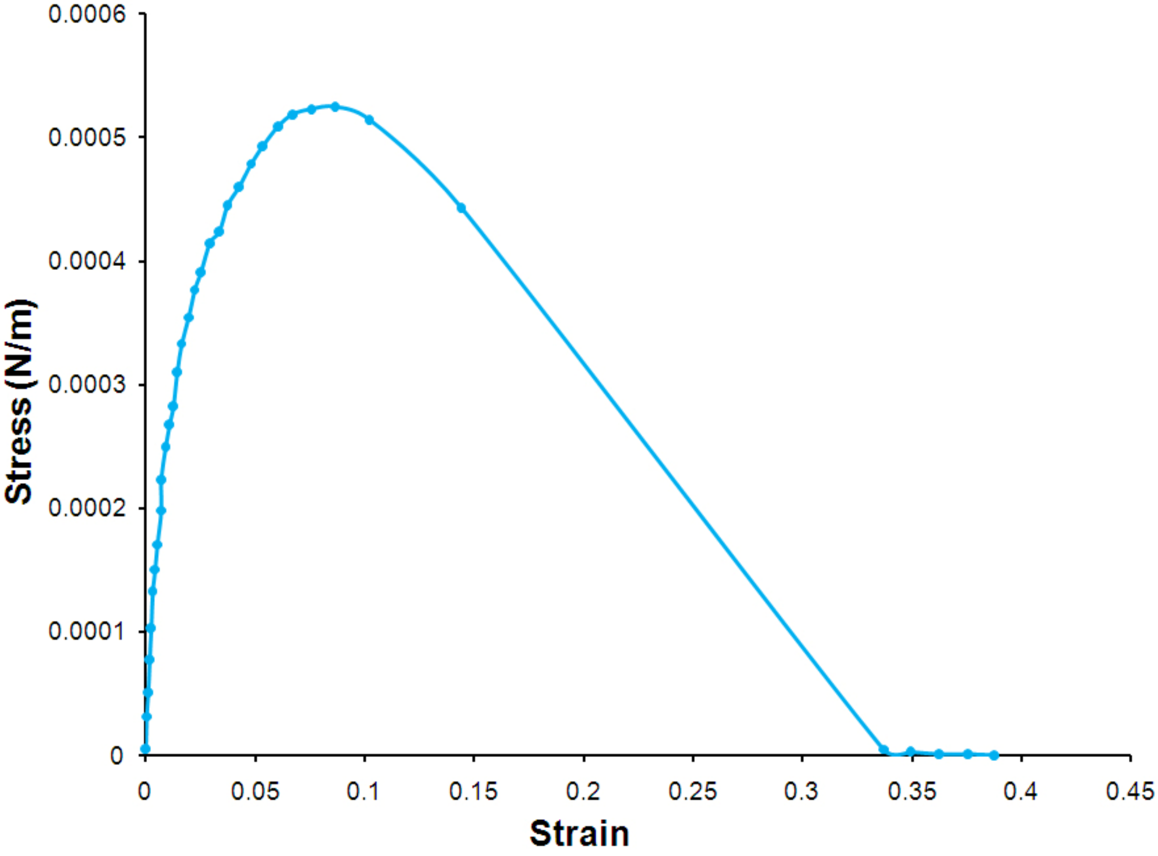
0.0006
0.0005
0.0004
0.0003
0.0002
0.0001
0
Stress (N/m)
0
0.05
0.1
0.15
0.2
0.25
0.3
0.35
0.4
0.45
Strain

3.3.2 Slope Determination

Another source of variability was selecting the linear portion of the rising slope of the stress versus strain graphs used to calculate stiffness (Fig. 3.7). Depending on what range of strain the linear segments were taken across, the calculated stiffness changed dramatically. Stiffness calculated from 0-2% strain was erratic (Fig. 3.7A) with an average stiffness of 0.0105 ±0.0037 N/m (Table 3.2) compared to stiffness calculated above 2% strain (Fig. 3.7B), averaged 0.00433 ±0.0015 N/m (Table 3.2). Due to the consistency of stiffness calculations taken from 2% strain to the highest strain sustained in tissue, this portion of the curve was used in all subsequent measurements. In Figure 3.7, stiffness was calculated from explants that sustained strains of up to 8% before tearing.

Table 3.2: Average stiffness from 0 to 2% strain and 2 to 8% strain of tests run at a strain rate of 200%/hr. Stiffness measurements calculated from slopes taken from 0% to 2% strain where higher and more variable, three times the standard error, than stiffness measurements taken from slopes from 2% to 8% strain.

Test Number	Stiffness (N/m) from 0% to 2% Strain	Stiffness (N/m) from 2% to 8% Strain	Embryo Stage
144	0.01206	0.00644	12.5
145	0.01059	0.00594	12.5
157	0.00678	0.00291	12.5
158	0.00916	0.00419	12.5
162	0.00773	0.00325	12.5
163	0.0169	0.00348	12.5
Average	0.0105 ± 0.0037	0.00433 ± 0.0015	

3.3.3 Clutch-to-Clutch Variability

Slopes after 2% strain were more consistent; however, the actual stress values of the slopes covered a wide range. In Figure 3.7B, stress values differed by four-fold. This high variation was most likely due to natural clutch-to-clutch variation of the biomechanical properties seen in *Xenopus* embryos (von Dassow and Davidson, 2007). This is most clearly exemplified when the linear slopes of stress versus strain data from a variety of embryo clutches are plotted on one stress versus strain graph (Fig. 3.8). Data from embryos of the same clutch cluster together. In this graph the clustering of two clutches is evident, Test 164 and 165 were explants from embryos of one clutch and Test 171 and 172 were explants from embryos of another clutch. The tensile stresses of the tissues varied by as much as four-fold, approximately 0.0002 to 0.0004 N/m of tensile stress over 2% to 8% strain in Test 172 compared to approximately 0.0008 to 0.001 N/m of tensile stress over 2% to 8% strain in Test 164 (Fig. 3.8). Therefore, to limit clutch-to-clutch variation the data was normalized by clutch before being averaged (as described in methods and materials section).

3.3.4 Limitations of TissueGUI

A series of tests running at 200% strain/hour compared the stiffness of neural explants from stage 11 embryos and stiffness of neural explants from stage 13 embryos in mediolateral (ML) and anteroposterior (AP) directions. Data shows ML stiffness, 0.00476 ±0.0013 N/m, is greater than AP stiffness, 0.00308 ±0.0011 N/m, at stage 11($P < 0.05$). Stage 13 ML stiffness, 0.00350 ±0.0013 N/m, was similar to ML stiffness at stage 11 ($P > 0.05$). Stage 13 AP stiffness, 0.00130 ±0.0004 N/m, was significantly lower than stage 11 AP stiffness ($P < 0.05$) (Fig. 3.8). Decreased tissue stiffness in later stages of development was unlikely (Moore et al, 1995; Zhou et al, 2009) suggesting that my method for measuring stiffness was limited and needed to reconsider how I collected data.

Figure 3.7: **Determining slope on stress versus strain plots.** Linear segments taken from 0% to 2% strain and 2% to 6% strain of tests run at a strain rate of 200%/hr. (A) Linear portions taken from 0% to 2% strain are erratic compared to (B) linear portions taken from 2% to 6% strain. The black lines represent calculated slopes. Test 144 and 145 were explants from embryos of one clutch, Test 157 and 158 were explants from another clutch, and Test 162 and 163 were explants from embryos of another separate clutch.

A

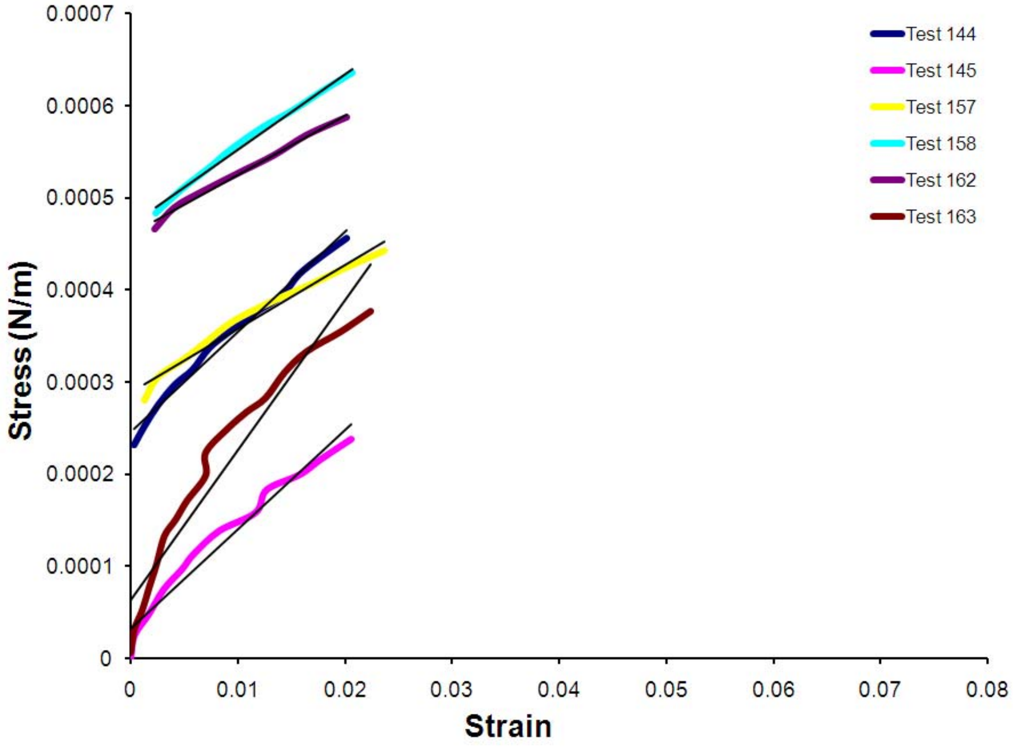

0.0007
0.0006
0.0005
0.0004
0.0003
0.0002
0.0001
0
Stress (N/m)
0
0.01
0.02
0.03
0.04
0.05
0.06
0.07
0.08
Strain
Test 144
Test 145
Test 157
Test 158
Test 162
Test 163

B

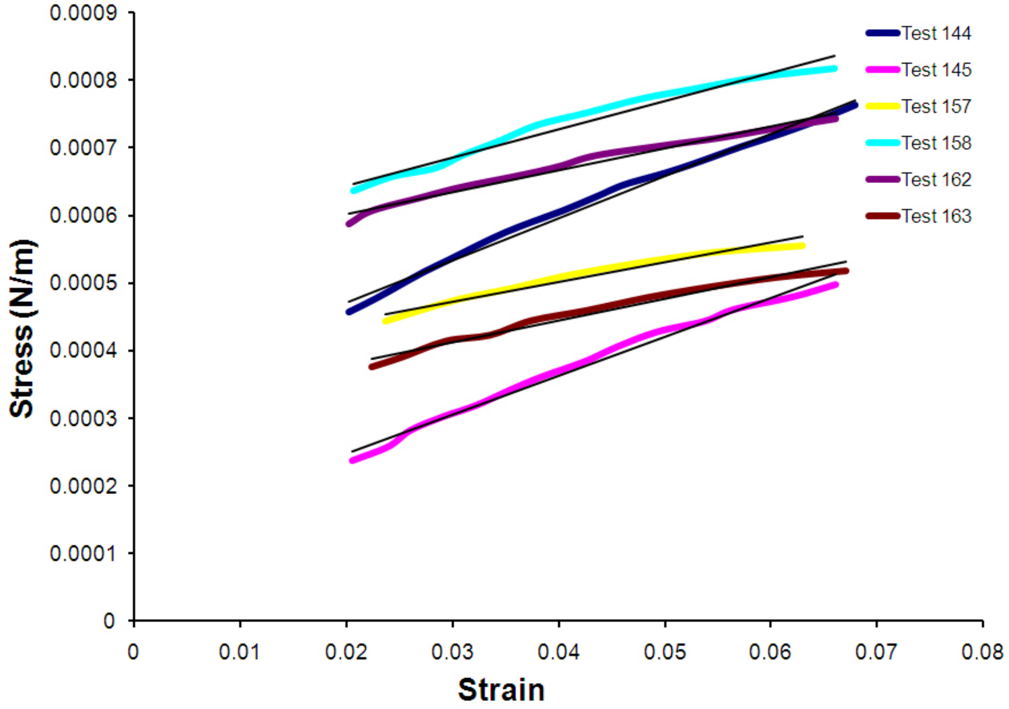

0.0009
0.0008
0.0007
0.0006
0.0005
0.0004
0.0003
0.0002
0.0001
0
Stress (N/m)
0
0.01
0.02
0.03
0.04
0.05
0.06
0.07
0.08
Strain
Test 144
Test 145
Test 157
Test 158
Test 162
Test 163

Figure 3.8: Evidence for clutch-to-clutch variability. Representative data of linear segments taken from 2% to 8% strain of tests from two different clutches. Tests 164 and 165 are from one clutch and their linear segments are clustered together. This is the same for tests 171 and 172 which are from another clutch. This shows clutch-to-clutch variation. The magnitude of measured tensile stress differs by four-fold between the two clutches, with 0.0002 to 0.0004 N/m of tensile stress over 2% to 8% strain in Test 172 compared to 0.0008 to 0.001 N/m of tensile stress over 2% to 8% strain in Test 164.

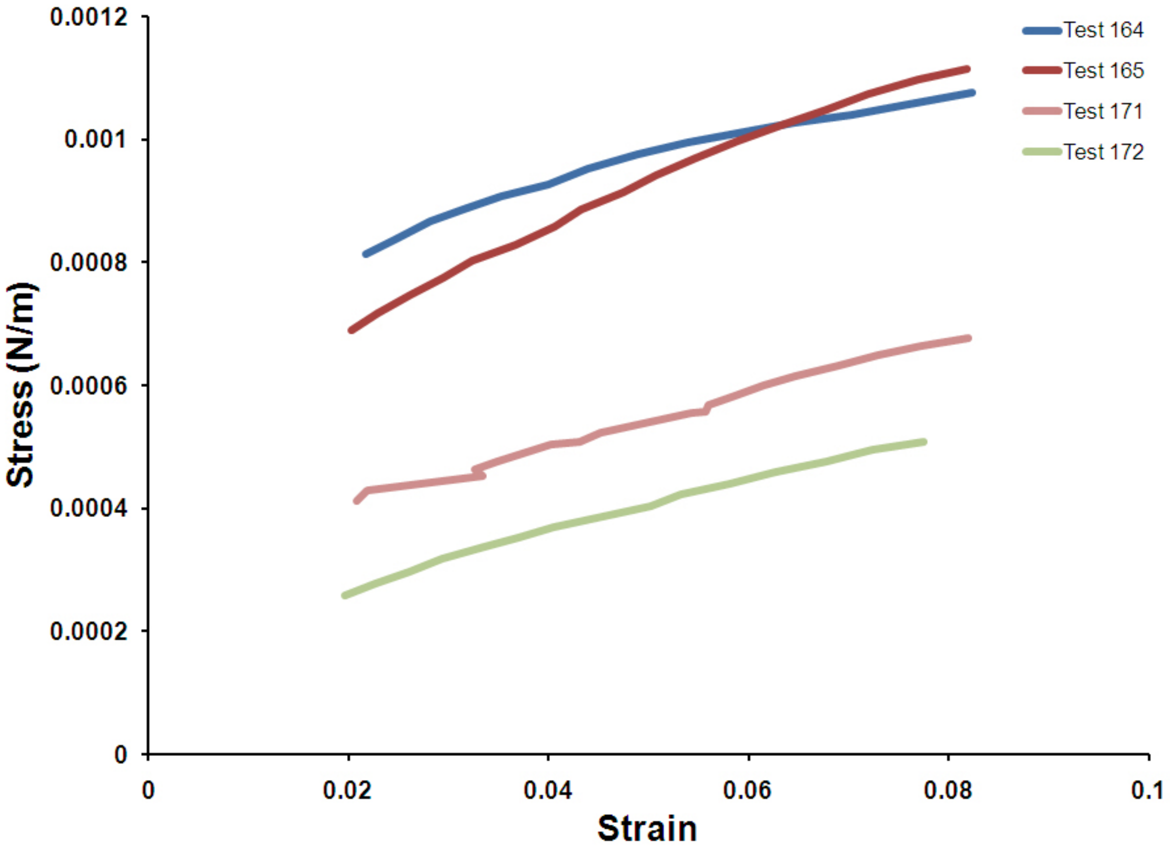
0.0012
0.001
0.0008
0.0006
0.0004
0.0002
0
Stress (N/m)
0
0.02
0.04
0.06
0.08
0.1
Strain
Test 164
Test 165
Test 171
Test 172

Figure 3.9: Directional stiffness of stage 11 and 13 embryos. Averaged data taken from 2% to 8% strain shows that ML stiffness is greater than AP stiffness at stage 11 ($P < 0.05$). At stage 13, ML stiffness remains near equal to ML stiffness at stage 11 ($P > 0.05$), but AP stiffness is significantly lower ($P < 0.05$). The error bars represent the standard error and '*' represent significant differences ($P < 0.05$).

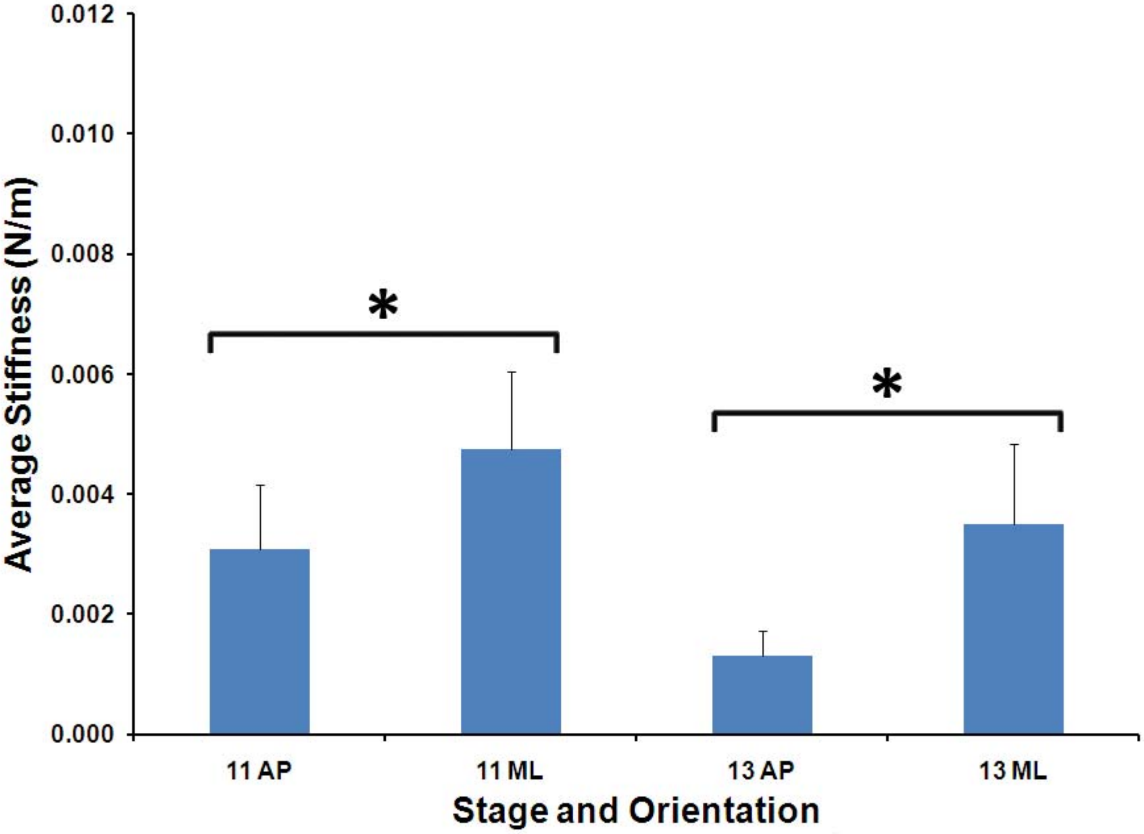
0.012
0.010
0.008
0.006
0.004
0.002
0.000
Average Stiffness (N/m)
*
*
11 AP
11 ML
13 AP
13 ML
Stage and Orientation

3.4 Results

3.4.1 TissueGUI2

TissueGUI2 is programmed to run in two phases. Phase A is similar to the method used in the previous TissueGUI program except the active wire is displaced 200 µm in 8 seconds. Phase B operates at constant strain and was incorporated to TissueGUI2 to provide a comparison to a previous method of measuring stiffness in compression studies. In those studies, stiffness was measured 3 minutes after application of stress (Moore et al, 1994, 1995; Zhou et al, 2009). A representative test is shown in Fig. 3.10.

The red trace indicates the strain in the explant calculated from wire tracking, and the blue trace indicates the tissue tension force. Phase A is represented as a linear curve nearly identical in both strain and tension. The quick drop in both traces that occurs at the initiation of Phase B is due to blacklash caused by a mechanical gap within the actuator created when changing directions. In phase B, strain is held constant within the tissue over time (horizontal red line), but tissue tension degrades over time (blue line, Fig. 3.10). This decay represents degradation of tissue integrity over time and is a normal property of biological tissue.

Figure 3.10: Sample data obtained using TissueGUI2. Representative stress and strain versus time graph from tests using the TissueGUI2 program. The red graph represents the strain of the explant over time and the blue graph represents the measured stress over time. Phase A occurs from ‘0’ to the peak (Y-axis to arrow A) where both strain and tension in the explant are linear. Phase B occurs after the peak point (arrow A to arrow B) where strain is held constant and tension in the explant degrades over time. The quick drop after the peak is due to mechanical backlash in the actuator.

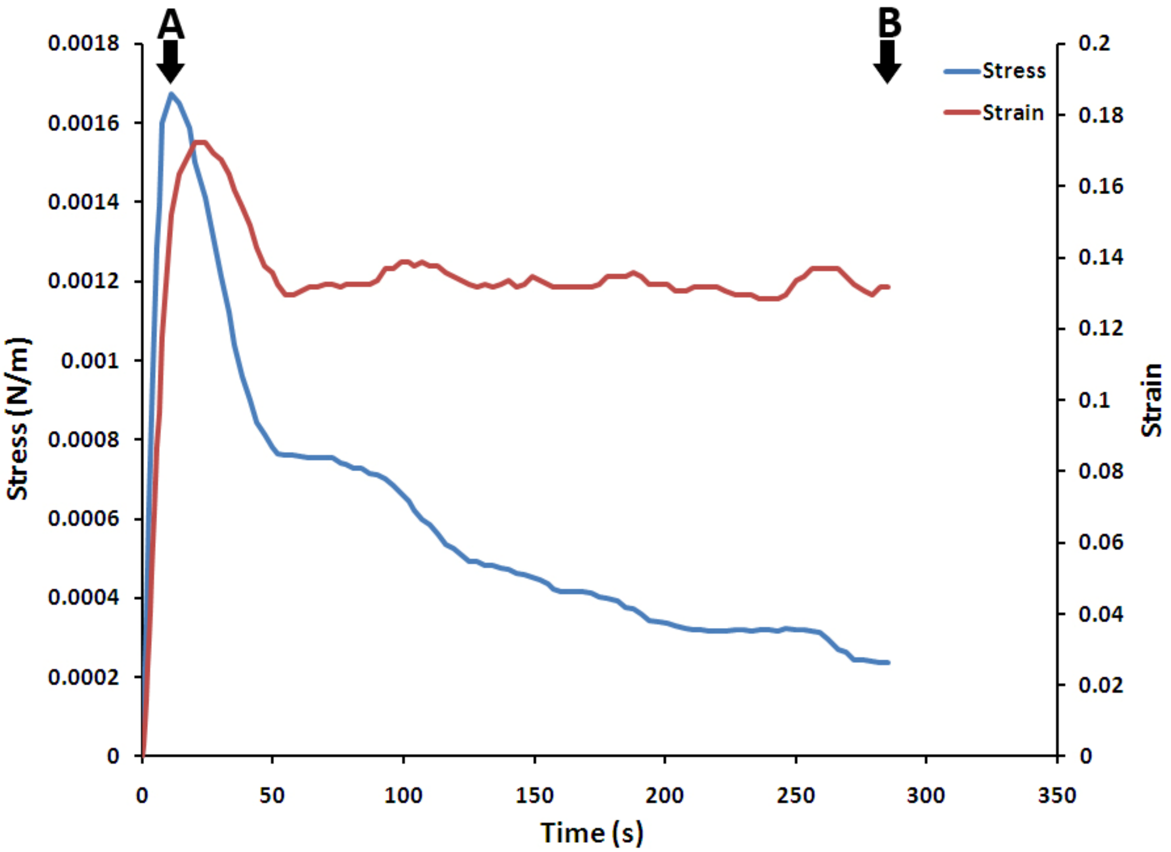
A
B
Stress
Strain
0.0018
0.0016
0.0014
0.0012
0.001
0.0008
0.0006
0.0004
0.0002
0
Stress (N/m)
0.2
0.18
0.16
0.14
0.12
0.1
0.08
0.06
0.04
0.02
0
Strain
0
50
100
150
200
250
300
350
Time (s)

3.4.2 Phase A Stiffness Measurements in Wild Type Embryos

Tissue stiffness was measured from Phase A and normalized to stage 11 ML stiffness to minimize clutch-to-clutch variation. Raw averages are presented in the Appendix. Averaged normalized data reveal increases in stiffness with developmental stage. Average ML and AP stiffness which are similar at stage 11 ($P > 0.05$) and both significantly increase by stage 13 ($P < 0.05$). ML stiffness is significantly greater than AP stiffness at stage 13 ($P < 0.05$) (Table 3.3, Fig 3.11).

Table 3.3: Average and normalized phase A stiffness measurements of explants at stage 11 and 13 in ML and AP directions.

Stage	Direction	Average Stiffness (N/m) (Mean ± Standard Deviation)	Average Normalized Stiffness (Mean ± Standard Deviation)
11	ML	0.0128 ± 0.0059	1.00
11	AP	0.0126 ± 0.0046	1.06 ± 0.4
13	ML	0.0249 ± 0.0062	2.39 ± 0.6
13	AP	0.0214 ± 0.0053	1.94 ± 0.4

Figure 3.11: Tissue stiffness increases with developmental stage. Averaged data normalized to stage 11 ML stiffness shows ML stiffness significantly increases from stage 11 (blue) to stage 13 (green), 1.00 to 2.39 ±0.6 ($P < 0.05$), and AP stiffness significantly increases from stage 11 (red) to stage 13 (purple), 1.06 ±0.4 to 1.94 ±0.4 ($P < 0.05$). ML stiffness is significantly greater than AP stiffness at stage 13 ($P < 0.05$). Error bars represent standard deviation and '*' indicates significant differences ($P < 0.05$).

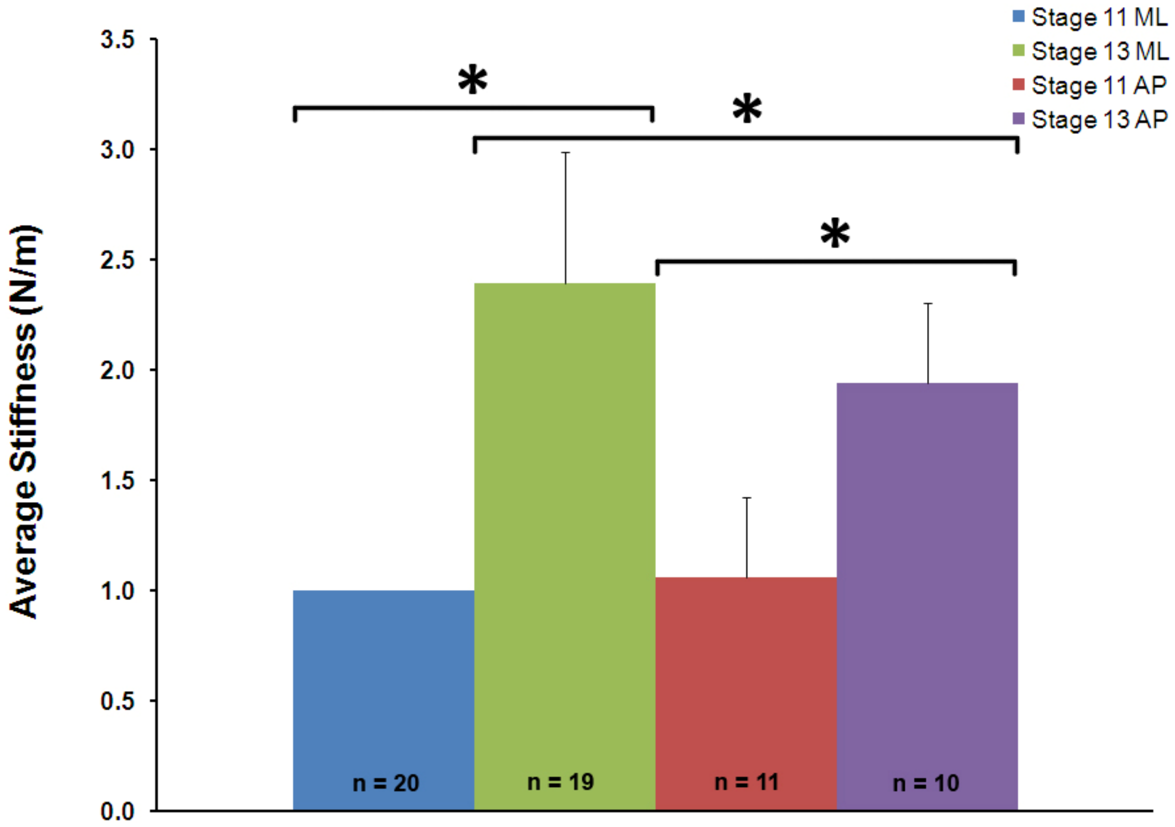
Stage 11 ML
Stage 13 ML
Stage 11 AP
Stage 13 AP
Average Stiffness (N/m)
3.5
3.0
2.5
2.0
1.5
1.0
0.5
0.0
*
*
*
n = 20
n = 19
n = 11
n = 10

3.4.3 Phase B Stiffness and Decay

Stiffness measurements were also taken in Phase B at 190 seconds similar to a previous method for measuring stiffness in compression studies. Average data normalized to stage 11 ML stiffness exhibit high variability and no trend is visible (raw averages are presented in the Appendix). ML and AP stiffness are similar at stage 11 ($P > 0.05$) and do not significantly change by stage 13 ($P > 0.05$). ML stiffness seems to be greater than AP stiffness at stage 13, but the difference is not significant ($P > 0.05$) (Table 3.4, Fig. 3.12).

Table 3.4: Average and normalized phase B stiffness measurements taken at 190 seconds of explants at stage 11 and 13 in ML and AP directions.

Stage	Direction	Average Stiffness (N/m) (Mean ± Standard Deviation)	Average Normalized Stiffness (Mean ± Standard Deviation)
11	ML	0.00560 ± 0.0048	1.00
11	AP	0.00457 ± 0.0026	1.25 ± 1.3
13	ML	0.00822 ± 0.0062	2.55 ± 1.3
13	AP	0.00374 ± 0.0019	1.41 ± 0.9

The inability to delineate changes in tissue stiffness across developmental stage is likely due to the decay in stiffness. Figure 3.13 summarizes normalized average decrease in stiffness from 45 to 190 seconds and demonstrates that the patterns of decay are unpredictable (raw averages are presented in Appendix). No trends are visible and the data exhibits high variability. The decreases in stiffness are not significantly different in both ML and AP directions from stage 11 to 13 ($P > 0.05$) nor significantly different between ML and AP directions at both stages ($P > 0.05$) (Table 3.5, Fig. 3.13).

Table 3.5: Average and normalized decrease in stiffness between 45 and 190 seconds of explants at stage 11 and 13 in ML and AP directions.

Stage	Direction	Average Stiffness (N/m) (Mean ± Standard Deviation)	Average Normalized Stiffness (Mean ± Standard Deviation)
11	ML	0.000126 ± 0.00022	1.00
11	AP	0.000211 ± 0.00022	1.31 ± 0.4
13	ML	0.000295 ± 0.00030	1.53 ± 0.6
13	AP	0.000355 ± 0.00026	2.24 ± 0.4

Figure 3.12: Phase B tissue stiffness measured at 190 seconds. ML stiffness does not significantly increase from stage 11 (blue) to stage 13 (green), 1.00 to 2.55 ±1.3 ($P > 0.05$). Similarly, AP stiffness also does not significantly change from stage 11 (red) to stage 13 (purple), 1.25 ±1.3 to 1.41 ±0.9 ($P > 0.05$). Error bars represent standard deviation.

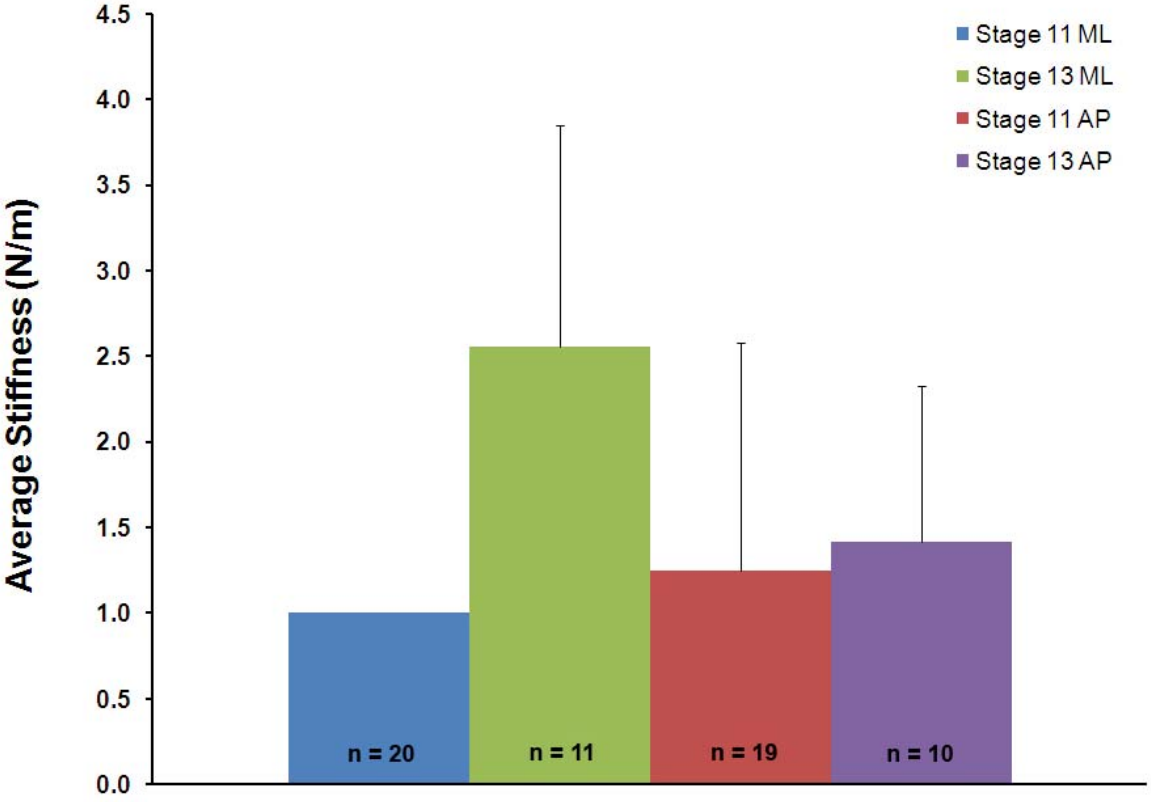
4.5
4.0
3.5
3.0
2.5
2.0
1.5
1.0
0.5
0.0
Average Stiffness (N/m)
Stage 11 ML
Stage 13 ML
Stage 11 AP
Stage 13 AP
n = 20
n = 11
n = 19
n = 10

Figure 3.13: Tissue stiffness decay in phase B. ML stiffness does not significantly increase from stage 11 (blue) to stage 13 (green), 1.00 to 1.53 ±0.6 (*P* > 0.05). Similarly, AP stiffness also does not significantly change from stage 11 (red) to stage 13 (purple), 1.31 ±0.4 to 2.24 ±0.4 (*P* > 0.05). Error bars represent standard deviation.

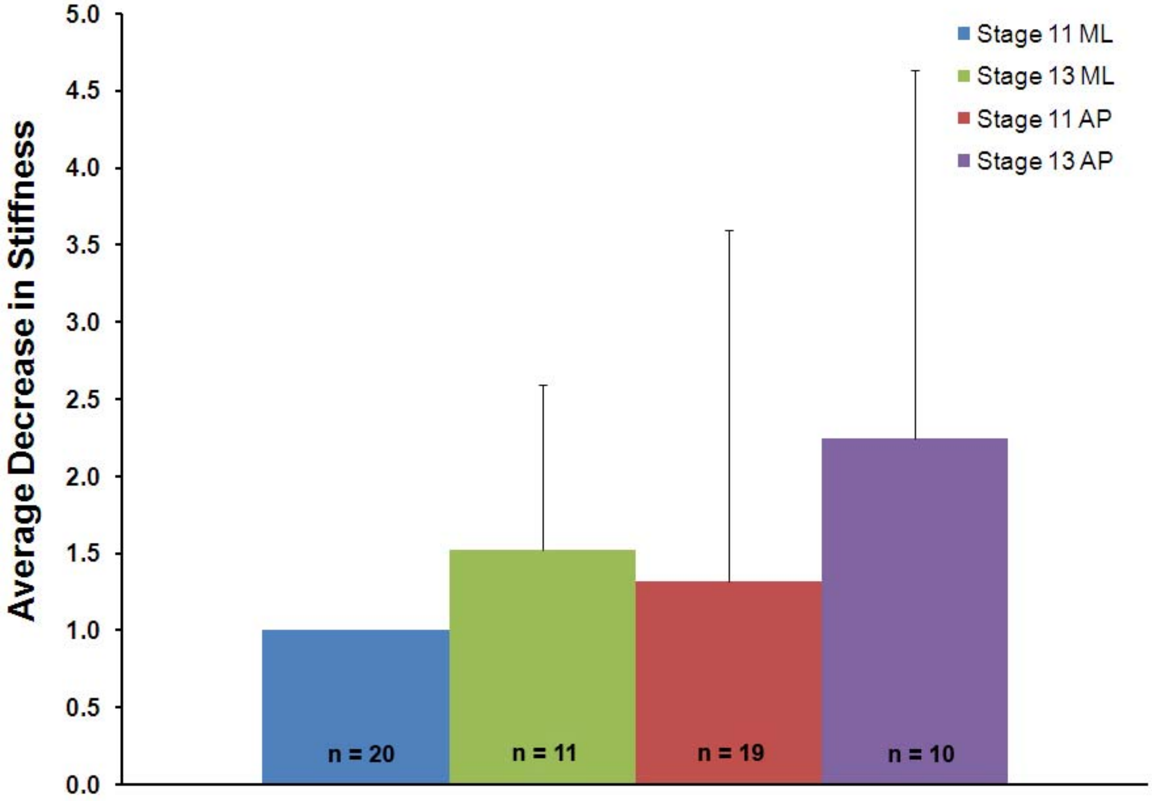
5.0
4.5
4.0
3.5
3.0
2.5
2.0
1.5
1.0
0.5
0.0
Average Decrease in Stiffness
Stage 11 ML
Stage 13 ML
Stage 11 AP
Stage 13 AP
n = 20
n = 11
n = 19
n = 10

3.4.4 Regulation of Tissue Stiffness by the PCP Signaling Pathway

To investigate what the contributions of the planar cell polarity (PCP) pathway were to the biomechanical properties of the neural plate, several dominant-negative constructs were used to block PCP signaling at three levels: outside the cell with dn*XWnt11* (Tada and Smith, 2000), at the cell membrane with dnXFz7 (Sumanas et al, 2000), and in the cytoplasm with dn*XDsh* (Wallingford and Harland, 2001, 2002). Phenotypes of developmental defects are most prominent in embryos injected with dn*XDsh*, which exhibit large abnormally shaped neural plates with neural folds that failed to migrate medially (Fig. 3.14). Similarly, embryos injected with dn*XWnt11* have large abnormally shaped neural plates with enlarged neural folds that also exhibit little medial migration (Fig. 3.14). Dn*XFz7* injected embryos also have large abnormally shaped neural plates with enlarged neural folds that exhibit reduced migration towards the midline (Fig. 3.14). At later stages, these injected embryos are truncated with open neural tube defects (Fig. 3.15).

Figure 3.14: Phenotypes of early neurula stage embryos expressing dominant-negative PCP pathway constructs. Embryos injected with the dn*XDsh* (left), dn*XWnt11* (middle), and dn*XFz7* (right) are compared to controls of the same clutch at developmental stages 12.5 (early neurulation), 14, 15, and 17 (late neurulation). Injected embryos show similar phenotypes of developmental defects including large and irregularly shaped neural plates, enlarged neural folds, and delayed neural fold migration. Neural plates are highlighted in yellow, neural folds are highlighted in blue, and epidermis is highlighted in green.

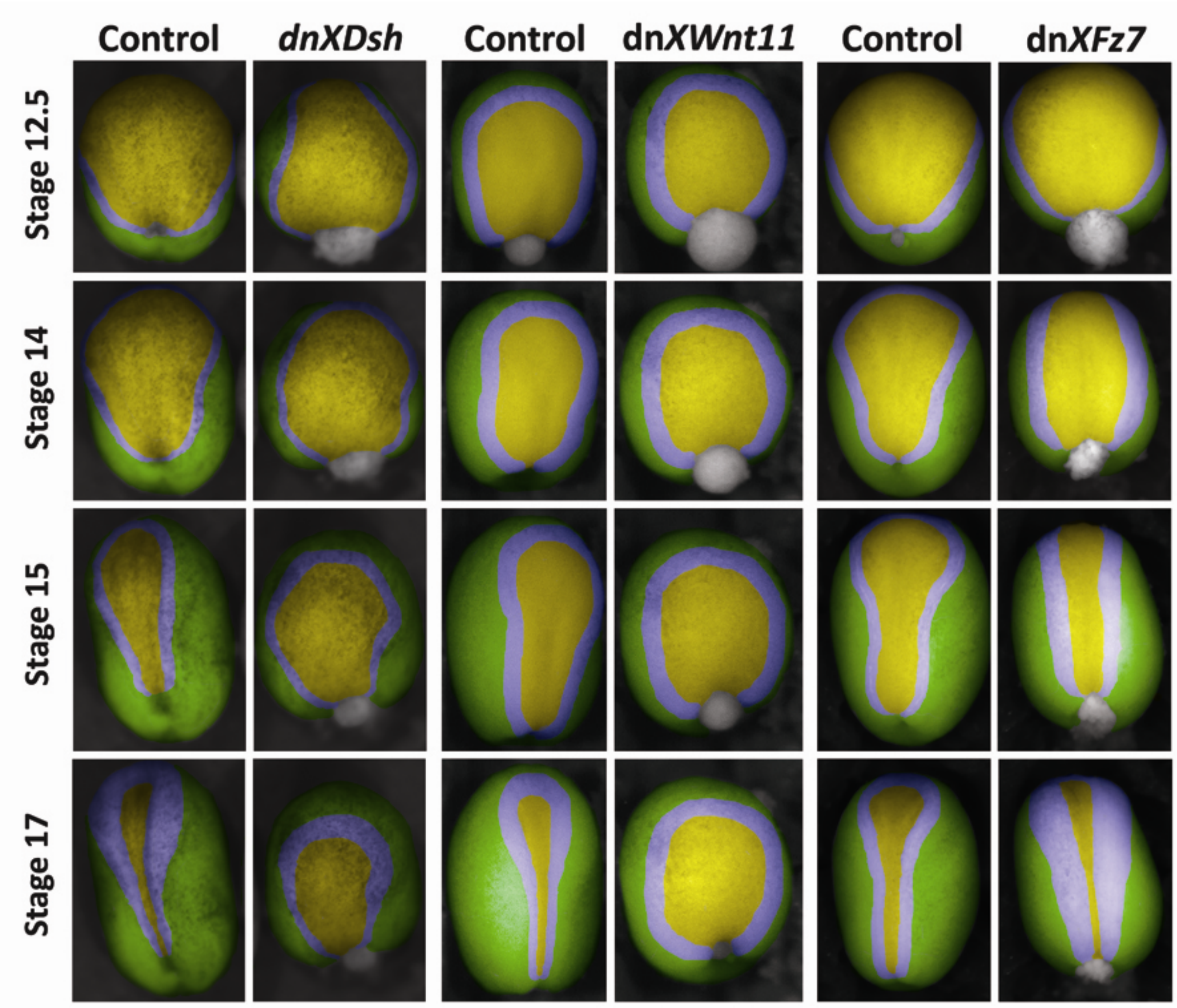
Control
dnXDsh
Control
dn*XWnt11*
Control
dn*XFz7*
Stage 12.5
Stage 14
Stage 15
Stage 17

Figure 3.15: Phenotypes of late neurula stage embryos expressing dominant-negative PCP pathway constructs. Embryos injected with the dn*XDsh* (top), dn*XWnt11* (middle), and dn*XFz7* (bottom) are compared to controls of the same clutch at developmental stage 20 (late neurulation). Injected embryos show similar phenotypes of developmental defects. They are truncated and have incomplete neural fold fusion. Neural plates are highlighted in yellow, neural folds are highlighted in blue, and epidermis is highlighted in green.

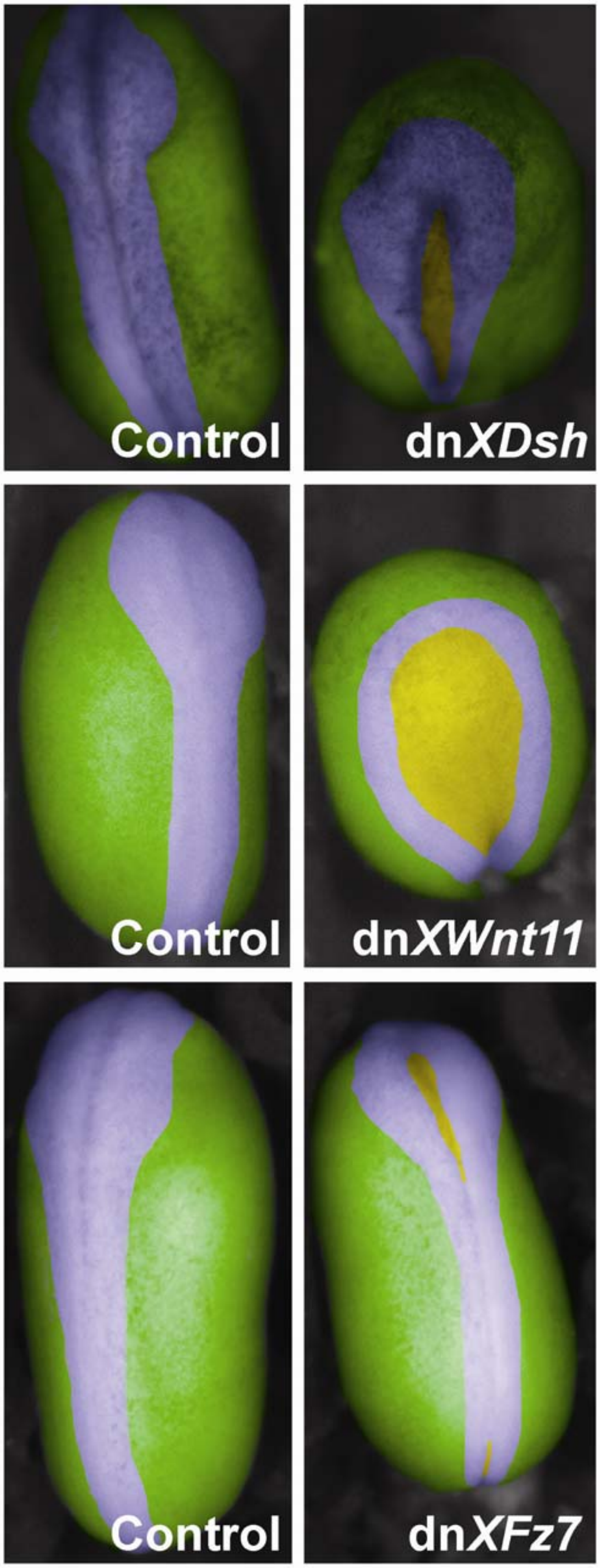
Control
dn*XDsh*
Control
dn*XWnt11*
Control
dn*XFz7*

Stiffness was measured in explants obtained from injected embryos as well as sibling controls (uninjected). Stiffness measured from dn*XDsh* injected embryos is compared to measured stiffness of control embryos first (Table 3.6, Fig. 3.16, raw averages are presented in the Appendix). Data was normalized to stage 11 ML stiffness of controls to limit clutch-to-clutch variation. Average normalized data reports that in control embryos average ML and AP stiffness are similar at stage 11 ($P > 0.05$) and do not significantly increase by stage 13 ($P > 0.05$). In dn*XDsh* injected embryos, ML and AP stiffness seem to decrease from stage 11 to stage 13 but these differences are not significant ($P > 0.05$) (Table 3.6, Fig. 3.16).

Table 3.6: The effects of a dn*XDsh* construct on tissue stiffness.

	Stage	Direction	Average Stiffness (N/m) (Mean ± Standard Deviation)	Average Normalized Stiffness (Mean ± Standard Deviation)
Control	11	ML	0.0131 ± 0.0047	1.00
	11	AP	0.0132 ± 0.0071	1.17 ± 0.8
	13	ML	0.0184 ± 0.0053	1.14 ± 0.3
	13	AP	0.0185 ± 0.0039	1.30
dn*XDsh* Injected	11	ML	0.0171 ± 0.0048	1.40 ± 0.8
	11	AP	0.0165 ± 0.0019	1.15 ± 0.8
	13	ML	0.0156 ± 0.0033	1.15 ± 0.2
	13	AP	0.0126 ± 0.0049	0.85 ± 0.4

Stiffness measurements from dn*XFz7* injected compared to stiffness measured from control embryos (Table 3.7, Fig. 3.17, raw averages are presented in the Appendix) exhibit different trends as those seen in dn*XDsh* injected embryos. In controls, average normalized ML and AP stiffness seem to increase from stage 11 to stage 13, but only ML stiffness increases significantly ($P < 0.05$).

Average normalized ML and AP stiffness of dn*XFz7* injected embryos show no increases in stiffness from stage 11 to 13 ($P > 0.05$) (Table 3.7, Fig. 3.17).

Table 3.7: The effects of a dn*XFz7* construct on tissue stiffness.

	Stage	Direction	Average Stiffness (N/m) (Mean ± Standard Deviation)	Average Normalized Stiffness (Mean ± Standard Deviation)
Control	11	ML	0.0113 ± 0.0032	1.00
	11	AP	0.0125 ± 0.0057	0.94 ± 0.2
	13	ML	0.0180 ± 0.0027	1.61
	13	AP	0.0148 ± 0.0033	1.34 ± 0.4
dn*XFz7* Injected	11	ML	0.0114 ± 0.0024	1.01 ± 0.1
	11	AP	0.0140 ± 0.0039	1.03 ± 0.2
	13	ML	0.0135 ± 0.0074	1.20 ± 0.1
	13	AP	0.0125 ± 0.0033	1.12 ± 0.2

Tissue stiffness of dn*XWnt11* injected embryos are compared to stiffness of control embryos last (Table 3.8, Fig. 3.18, raw averages are presented in the Appendix). Average normalized tissue stiffness of control embryos significantly increases from stage 11 to stage 13 ($P < 0.05$) in both ML and AP directions. There are no increases in ML and AP stiffness seen in dn*XWtn11* injected embryos ($P > 0.05$) across these stages (Table 3.8, Fig. 3.18). The dn*XWnt11* construct produces the most robust difference from controls seen among all the dominant negative constructs.

Table 3.8: The effects of a dn*XWnt11* construct on tissue stiffness.

	Stage	Direction	Average Stiffness (N/m) (Mean ± Standard Deviation)	Average Normalized Stiffness (Mean ± Standard Deviation)
Control	11	ML	0.0071 ± 0.0026	1.00
	11	AP	0.0130 ± 0.0060	1.84 ± 0.2
	13	ML	0.0200 ± 0.0055	3.48
	13	AP	0.0174 ± 0.0098	3.04
dn*XWnt11* Injected	11	ML	0.0156 ± 0.0026	2.20 ± 1.1
	11	AP	0.0159 ± 0.0063	2.26 ± 1.2
	13	ML	0.0159 ± 0.0028	2.78
	13	AP	0.0170 ± 0.0086	2.97

When comparing the overall stiffness of controls (blue) to dn*XDsh* (red), dn*XFz7* (green), and dn*XWtn11* (purple) injected embryos in ML orientation, significant increases in stiffness from stage 11 to 13 ($P < 0.05$) visible in control embryos are not seen in injected embryos (Table 3.9, Fig. 3.19, raw averages are presented in the Appendix). ML stiffness in dn*XDsh* injected embryos seems to decrease from stage 11 to 13 and increase in dn*XFz7* injected embryos; however, these differences are not significant ($P > 0.05$). Stiffness in embryos injected with dn*XWnt11* constructs are similar at stage 11 and 13 ($P > 0.05$) (Table 3.9, Fig. 3.19).

Table 3.9: Average ML stiffness of explants obtained from embryos with disrupted PCP signaling.

	Stage	Average Stiffness (N/m) (Mean ± Standard Deviation)	Average Normalized Stiffness (N/m) (Mean ± Standard Deviation)
Control	11	0.0112 ± 0.0044	1.00
	13	0.0186 ± 0.0041	1.79 ± 1.0
dn*XDsh* Injected	11	0.0171 ± 0.0048	1.40 ± 0.8
	13	0.0156 ± 0.0033	1.15 ± 0.2
dn*XFz7* Injected	11	0.0114 ± 0.0024	1.01 ±0.1
	13	0.0135 ± 0.0074	1.20 ± 0.1
dn*XWnt11* Injected	11	0.0156 ± 0.0026	2.20 ± 1.1
	13	0.0159 ± 0.0028	2.78

Similar trends are seen when comparing the overall stiffness in the AP orientation. Significant increases in AP stiffness of control embryos (blue) from stage 11 to 13 ($P < 0.05$) are not exhibited by dn*XDsh* (red), dn*XFz7* (green), and dn*XWnt11* (purple) injected embryos. Embryos injected with dn*XDsh*, dn*XFz7*, or dn*XWnt11* constructs seem to increase from stage 11 to 13 but the differences are not significant ($P > 0.05$) (Table 3.10, Fig. 3.20).

Table 3.10: Average AP stiffness of explants obtained from embryos with disrupted PCP signaling.

	Stage	**Average Stiffness (N/m)** **(Mean ± Standard Deviation)**	**Average Normalized Stiffness (N/m)** **(Mean ± Standard Deviation)**
Control	11	0.0129 ± 0.0059	1.00
	13	0.0170 ± 0.0047	1.78 ± 0.7
dn*XDsh* Injected	11	0.0165 ± 0.0019	1.26 ± 1.1
	13	0.0126 ± 0.0049	1.51 ± 1.4
dn*XFz7* Injected	11	0.0140 ± 0.0039	1.11 ±0.1
	13	0.0125 ± 0.0033	1.24 ± 0.5
dn*XWnt11* Injected	11	0.0159 0.0063	1.28 ± 0.8
	13	0.0170 ± 0.0086	1.77

Figure 3.16: The effects of a dn*XDsh* construct on tissue stiffness. ML and AP stiffness measurements of control and dn*XDsh* injected embryos shows no trend. ML stiffness does not significantly differ from stage 11 (blue columns) to stage 13 (green columns) in control embryos, 1.0 to 1.14 ±0.3 ($P > 0.05$), and dn*XDsh* injected embryos, 1.40 ±0.8 to 1.15 ±0.2 ($P > 0.05$). AP stiffness does not significantly differ from stage 11 (red columns) to stage 13 (purple columns) in control embryos, 1.17 ±0.8 to 1.30 ($P > 0.05$), and dn*XDsh* injected embryos, 1.26 ±0.78 to 0.96 ±0.43 ($P > 0.05$). Error bars represent standard deviation.

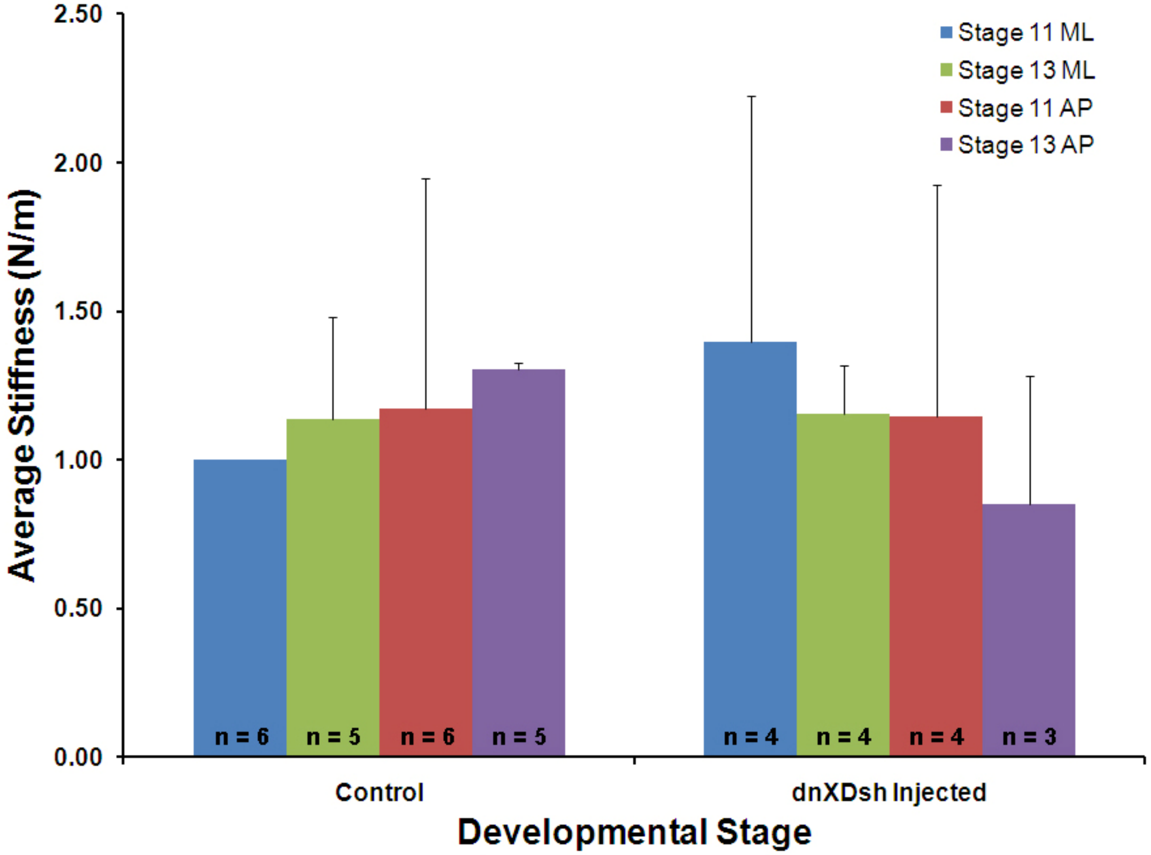
2.50
2.00
1.50
1.00
0.50
0.00
Average Stiffness (N/m)
Stage 11 ML
Stage 13 ML
Stage 11 AP
Stage 13 AP
n = 6
n = 5
n = 6
n = 5
n = 4
n = 4
n = 4
n = 3
Control
dnXDsh Injected
Developmental Stage

Figure 3.17: The effects of a dn*XFz7* construct on tissue stiffness. ML stiffness from stage 11 (blue columns) to stage 13 (green columns) significantly increases in control embryos, 1.0 to 1.61 ($P < 0.05$), but not in dn*XFz7* injected embryos, 1.01 ±0.1 to 1.20 ±0.1 ($P > 0.05$). AP stiffness does not significantly differ from stage 11 (red columns) to stage 13 (purple columns) in control embryos, 0.94 ±0.2 to 1.34 ±0.4 ($P > 0.05$), and dn*XFz7* injected embryos, 1.03 ±0.2 to 1.12 ±0.2 ($P > 0.05$). Error bars represent standard deviation and '*' indicates significant differences ($P < 0.05$).

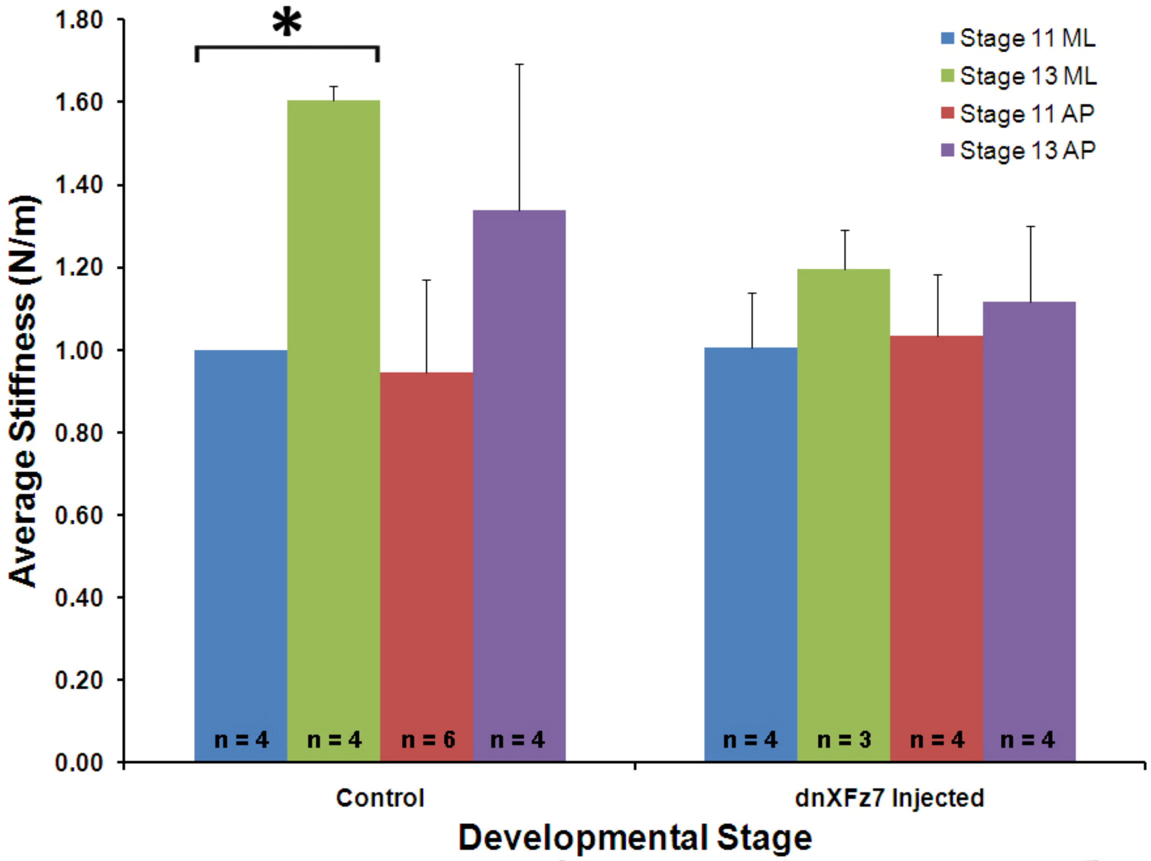
*
Stage 11 ML
Stage 13 ML
Stage 11 AP
Stage 13 AP
1.80
1.60
1.40
1.20
1.00
0.80
0.60
0.40
0.20
0.00
Average Stiffness (N/m)
n = 4
n = 4
n = 6
n = 4
n = 4
n = 3
n = 4
n = 4
Control
dnXFz7 Injected
Developmental Stage

Figure 3.18: The effects of a dn*XWnt11* construct on tissue stiffness. ML stiffness from stage 11 (blue columns) to stage 13 (green columns) significantly increases in control embryos, 1.0 to 3.48 ($P < 0.05$), but not in dn*XWnt11* injected embryos, 2.20 ±1.1 to 2.78 ($P > 0.05$). Similarly, AP from stage 11 (red columns) to stage 13 (purple columns) significantly increases in control embryos, 1.84 ±0.24 to 3.04 ($P < 0.05$), but not in dn*XWnt11* injected embryos, 2.26 ±1.2 to 2.97 ($P > 0.05$). Error bars represent standard deviation and '*' indicates significant differences ($P < 0.05$).

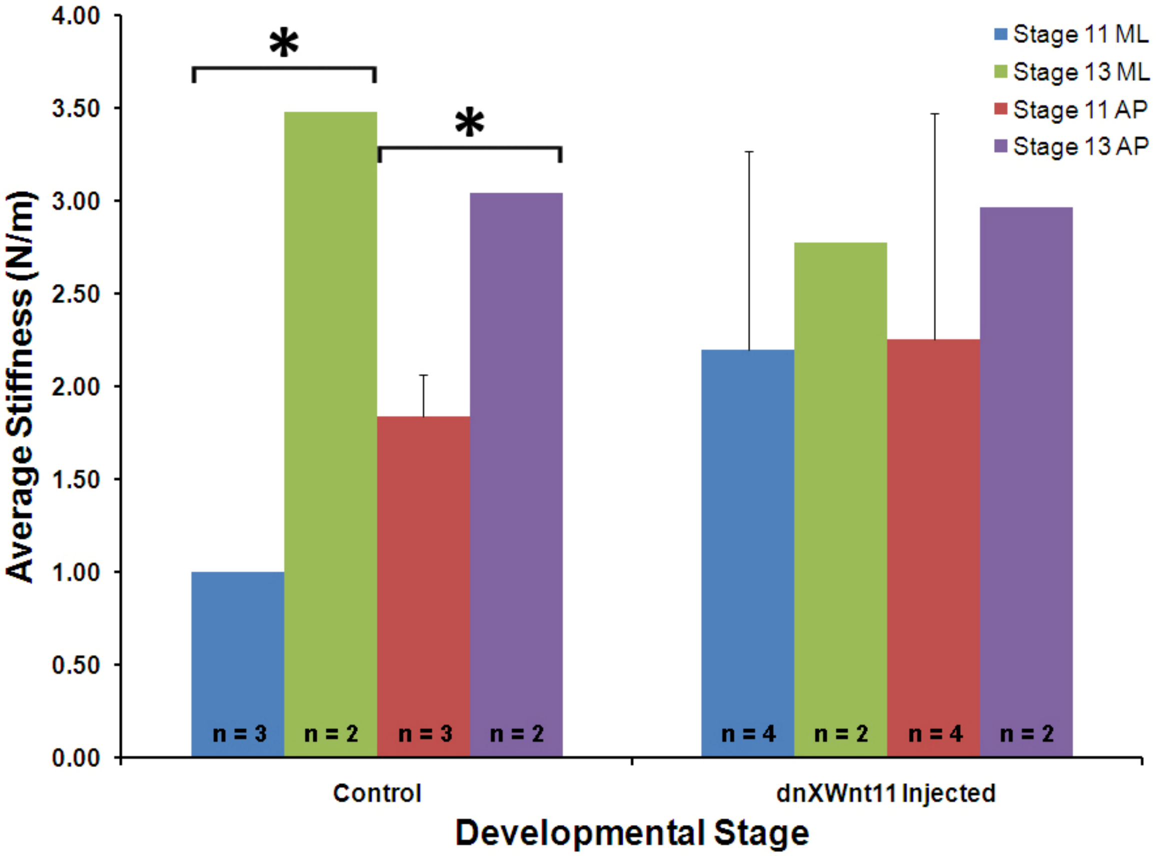
4.00
3.50
3.00
2.50
2.00
1.50
1.00
0.50
0.00
Average Stiffness (N/m)
*
*
Stage 11 ML
Stage 13 ML
Stage 11 AP
Stage 13 AP
n = 3
n = 2
n = 3
n = 2
n = 4
n = 2
n = 4
n = 2
Control
dnXWnt11 Injected
Developmental Stage

Figure 3.19: Average ML and AP stiffness of explants obtained from embryos with disrupted PCP signaling. (A) Medial-lateral tissue stiffness measurements. Average data is normalized to stage 11 ML stiffness of controls. Stiffness significantly increases from stage 11 to 13 (blue columns), 1.0 to 1.79 ±1.0 ($P < 0.05$), in control embryos. There are no significant differences in stiffness from stage 11 to 13 in dn*XDsh* injected embryos (red columns), 1.40 ±0.8 to 1.15 ±0.2 ($P > 0.05$), dn*XFz7* injected embryos (green columns), 1.01 ±0.1 to 1.20 ±0.1 ($P > 0.05$), and dn*XWnt11* injected embryos (purple columns), 2.20 ±1.1 to 2.78 ($P > 0.05$). Error bars represent standard deviation and '*' indicates significant differences ($P < 0.05$). (B) Anterior-posterior tissue stiffness measurements. Average data is normalized to stage 11 AP stiffness of control embryos. Stiffness significantly increases from stage 11 to 13 (blue columns), 1.0 to 1.78 ±0.7 ($P < 0.05$), in control embryos. There are no significant differences in stiffness from stage 11 to 13 in dn*XDsh* injected embryos (red columns), 1.26 ±1.1 to 1.51 ±1.4 ($P > 0.05$), dn*XFz7* injected embryos (green columns), 1.11 ±0.1 to 1.24 ±0.5 ($P > 0.05$), and dn*XWnt11* injected embryos (purple columns), 1.28 ±0.82 to 1.77 ($P > 0.05$). Error bars represent standard deviation and '*' indicates significant differences ($P < 0.05$).

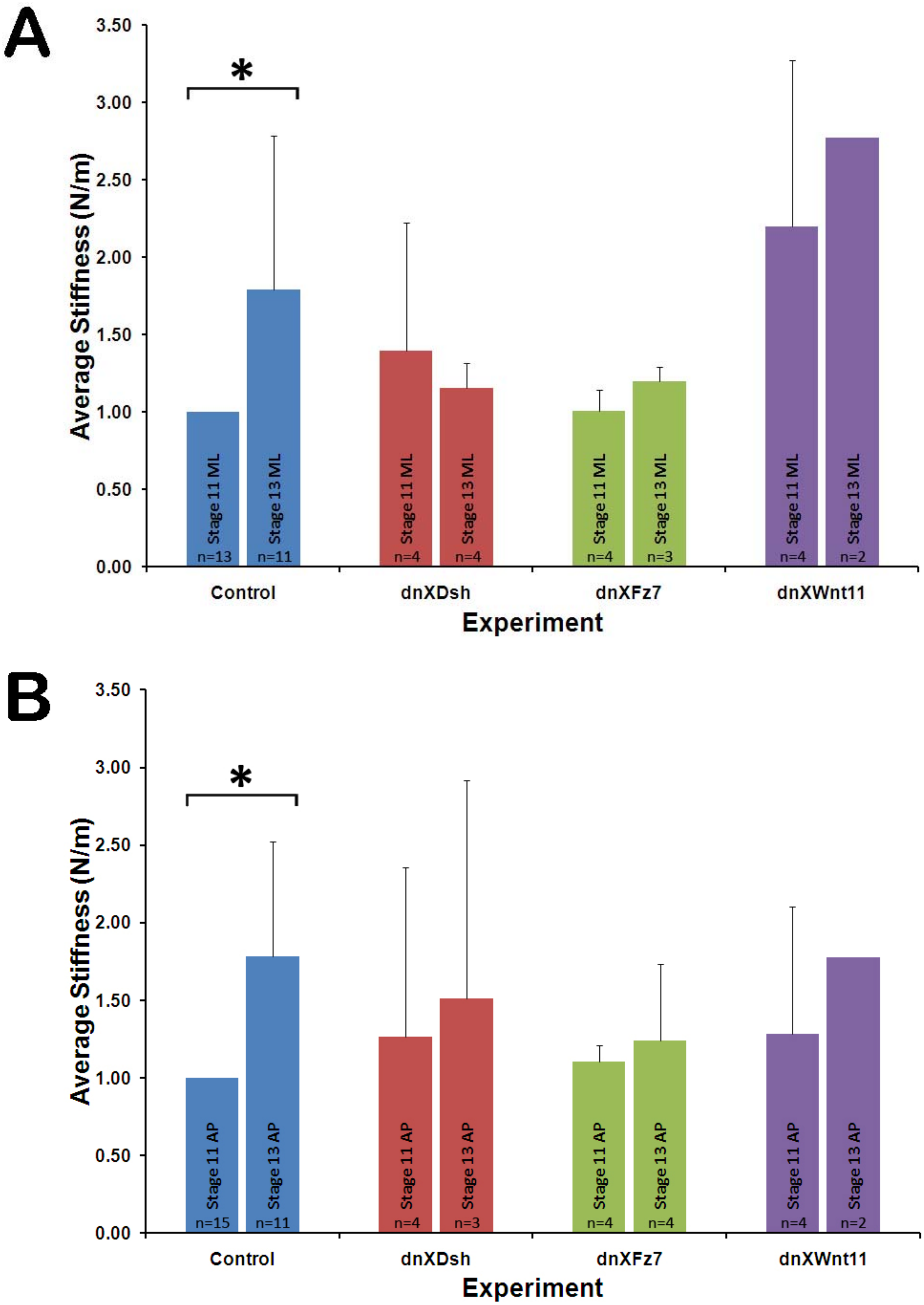
A
Average Stiffness (N/m)
3.50
3.00
2.50
2.00
1.50
1.00
0.50
0.00
*
Stage 11 ML n=13
Stage 13 ML n=11
Stage 11 ML n=4
Stage 13 ML n=4
Stage 11 ML n=4
Stage 13 ML n=3
Stage 11 ML n=4
Stage 13 ML n=2
Control
dnXDsh
dnXFz7
dnXWnt11
Experiment
B
Average Stiffness (N/m)
3.50
3.00
2.50
2.00
1.50
1.00
0.50
0.00
*
Stage 11 AP n=15
Stage 13 AP n=11
Stage 11 AP n=4
Stage 13 AP n=3
Stage 11 AP n=4
Stage 13 AP n=4
Stage 11 AP n=4
Stage 13 AP n=2
Control
dnXDsh
dnXFz7
dnXWnt11
Experiment

Chapter 4

Discussion

A primary objective of this study was to establish an experimental system to evaluate the biomechanical properties of *Xenopus* neural tissue. An experimental system was successfully developed sensitive enough to measure the mechanical stiffness of embryonic *Xenopus* neural tissue. After determining stiffness of control embryo neural plates, neurulation was disrupted by interrupting the PCP pathway. Resulting changes in neural plate stiffness were measured to determine if the forces that shape the neural plate arise from within the neural plate. I propose that cell rearrangements in the neural plate generate forces that contribute to neurulation in Xenopus.

4.1 Device Optimization

Measurement of tissue mechanical properties from small and delicate embryonic tissues requires construction of custom devices (Moore et al, 1994, 1995; Keller et al, 2000; Zhou et al, 2009). Our approach was to modify a device previously used to measure tissue stiffness in *Ambystoma mexicanum* embryos. The first modification made was to simplify the functional components of the device and ensure that the device was small enough to fit under a stereomicroscope. This was accomplished by milling a plexiglass chamber that incorporated a wire lifting mechanism and modifying the method of wire separation with the actuator using a tungsten needle (Fig. 2.1).

As this device measures tissue stiffness by attaching fine cantilever wires onto explanted tissues, the strength and consistency of attachment were optimized by investigating different types of wire and adhesives. Selection of the type of adhesive used for gluing was based on the ability to provide strong bond strength with tissues under aqueous solution. Attachment needed to be strong enough to hold explants while they were being stretched. The adhesives utilized are described in Table 3.1. UV adhesives became dilute under aqueous conditions, resulting in a bond too weak to support tissue explants. Biological adhesive C-cadherin and Mr. Sticky's Underwater Epoxy bond underwater in aqueous environments but require long cure times. A fast cure time was essential to maximize the number of tests that could be completed and ensure tests were conducted at desirable embryonic stages. Cyanoacrylate glue was found to provide the greatest bond strength and had the fastest cure times (Table 3.1). However, cyanoacrylate glue was difficult to use because it cured quickly in contact with aqueous solution. Higher viscosity cyanoacrylate glues delay curing under aqueous solution and provided greater consistently and stronger attachment. FLASH brand thick viscosity cyanoacrylate glue was the most viscous and had the strongest attachment overall and was used in all experiments.

Wire selection was based on material and modulus. The 125 µm wires used in the original design were too large for gluing onto 750 µm *Xenopus* explants. Cyanoacrylate glue would often glue the ends of large wires together because of the proximity of the wires. Finer wires maximized the area of the explanted tissue from which I could measure stiffness and reduced the tendency to glue wire ends together. Finer 75 µm wires tungsten were used to overcome this problem; however, I discovered that the material properties of wires also affected gluing. The hydrophobic oxidized surface of the tungsten wires caused cyanoacrylate glue to bead and the glue cured in a crystalline fashion causing irregular and weak bonding along the explants (Fig. 3.1A). Uniform attachment along the glue length was important to ensure an accurate measurement of stiffness. Incomplete attachment reduced the area of the explant that was actually under tension and resulted in an underestimation of calculated stiffness. Altering the surface material properties of the tungsten wires with gold/palladium did not improve glue strength. There was no beading of cyanoacrylate glue on glass and plastic fibres but glass and plastic were too buoyant and unable to break the surface tension of the solution in the chamber. Stainless steel wires allowed smooth coats of glue to form on the wire that improved attachment strength along the glue length of the explant (Fig. 3.1B). The finest manufactured stainless steel wires I could find were 63μm in diameter and these were used to manufacture cantilevers in all experiments.

4.2 Experimental Parameters

Preliminary data from initial tests that measured stiffness along the ML axis at 30% strain/hr find neural explants from developmental stages 11 (mid-gastrula), 12, and 13 (late-gastrula) are not significantly different with an average stiffness of 0.0014 N/m and large standard deviation of ±0.0015 N/m ($P > 0.05$) (Fig. 3.3). Only neural explants were compared at later stages because average stiffness measurements of deep neural and neural explants at stage 11 (mid-gastrula) were not significantly different ($P > 0.05$) (Fig. 3.3). Also, neural explants were easier and required less time to excise from whole embryos. It should be noted that my stiffness measurements are reported in N/m because we do not take into account the thickness of the tissue being stretched, but if an average explant thickness of 40-60 microns (Zhou et al, 2009) is incorporated into the calculations, very similar numbers to those reported in previous literature are obtained. However, my preliminary data did not coincide with previous findings. *Xenopus* axial dorsal mesoderm has been shown to increase in stiffness during CE. Stiffness increases in both ML and AP directions during early gastrulation with increases as much as three-fold from 3 N/m^2 at stage 10+ to 10 N/m^2 at stage 11.5 in the AP axis (Moore et al, 1995). A more recent study (Zhou et al, 2009) reports AP stiffness increases of more than six-fold from 13 to 85 N/m^2 between the late-gastrula (stage 13) to early neural tube stage (stage 22) suggesting that there is a significant increase in mesodermal stiffness through early development. Expected increases in stiffness with progressing developmental stage were not seen in preliminary tests and suggested our experimental design was not sensitive enough to discriminate between small changes in tissue stiffness.

While investigating potential sources of error, wound healing was discovered to be the primary source of error in my experiments. Wound healing occurs in explanted tissue to curl up the tissue into a ball as if to close a wound. In fact, studies show that isolated mesodermal tissue behaves much like a liquid droplet to form a spherical shape to minimize surface area and surface tension (Ninomiya and Winklbauer, 2008). In my experiments, wound healing contracts tissues to draw the two cantilever wires together and was visible in stress versus strain graphs as an initial negative sloping curve (Fig. 3.4). In tests programmed to idle at 0% strain/hr, wound healing produced negatively sloping linear curves in stress versus strain graphs, meaning the gap between the wires was decreasing at a steady rate (Fig. 3.5). This effect produced an artificial tissue stiffness calculated to be 0.0036 N/m and had an average healing rate of 35% strain/hr (representative data shown in Figure 3.5). A wound healing rate of 35% strain/hr acts against a programmed strain rate of 30% strain/hr in TissueGUI and masks any differences in tissue stiffness measured across embryonic stages (Figure 3.3). The apparent stiffness of the healing tissue is greater than the stiffness values recorded indicating that unless the effects of healing were compensated for obtaining meaningful results would be impossible. Wound healing was not an expected source of error and had not been seen in other systems that rely on compression to determine stiffness and therefore may not have been able to discriminate the contracting tissues (Moore et al, 1995; Zhou et al, 2009). To compensate for the effects of wound healing, I experimented with tests programmed to stretch tissues at higher strain rates. A strain rate of 200% strain/hr provided the maximum number of data points while successfully limiting the effects of wound healing and removing the negative slope seen at the beginning of stress versus strain graphs (Fig 3.6).

In trouble shooting the effects of wound healing, I also examined discrepancies in the criteria used to select the linear portions of stress versus strain graphs to calculate stiffness (slope) (red box, Fig. 3.2). For tests programmed to run at 200% strain/hr, calculated stiffness changed dramatically depending on what range of strain the linear segments were taken across. Stiffness calculated from 0-2% strain (Fig. 3.7A) had higher values and larger errors compared to stiffness calculated above 2% strain (Fig. 3.7B and Table 3.2). Stiffness calculations taken from 0-2% strain may be unreliable due to remaining effects of wound healing. Wound healing begins the moment tissues are excised from whole embryos. By the time wires are glued onto the explant for testing some wound healing has already occurred for a few minutes. Therefore, data points at early stages of testing at 0-2% strain would be affected the most by wound healing. Stiffness calculations taken from 2% strain to the highest strain sustained in tissues before tearing, usually 8% strain, were more consistent and became the standard method for calculating stiffness.

Although the effects of wound healing are overcome after 2% strain by high programmed strain rates of 200%, I continued to find a wide range of actual stress values from slopes taken after 2% strain (Fig. 3.7B) that result in high variation of calculated stiffness. It was determined that the variation was due to high clutch-to-clutch variation. A clear example of clutch-to-clutch variation is seen in Figure 3.8 where tests of explants from embryos of two different clutches are plotted on the same stress versus strain graph. Linear slopes from embryos of the same clutch cluster together and measured tensile stresses between clutches can differ by as much as four-fold (Fig. 3.8). Inconsistencies in biomechanical properties of *Xenopus* embryos have been documented (von

Dassow and Davidson, 2007, 2009). During data analysis, clutch-to-clutch variation was compensated for by normalizing data within each clutch before taking averages.

Tests run at 200% strain/hr find that average stiffness calculated from 2% to 8% strain did not increase in the ML direction from stage 11 to 13 ($P > 0.05$) and AP stiffness actually decreased ($P < 0.05$) (Fig. 3.9). Again, these results were inconsistent with previous findings that describe increasing ML and AP stiffness in neural tissue with greater increases in the AP direction (Moore et al, 1995; Zhou et al, 2009). Also, a greater AP stiffness at later stages was expected (Moore et al, 1995); however, my results find ML stiffness to be significantly greater than AP stiffness at stage 11 and at stage 13 ($P < 0.05$) (Fig. 3.9). Our method of measuring stiffness was limited and how data was being collected needed to be reconsidered. It was decided that data would be collected at high instantaneous strain rates to limit the effects of wound healing. Collecting data at the moment stress is applied also provided a standard method for calculating slope (stiffness) for every test that brought consistency within clutches. Data would also be collected following instantaneous strain measurements where strain is maintained at a constant rate in the tissue to provide a direct comparison of my data to that collected by previous researchers (Moore et al, 1994, 1995; Zhou et al, 2009). These programming changes were subsequently named Tissue GUI2. TissueGUI2 is programmed to run in two phases. Phase A is similar to the method used in the previous TissueGUI program except the active wire is displaced 200 μm to stretch the tissue in 8 seconds. Phase B (constant strain) was incorporated to TissueGUI2 to provide a comparison to a previous method of measuring stiffness in compression studies where stiffness is measured 180 seconds after application of stress, known as the 180-second stress-relaxation protocol (Moore et al, 1994, 1995; Zhou et al, 2009).

4.3 Directional Stiffness of the Neural Plate

Measured Phase A stiffness of control embryos from tests using TissueGUI2 show that average ML and AP stiffness are similar at stage 11 ($P > 0.05$) and increase significantly at stage 13 ($P < 0.05$) (Fig. 3.11A). These differences remain significant when data is normalized to stage 11 ML stiffness to reduce clutch-to-clutch variation ($P < 0.05$) (Fig. 3.11B). Increases in stiffness with progressing developmental stage seen are consistent with previous studies (Moore et al, 1995; Zhou et al, 2009). Although the molecular details of how the cytoskeleton generates the tensile forces pulling the cells between one another remain unclear. Evidence suggests tension originates from the cortical actin-myosin cytoskeleton generated by the tugging of cells through the protrusive activity of lamellipodia and active actin-myosin-mediated contraction that shorten and limit cell elongation. Computer modeling suggests that tractoring through lamellipodia protrusions has the mechanical capacity to drive CE (Brodland, 2006; Brodland and Veldhuis, 2006). F-actin, long filamentous polymers of actin, exhibit dynamic elastic properties (Gardel et al, 2006) and non-muscle myosin II has been found to co-localize with F-actin and generate forces that contribute to dorsal closure in *Drosophila* embryos (Franke et al, 2005). In *Xenopus* myosin IIB localizes to the cortex of intercalating cells acting to cross-link actin filaments and maintain cortical stiffness. MyosinIIB could possibly generate contraction within the cortical actin cytoskeleton in the dorsal mesodermal cells (Skoglund et al, 2008; Rolo et al, 2009). This attributes increases in tissue tension to tension generated in the cell-cortex, a mechanism that has been described as the ‘Differential Interfacial Tension Hypothesis’ (Brodland, 2002). As the neural plate undergoes CE it is possible that the tension generated by cell contractility may contribute to the increase in tissue stiffness I observe in my experiments.

Furthermore, tissue tension may also be mediated by cell-cell adhesion. A recent study (Krieg et al, 2008) addresses the 'Differential Adhesion Hypothesis' (Foty and Steinberg, 2005) using atomic force microscopy (AFM). In zebrafish embryos they determine that E-cadherin mediated cell-cell adhesion was highest in mesodermal cells and lowest in ectodermal cells, with endoderm cells displaying intermediate levels of cell adhesion. In cell sorting experiments the tissue with the highest cell-cell adhesion levels did not engulf the tissue with the lower levels of cell-cell adhesion. However, the same study reveals cell-cortex tension is driven by acto-myosin contraction and was highest in ectodermal cells, intermediate in mesodermal cells, and lowest in endodermal cells and ectoderm cells engulf mesoderm cells, suggesting cell-cortex tension has a greater influence in cell sorting experiments (Krieg et al, 2008). Taken together it is certainly possible that cell-cortex tension may play a role in mediating tissue stiffness in my experiments independent of cell-cell adhesion.

Contrary to previous literature, my data indicates there is greater ML stiffness at stage 13 than at stage 11 ($P < 0.05$). This finding suggests that the current assumption that AP stiffness is greater than ML stiffness at later stages (Moore et al, 1995) may be premature as it compares ML and AP stiffness in early-gastrula stage embryos (Moore et al, 1995). I am making a comparison of stiffness between the axial orientations of late-gastrula or neural stage *Xenopus* embryos and it is likely my results are due to measurements taken at a later developmental stage. The observed differences may also be due to differences in methodology as I stretched tissues and they compressed tissues. Due to their structure some molecules may resist tension but not compression (Vincent, 1990). The sub-cellular structures that support tension in neural cells, including the myosin filaments, actin filaments, microtubules, and cell-cell adhesion molecules may behave differently when compressed, as opposed to when they are stretched, accounting for the difference between my observations and those collected in compression. Differences in directional stiffness may also depend on differences in the intercalation of cells in mesoderm (bipolar) and in the neural plate (monopolar). Bipolar intercalation occurs in all dorsal mesodermal cells undergoing CE, but in the neural plate monopolar intercalation occurs only in lateral neural cells of the neural plate and occurs towards the notoplate (midline) where cells remain pleomorphic (Elul et al, 2000; Ezin et al, 2003, 2006). Notoplate cells do not exhibit cell intercalation and the notoplate is thought to extend along the AP axis through attachment to the underlying notochord (Ezin et al, 2003). Pleomorphic cells of the notoplate are unlikely to contribute in generating forces that drive CE causing AP axial elongation in the neural plate and may be responsible for lower AP stiffness measured in my experiments. My results clearly demonstrate neural plate tissues have biomechanical properties that contribute to morphogenesis and that these are distinct from those found in mesoderm.

In an attempt to further validate our methodology, I also took measurements over a similar time course t previous studies (Moore et al, 1995; Zhou et al, 2009). A 180-second stress-relaxation protocol for measuring stiffness is used in compression tests. Stiffness is measured 180 seconds after compression (Moore et al, 1995; Zhou et al, 2009). Measurements were taken at this time as they found the tissue responded to compression and at 180 seconds this response had subsided. When I measured stiffness in Phase B of my experiments, average and normalized ML and AP stiffness was not significantly different from stage 11 to 13 ($P > 0.05$) although my results exhibit high variation (Fig. 3.12). The high variation from measurements taken in phase B is similar to the variation seen in compression studies (Moore et al, 1995; and Zhou et al, 2009). One of the advantages of my approach is that my experiments demonstrate this variance is due to the decay in stiffness over time (Fig. 3.10). As constant strain is sustained within the tissue (red line, Fig. 3.10) stress is observed to decrease over time (blue line, Fig. 3.10). A decrease of stress in the tissue represents a decrease in tissue stiffness. Decay in stiffness likely results from natural degradation of tissue integrity over time in response to stress. Explants that have been stretched twice exhibit a much lower stiffness the second time suggesting the mechanical properties of the tissue have degraded due to stress (data not shown). The amount of decay that occurs is variable in phase B, meaning the rates at which tissues degrade are unpredictable. This is most evident in the raw data separated by clutch (Fig. A1.2A and Fig. A1.3A). For example, AP stiffness at stage 11 of clutch 7 embryos was unusually higher than stiffness at stage 13 (Fig. A1.2A). This was due to greater decay at stage 13 than at stage 11 of clutch 7 embryos (Fig. A1.3A). Similar observations have been made in compression studies in mesoderm (von Dassow and Davidson, 2007, 2009). Furthermore, limitations of our experimental method may contribute to variable amounts of degradation of tissue stiffness. Gluing may not always result in complete attachment of the wires to the tissue explant and it is observed that attachment weakens over time and the explant eventually separates from the wires. Tearing of the tissue at the site of attachment during testing has also been observed and may be a source of degradation of stress seen in Phase B.

The 180-second stress-relaxation protocol for measuring stiffness used in compression studies refers to this decay as tissue ‘response’ to applied stress and measurements are taken at 180 seconds after the ‘response’ subsides (Moore et al, 1995). Similar patterns of decay are observed in my analysis where degradation seems to plateau as stress approaches zero. However, decay or ‘response’ never completely subsides and waiting for degradation to settle seemed impractical. The sources of degradation are unknown, but I demonstrate it can account for unreliable stiffness measurements in Phase B. This is why I restrict my analysis to Phase A stiffness, at the instant stress is applied.

4.4 PCP Affects Neural Plate stiffness

The PCP pathway is known to regulate CE in the neural plate (Habas et al, 2001; Habas et al, 2003) and the disruption of PCP signaling randomizes lamellipodia (Wallingford and Harland, 2001; Wallingford, 2006). When PCP is disrupted neural tissue cannot generate the forces required for proper neurulation (Keller et al, 2008). It is expected that blocking PCP signaling would eliminate the differences in stiffness in neural tissue in the ML versus AP orientation. I first looked at the phenotypic effects of disrupting PCP signaling by using a dominant-negative constructs to block PCP signaling at three levels: outside the cell with dn*XWnt11* (Tada and Smith, 2000) at the cell membrane with dnXFz7 (Djiane et al, 2000) and in the cytoplasm with dn*XDsh* (Wallingford and Harland, 2001, 2002). Phenotypes of injected embryos were similar exhibiting large abnormally shaped neural plates with neural folds that had little medial migration compared to controls (Fig. 3.14). At stage 17 (early-neurula stage), injected embryos were truncated compared to sibling controls and possessed neural tube defects. The ability of the neural folds to elevate was not affected suggesting apical constriction occurred normally in the neural plate. Control embryos exhibit AP elongation and have closed neural tubes (Fig. 3.15). Injected embryos have open neural tubes and exhibit little AP elongation (Fig. 3.15). The shortened axis and lack of medial neural fold medial migration indicates that there has been a generalized failure in CE movements in the embryo. My dominant negative construct injections target the neural plate and it is therefore likely that this failure stems from the disruption of the biomechanical properties of the neural plate.

To determine what effects disrupting PCP had on the biomechanical properties of the neural plate, I measured stiffness in explants derived from injected embryos as well as controls from the same clutch. After normalizing to stage 11 ML stiffness of controls, ML and AP stiffness exhibit increases from stage 11 to 13 in control embryos ($P < 0.05$) (blue, Fig. 3.19B and Fig. 3.20B) correlating well with my previous results. Embryos injected with dn*XDsh* (red), dn*XFz7* (green), and dn*XWnt11* (purple) constructs exhibits no increases in ML and AP stiffness from stage 11 to 13 ($P > 0.05$) (Fig. 3.19B and Fig. 3.20B). Disrupting PCP outside the cell, at the cell membrane, and inside the cell by expressing dn*XWnt11*, dn*XFz7*, and dn*XDsh* indicates that failure of CE is directly correlated with decreases in forces generated in the neural plate. As disruption of PCP signaling leads to decreased Rac and Rho function the decreased stiffness maybe due to misregulation of the cortical actin cytoskeleton. In vertebrates, apical accumulation of Rho in the neural plate is required for cell shape change and proper neural tube formation (Kinoshita et al, 2008). Furthermore decreased actin reorganization randomizes lamellipodia (Wallingford and Harland, 2001; Wallingford, 2006). Neural cells with randomized lamellipodia would behave similarly to pleomorphic cell and do not exhibit polarized traction. In the presence of dominant negative constructs uncoordinated protrusive activity of the lamellipodia inhibits cell intercalation disrupting CE and results in no increases in stiffness through stage 11 to 13. Also, decreased cytoskeletal reorganization during CE would compromise cell-cortex tension. In *Xenopus*, inhibiting myosin IIB function disrupts cortical actin cytoskeleton polarity and reduces cell-cell adhesion (Skoglund et al, 2008) and reduced F-actin or Myosin II contractility reduces AP stiffness in dorsal tissues by 50 percent in a dose-dependent manner (Zhou et al, 2009). This supports PCP's role in modulating the biomechanical properties of the neural plate and shows that forces that shape neural plate arise from within it. However, how *XWnt11*, *XFz7*, and *XDsh* exactly function to modulate the biomechanical properties or the generation of these forces in the neural plate is still unknown.

My study provides evidence and a quantitative measure of the differences in the biomechanical properties of the neural plate regulated by *XWnt11*, *XFz7*, and *XDsh*. Although the differences are not significant, an apparent increase in stiffness of dn*XDsh* and dn*XWnt11* injected embryos compared to controls at stage 11 is a common trend observed when comparing both ML and AP stiffness (Fig. 3.19B and Fig. 3.20B). Normalized data comparing dn*XDsh* injected and control embryos (Fig. 3.16B) exhibit the same trend; however, expected increases in stiffness with stage in controls are not significant ($P > 0.05$) and most likely due natural variations in biomechanical properties of *Xenopus* embryos. Normalized data comparing dn*XWnt11* injected and control embryos do exhibit expected increases in both ML and AP stiffness from stage 11 to 13 in controls ($P < 0.05$) and exhibits a trend, similar to dn*XDsh* experiments, of greater ML and AP stiffness of dn*XWnt11* injected embryos than controls at stage 11 (Fig. 3.18B). Conversely, normalized data comparing dn*XFz7* injected and control embryos exhibit similar ML and AP stiffness at stage 11 (Fig. 3.17B). ML and AP stiffness of dn*XFz7* injected embryos remains similar to controls at stage 11.

These trends may be explained by the differences in the molecular function of Wnt, *Fz*, and *Dsh*. Since *Fz* functions primarily as Wnt's receptor signaling downstream to activate *Dsh* (Wallingford and Habas, 2005) its disruption would be the most specific in interrupting PCP signaling and failed CE. ML and AP stiffness are similar between control and dn*XFz7* injected embryos at stage 11 prior to the onset of CE. At stage 13, control embryos exhibit increases in ML and AP stiffness due to active CE while dn*XFz7* injected embryos exhibit no increases in stiffness due to disrupted CE. Wnt proteins function in multiple signaling pathways that control several aspects of development including proliferation, fate specification, polarity, and migration of cells (reviewed by Logan and Nusse, 2004). Disrupting Wnt11 function with the construct that I used could potentially block many Wnt pathways as how the construct acts is unclear. Therefore, reasons for the apparent increases in ML and AP stiffness of dn*XWnt11* injected embryos compared to controls at stage 11 exhibited in my experiments are unclear. Wnt11 is known to regulate the turnover of cadherins and if this is disrupted it may result in increased cell-cell adhesion. This could be clarified with experiments that examine the turnover of C-cadherin in the embryo. However, increases in ML and AP stiffness in controls from stage 11 to 13 are not exhibited by dn*XWnt11* injected embryos suggesting disruption of CE. Similarly, ML and AP stiffness measurements of dn*XDsh* injected and control embryos show the same trend. Disruptions of *Dsh* would also have a variety of effects as it functions in not only in PCP signaling, but also in canonical Wnt signaling (reviewed by Wallingford and Habas, 2005). In canonical Wnt signaling, *Dsh* signals downstream to block cytoplasmic β-catenin phosphorylation. β-catenin accumulates and traffics into the nucleus to initiate transcription of a variety of Wnt-target genes (Itoh et al, 2005). Other non-conical pathways, such as Wnt-Ca^{2+} signaling, that may influence the canonical and PCP pathways have been emerging (Miller et al, 1999a; Wallingford and Habas, 2005). Therefore the disruption of *Dsh* is the least specific, making it difficult to decipher how it is responsible for the increases seen prior to stage 11. Increased stiffness prior to CE may be responsible for failed neural tube closure by creating tissue too stiff for morphogenetic movements to occur and the tissue then resists deformation. An initial stiffer tissue may explain wider neural folds exhibited in injected embryos. It is possible that a temporal and spatial optimal level of stiffness is necessary for proper neurulation to occur. This is supported by the observation that stimulation and inhibition of the PCP leads to the same phenotypes (Roszko et al, 2009). Ultimately, my experiments reinforce PCP's role in modulating the biomechanical properties of the neural plate and specific molecules of the PCP pathway regulate these properties differently.

4.5 Conclusion

We were successful in developing an experimental method to measure tissue stiffness in Xenopus embryos. The design was sensitive enough to discriminate small differences in stiffness between mediolateral and anteroposterior axial orientations, as well as developmental stage. My experiments describe the forces behind wound healing, and are the first observation that describes this process in mechanical terms. Control embryos show equivalent stiffness in both the ML and AP axis measurements at stage 11 before CE occurs. Stiffness increased at stage 13 coincident with CE, with greater stiffness in the ML direction. Embryos injected with dominant-negative constructs of *Wnt11*, *Fz7* and *Dsh*, showed little change in stiffness in both ML and AP directions. This suggests PCP is responsible for modulating or initiating these differences. Overall, this study provides evidence that the forces that shape the neural plate arise from within neural tissue.

4.6 Future Direction

The optimization of this device opens many avenues for the investigation of the biomechanical forces in embryonic tissues. The use of the device is limited only by the size of the tissue in question. Immediate questions that arise from my work are: does the neural plate continue to become stiffer with more advanced developmental stage? If so, how do ML and AP stiffness compare at later stages? What is the source of the stiffness in the ML direction? How does PCP regulate tissue stiffness? Future experiments could investigate the effects of over-expression or knockout of *Wnt*, *Fz*, and *Dsh* and if the effects could be rescued using downstream PCP molecules such as Rac and Rho. Answering these questions will lead to a better understanding of how molecular mechanisms mediate changes in the biomechanical properties of the neural plate.

Appendix A

Raw Data

Table A1.1: Average Phase A stiffness of explants at stage 11 and 13 in ML and AP directions by clutch.

Clutch	Stage	Direction	Average Stiffness (N/m) (Mean ± Standard Deviation)
4	11	ML	0.0115 ± 0.0014
	11	AP	0.00893 ± 0.0034
	13	ML	0.0312 ± 0.011
	13	AP	0.0238 ± 0.012
6	11	ML	0.0098 ± 0.0039
	11	AP	0.0122 ± 0.0055
	13	ML	0.0222 ± 0.0036
	13	AP	0.0182 ± 0.0046
7	11	ML	0.0074 ± 0.0048
	11	AP	0.0133 ± 0.0032
	13	ML	0.0221 ± 0.0076
	13	AP	0.0175 ± 0.00092
9	11	ML	0.0155 ± 0.0012
	11	AP	0.0160 ± 0.00049
	13	ML	0.0251 ± 0.0045
	13	AP	0.0232 ± 0.0049
Average	11	ML	0.0128 ± 0.0059
	11	AP	0.0126 ± 0.0046
	13	ML	0.0249 ± 0.0062
	13	AP	0.0214 ± 0.0053

Figure A1.1: Average Phase A stiffness of explants at stage 11 and 13 in ML and AP directions. (A) Phase A stiffness measured in embryos from four separate clutches (clutch 4, 6, 7, and 9). ML stiffness increased from stage 11 (blue) to stage 13 (green) in all clutches: 0.0115 ±0.0014 N/m to 0.0312 ±0.011 N/m ($P > 0.05$) in clutch 4, 0.0098 ±0.0039 N/m to 0.0222 ±0.0036 N/m ($P > 0.05$) in clutch 6, 0.0074 ±0.0048 N/m to 0.0221 ±0.0076 N/m ($P > 0.05$) in clutch 7, and 0.0155 ±0.0012 N/m to 0.0251 ±0.0045 N/m ($P > 0.05$) in clutch 9. Similarly, AP stiffness increased from stage 11 (red) to stage 13 (purple) in all clutches: 0.00893 ±0.0034 N/m to 0.0238 ±0.012 N/m ($P > 0.05$) in clutch 4, 0.0122 ±0.0055 N/m to 0.0182 ±0.0046 N/m ($P > 0.05$) in clutch 6, 0.0133 ±0.0032 N/m to 0.0175 ±0.00092 N/m ($P > 0.05$) in clutch 7, 0.0160 ±0.00049 N/m to 0.0232 ±0.0049 N/m ($P > 0.05$) in clutch 9. Error bars represent standard deviation. (B) Increases in ML and AP stiffness from stage 11 to 13 are exhibited when data is averaged across clutches and the differences are significant ($P < 0.05$). Average ML stiffness increases from 0.0128 ±0.0059 N/m at stage 11 (blue) to 0.0249 ±0.0062 N/m at stage 13 (green) ($P < 0.05$). Similarly, average AP stiffness increases from 0.0126 ±0.0046 N/m at stage 11 (red) to 0.0214 ±0.0053 at stage 13 (purple) ($P < 0.05$). Error bars represent standard deviation and ‘*’ indicates significant differences ($P < 0.05$).

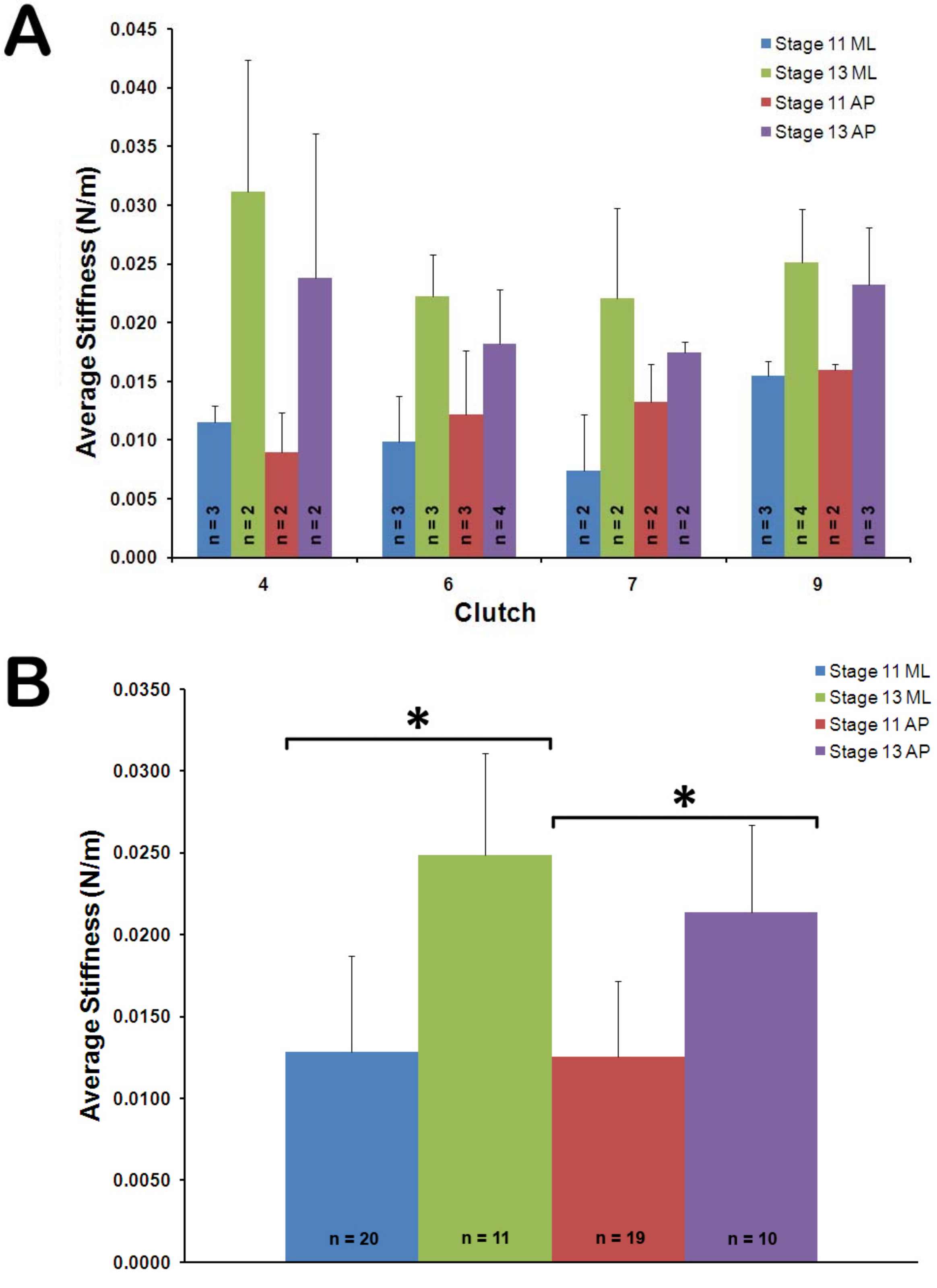
A
0.045
0.040
0.035
0.030
0.025
0.020
0.015
0.010
0.005
0.000
Average Stiffness (N/m)
Stage 11 ML
Stage 13 ML
Stage 11 AP
Stage 13 AP
n = 3
n = 2
n = 2
n = 2
n = 3
n = 3
n = 3
n = 4
n = 2
n = 2
n = 2
n = 2
n = 3
n = 4
n = 2
n = 3
4
6
7
9
Clutch
B
0.0350
0.0300
0.0250
0.0200
0.0150
0.0100
0.0050
0.0000
Average Stiffness (N/m)
Stage 11 ML
Stage 13 ML
Stage 11 AP
Stage 13 AP
*
*
n = 20
n = 11
n = 19
n = 10

Table A1.2: **Average Phase B (190 seconds) stiffness of explants at stage 11 and 13 in ML and AP directions by clutch.**

Clutch	Stage	Direction	Average Stiffness (N/m) (Mean ± Standard Deviation)
4	11	ML	0.00390 ± 0.0016
	11	AP	0.00298 ± 0.0012
	13	ML	0.0168 ± 0.010
	13	AP	0.00540 ± 0.0029
6	11	ML	0.00407 ± 0.0011
	11	AP	0.00418 ± 0.0031
	13	ML	0.00885 ± 0.00099
	13	AP	0.00403 ± 0.0046
7	11	ML	0.000981 ± 0.0012
	11	AP	0.00441 ± 0.00041
	13	ML	0.00247 ± 0.0029
	13	AP	0.00264 ± 0.00021
9	11	ML	0.00525 ± 0.0031
	11	AP	0.00601 ± 0.0011
	13	ML	0.00633 ± 0.0034
	13	AP	0.00309 ± 0.0015
Average	11	ML	0.00560 ± 0.0048
	11	AP	0.00457 ± 0.0026
	13	ML	0.00822 ± 0.0062
	13	AP	0.00374 ± 0.0019

Figure A1.2: Average Phase B (190 seconds) stiffness of explants at stage 11 and 13 in ML and AP directions. (A) Phase B stiffness measured in embryos from clutch 4, 6, 7, and 9 showed high variability and no trends. There are no significant differences in ML stiffness from stage 11 (blue) to stage 13 (green) in all clutches: 0.00390 ±0.0016 N/m to 0.0168 ±0.010 N/m ($P > 0.05$) in clutch 4, 0.00407 ±0.0011 N/m to 0.00885 ±0.00099 N/m ($P > 0.05$) in clutch 6, 0.00981 ±0.0012 N/m to 0.00247 ±0.0029 N/m ($P > 0.05$) in clutch 7, and 0.00525 ±0.0031 N/m to 0.00633 ±0.0034 N/m ($P > 0.05$) in clutch 9. Similarly, there are no significant differences in AP stiffness from stage 11 (red) to stage 13 (purple) in all clutches: 0.00298 ±0.0012 N/m to 0.00540 ±0.0029 N/m ($P > 0.05$) in clutch 4, 0.00418 ±0.0031 N/m to 0.00403 ±0.0046 N/m ($P > 0.05$) in clutch 6, 0.00441 ±0.00041 N/m to 0.00264 ±0.00021 N/m ($P > 0.05$) in clutch 7, 0.00601 ±0.0011 N/m to 0.00309 ±0.0015 N/m ($P > 0.05$) in clutch 9. Error bars represent standard deviation. (B) Averaged data across clutches reveals high variability and no trend. Average ML stiffness changes from 0.00560 ±0.0048 N/m at stage 11 (blue) to 0.00822 ± 0.0062 N/m at stage 13 (green) ($P > 0.05$). Average AP stiffness changes from 0.00457 ±0.0026 N/m at stage 11 (red) to 0.00374 ±0.0019 at stage 13 (purple) ($P > 0.05$). Error bars represent standard deviation.

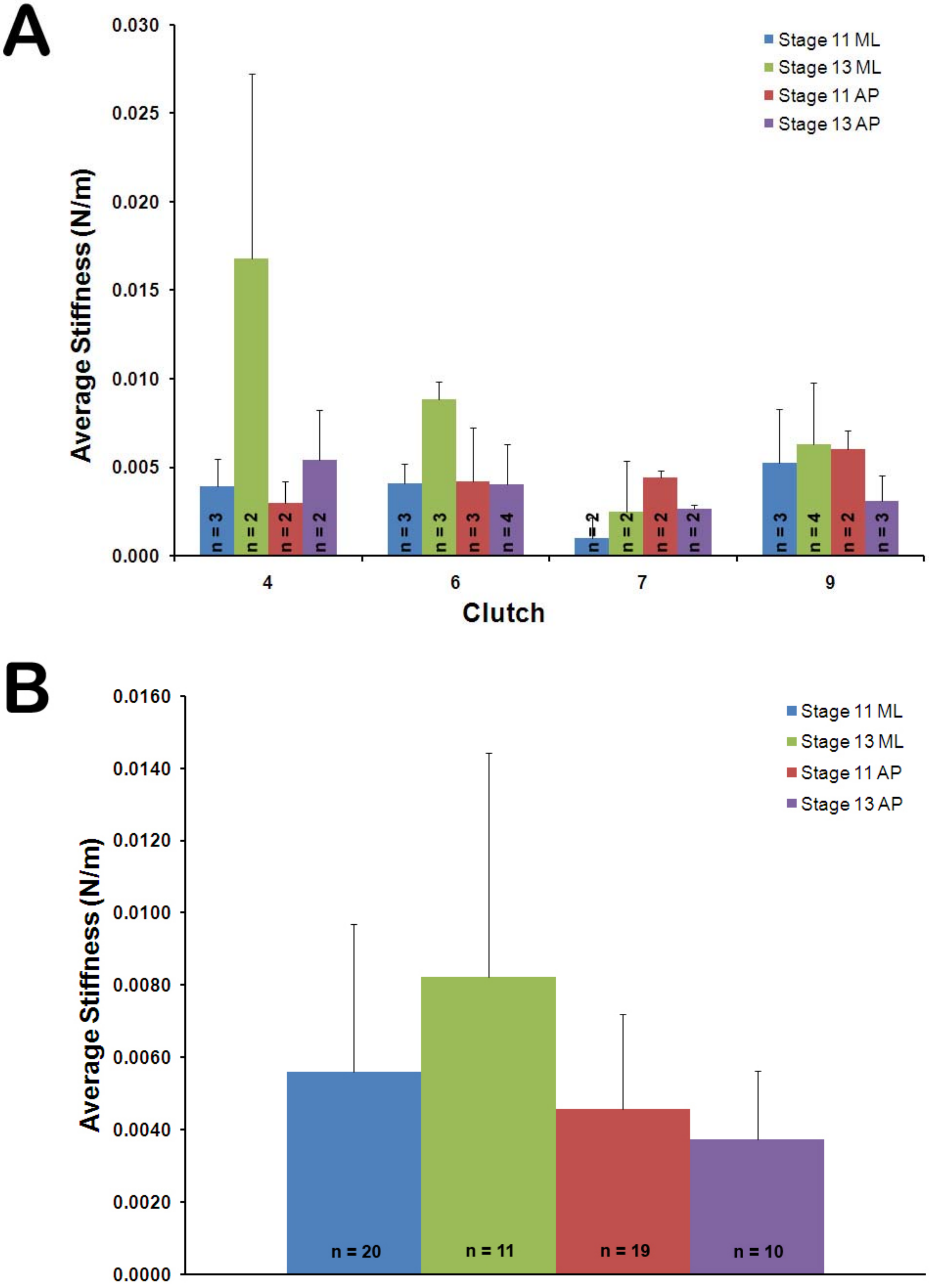
A
Average Stiffness (N/m)
0.030
0.025
0.020
0.015
0.010
0.005
0.000
Stage 11 ML
Stage 13 ML
Stage 11 AP
Stage 13 AP
n = 3
n = 2
n = 2
n = 2
n = 3
n = 3
n = 3
n = 4
n = 2
n = 2
n = 2
n = 2
n = 3
n = 4
n = 2
n = 3
4
6
7
9
Clutch
B
Average Stiffness (N/m)
0.0160
0.0140
0.0120
0.0100
0.0080
0.0060
0.0040
0.0020
0.0000
Stage 11 ML
Stage 13 ML
Stage 11 AP
Stage 13 AP
n = 20
n = 11
n = 19
n = 10

Table A1.3: **Average decrease in stiffness between 45 and 190 seconds of explants at stage 11 and 13 in ML and AP directions by clutch.**

Clutch	Stage	Direction	Average Stiffness (N/m) (Mean ± Standard Deviation)
4	11	ML	0.000259 ± 0.00020
	11	AP	0.000169 ± 0.00020
	13	ML	0.00000365 ± 0.00016
	13	AP	0.000148 ± 0.00024
6	11	ML	0.0000817 ± 0.00014
	11	AP	0.000258 ± 0.00018
	13	ML	0.000202 ± 0.00011
	13	AP	0.000472 ± 0.00033
7	11	ML	0.000389 ± 0.000088
	11	AP	0.000224 ± 0.000081
	13	ML	0.000765 ± 0.00038
	13	AP	0.000464 ± 0.000037
9	11	ML	0.000166 ± 0.00029
	11	AP	-0.0000288 ± 0.000089
	13	ML	0.000274 ± 0.00013
	13	AP	0.000236 ± 0.00024
Average	11	ML	0.000126 ± 0.00022
	11	AP	0.000211 ± 0.00022
	13	ML	0.000295 ± 0.00030
	13	AP	0.000355 ± 0.00026

Figure A1.3: Average decrease in stiffness between 45 and 190 seconds of explants at stage 11 and 13 in ML and AP directions. (A) Decrease in stiffness measured in embryos from clutch 4, 6, 7, and 9 exhibited high variability and demonstrates that the patterns of decay are unpredictable. Decreases in ML stiffness are not significantly different ($P > 0.05$) from stage 11 (blue) to stage 13 (green) embryos in all clutches: 0.000259 ±0.00020 N/m to 0.00000365 ±0.00016 N/m ($P > 0.05$) in clutch 4, 0.0000817 ±0.00014 N/m to 0.000202 ±0.00011 N/m ($P > 0.05$) in clutch 6, 0.000389 ±0.000088 N/m to 0.000765 ±0.00038 N/m ($P > 0.05$) in clutch 7, and 0.000166 ±0.00029 N/m to 0.000274 ±0.00013 N/m ($P > 0.05$) in clutch 9. Similarly, there are no significant differences in decreases in AP stiffness from stage 11 (red) to stage 13 (purple) in all clutches: 0.000169 ±0.00020 N/m to 0.000148 ±0.00024 N/m ($P > 0.05$) in clutch 4, 0.000258 ±0.00018 N/m to 0.000472 ±0.00033 N/m ($P > 0.05$) in clutch 6, 0.000224 ±0.000081 N/m to 0.000464 ±0.000037 N/m ($P > 0.05$) in clutch 7, -0.0000288 ±0.000089 N/m to 0.000236 ±0.00024 N/m ($P > 0.05$) in clutch 9. Error bars represent standard deviation. (B) Averaged data across clutches reveals high variability and no trend to demonstrate that he patterns of decay are erratic. Average ML stiffness changes from 0.000126 ±0.00022 N/m at stage 11 (blue) to 0.000295 ±0.00030 N/m at stage 13 (green) ($P > 0.05$). Average AP stiffness changes from 0.000211 ±0.00022 N/m at stage 11 (red) to 0.000355 ±0.00026 at stage 13 (purple) ($P > 0.05$). Error bars represent standard deviation.

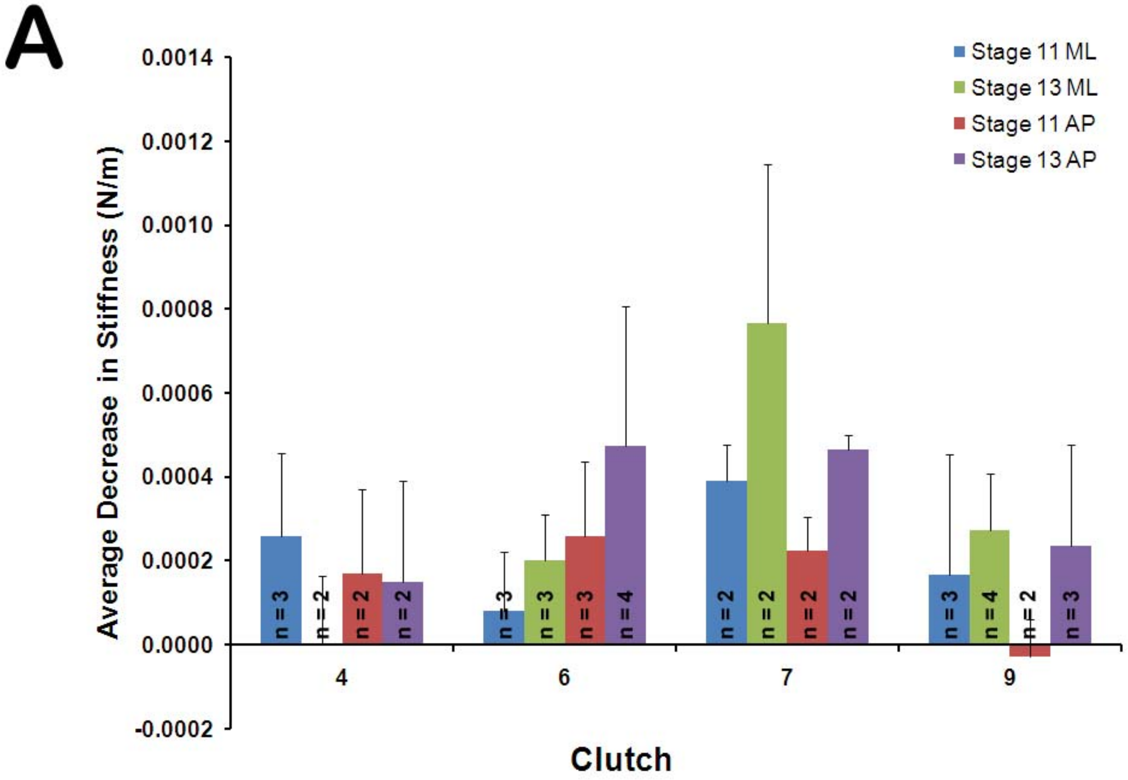
A
0.0014
0.0012
0.0010
0.0008
0.0006
0.0004
0.0002
0.0000
-0.0002
Average Decrease in Stiffness (N/m)
Stage 11 ML
Stage 13 ML
Stage 11 AP
Stage 13 AP
n = 3
n = 2
n = 2
n = 2
n = 3
n = 3
n = 3
n = 4
n = 2
n = 2
n = 2
n = 2
n = 3
n = 4
n = 2
n = 3
4
6
7
9
Clutch

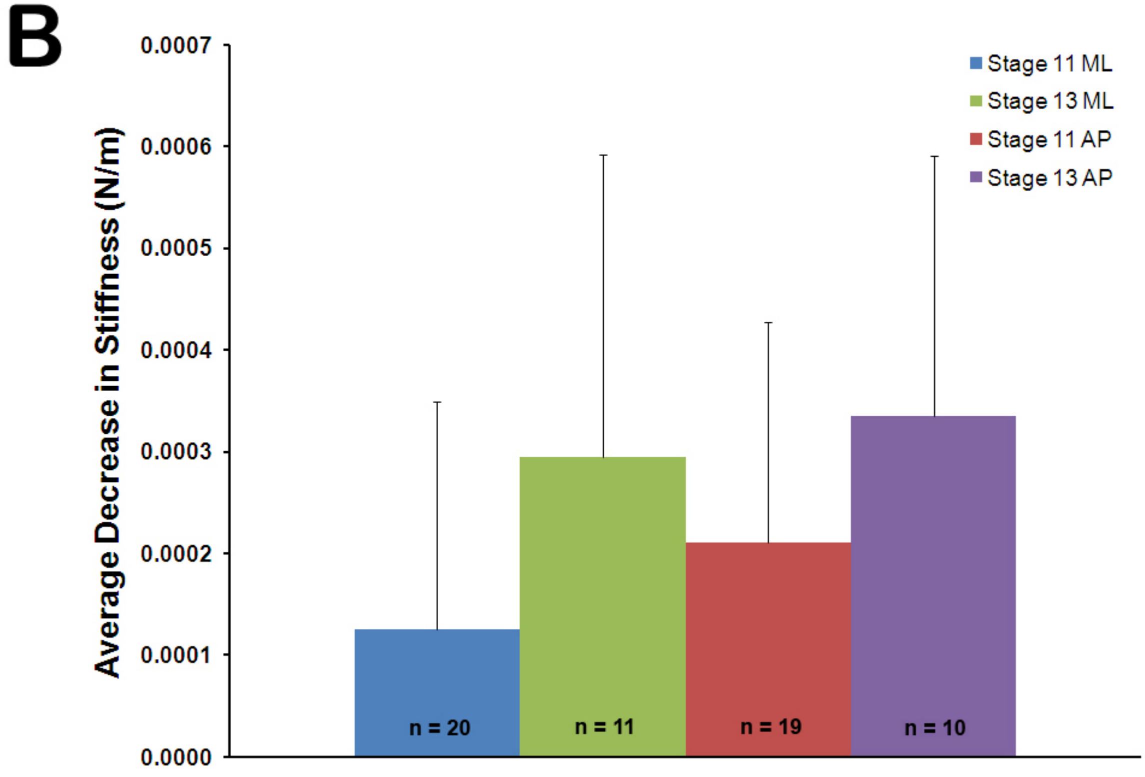
B
0.0007
0.0006
0.0005
0.0004
0.0003
0.0002
0.0001
0.0000
Average Decrease in Stiffness (N/m)
Stage 11 ML
Stage 13 ML
Stage 11 AP
Stage 13 AP
n = 20
n = 11
n = 19
n = 10

Table A2.1: **The effects of a dn*XDsh* construct on tissue stiffness by clutch.**

Clutch	Type	Stage	Direction	Average Stiffness (N/m) (Mean ± Standard Deviation)
11	Control	11	ML	0.00787 ± 0.00050
	Control	11	AP	0.0157 ± 0.0045
	dn*XDsh* injected	11	ML	0.0185 ± 0.0060
	dn*XDsh* injected	11	AP	0.0152 ± 0.0018
12	Control	11	ML	0.0156 ± 0.00091
	Control	11	AP	0.00721 ± 0.0021
	Control	13	ML	0.0216 ± 0.0083
	Control	13	AP	0.0207 ± 0.0034
	dn*XDsh* injected	11	ML	0.0158 ± 0.0050
	dn*XDsh* injected	11	AP	0.0178 ± 0.00082
	dn*XDsh* injected	13	ML	0.0198
	dn*XDsh* injected	13	AP	0.0181
13	Control	13	ML	0.0175 ± 0.0014
	Control	13	AP	0.0155 ± 0.0044
	dn*XDsh* injected	13	ML	0.0130 ± 0.00068
	dn*XDsh* injected	13	AP	0.0111
14	Control	11	ML	0.0158 ± 0.0053
	Control	11	AP	0.0166 ± 0.011
	Control	13	ML	0.0141
	Control	13	AP	0.0203
	dn*XDsh* injected	11	ML	0.0132
	dn*XDsh* injected	11	AP	0.00581
	dn*XDsh* injected	13	ML	0.0164
	dn*XDsh* injected	13	AP	0.00857

Table A2.1 continued on next page →

Average	Control	11	ML	0.0131 ± 0.0047
	Control	11	AP	0.0132 ± 0.0071
	Control	13	ML	0.0184 ± 0.0053
	Control	13	AP	0.0185 ± 0.0039
	dn*XDsh* injected	11	ML	0.0163 ± 0.0045
	dn*XDsh* injected	11	AP	0.0144 ± 0.0051
	dn*XDsh* injected	13	ML	0.0156 ± 0.0033
	dn*XDsh* injected	13	AP	0.0126 ± 0.0049

Figure A2.1: Average stiffness measured from dn*XDsh* injected embryos compared to sibling controls. (A) Average stiffness measured from dn*XDsh* injected embryos compared to sibling controls by clutch. Trends are difficult to determine due to high variation. At stage 11, average stiffness measured: 0.00787 ±0.00050 N/m in ML and 0.0157 ±0.0045 N/m in AP for control embryos, 0.0185 ±0.0060 N/m in ML and 0.0152 ±0.0018 N/m in AP for dn*XDsh* injected embryos of clutch 11; 0.0156 ±0.00091 N/m in ML and 0.00721 ±0.0021 N/m in AP for control embryos, 0.0158 ±0.0050 N/m in ML and 0.0178 ±0.00082 N/m in AP for dn*XDsh* injected embryos of clutch 12; 0.0158 ±0.0053 N/m in ML and 0.0166 ±0.011 N/m in AP for control embryos, 0.0132 N/m in ML and 0.00581 N/m in AP for dn*XDsh* injected embryos of clutch 14. At stage 13 average stiffness measured: 0.0216 ±0.0083 N/m in ML and 0.0207 ±0.0034 N/m in AP for control embryos, 0.0198 N/m in ML and 0.0181 N/m in AP for dn*XDsh* injected embryos of clutch 12; 0.0175 ±0.0014 N/m in ML and 0.0155 ±0.0044 N/m in AP for control embryos, 0.0130 ±0.00068 N/m in ML and 0.0111 N/m in AP for dn*XDsh* injected embryos of clutch 13; 0.0141 N/m in ML and 0.0203 N/m in AP for control embryos, 0.0164 N/m in ML and 0.00857 N/m in AP for dn*XDsh* injected embryos of clutch 14. Error bars represent standard deviation. (B) Average stiffness measured from dn*XDsh* injected embryos compared to sibling controls across clutches. Trends are difficult to determine due to high variability; however, a significant increase in ML stiffness from stage 11 (blue) to stage 13 (green) not exhibited in dn*XDsh* injected embryos, 0.0163 ±0.0045 N/m to 0.0156 ±0.0033 N/m($P > 0.05$), is exhibited in control embryos, 0.0131 ±0.0047 N/m to 0.0184 ±0.0053 N/m ($P < 0.05$). No significant differences are seen in AP stiffness from stage 11 (blue) to stage 13 (green) of control embryos, 0.0132 ±0.0071 N/m to 0.0185 ±0.0039 N/m($P > 0.05$), or of dn*XDsh* injected embryos, 0.0144 ±0.0051 N/m to 0.0126 ±0.0049 N/m ($P > 0.05$). Error bars represent standard deviation and ‘*’ indicates significant differences ($P < 0.05$).

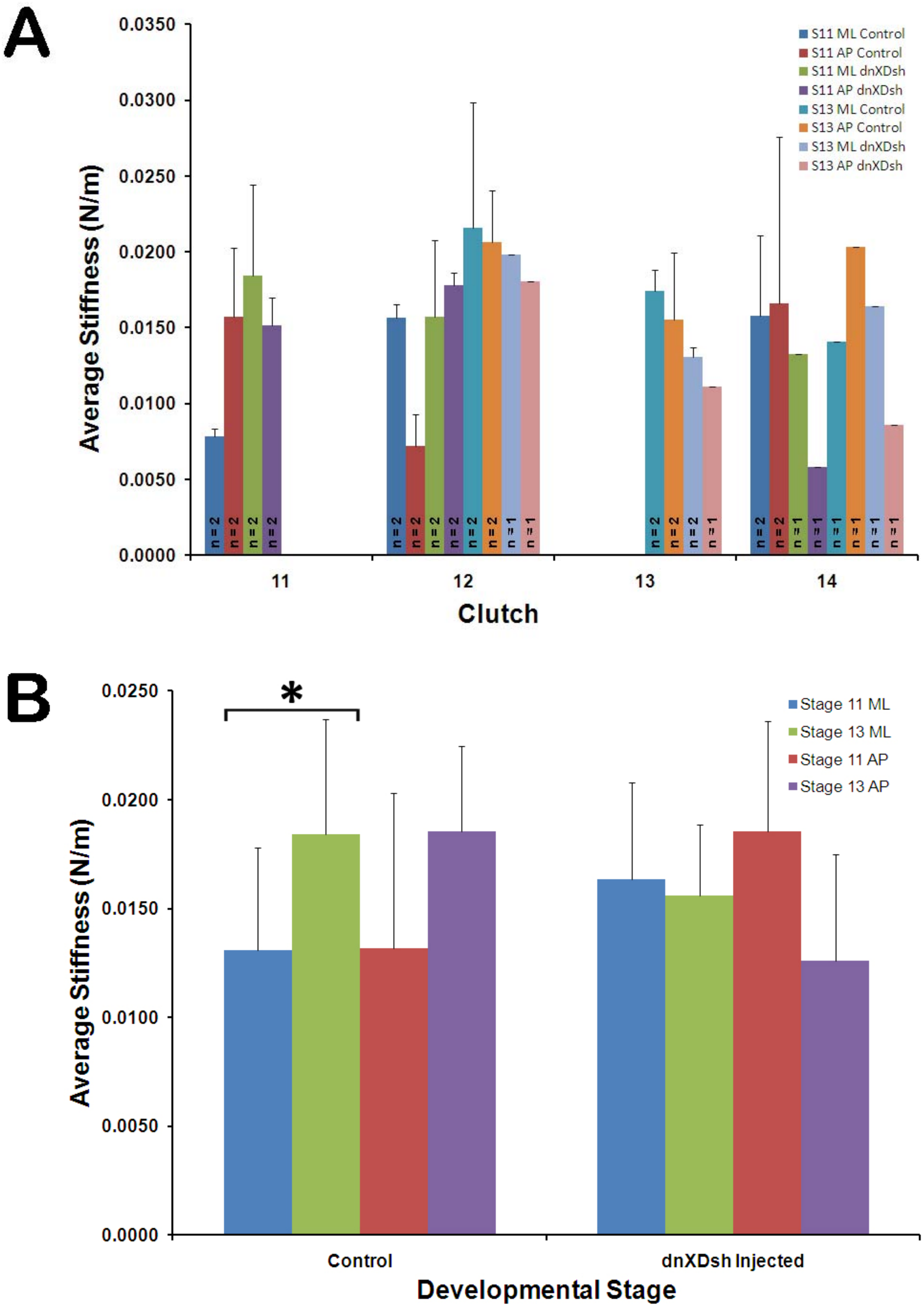
A
0.0350
0.0300
0.0250
0.0200
0.0150
0.0100
0.0050
0.0000
Average Stiffness (N/m)
S11 ML Control
S11 AP Control
S11 ML dnXDsh
S11 AP dnXDsh
S13 ML Control
S13 AP Control
S13 ML dnXDsh
S13 AP dnXDsh
n = 2
n = 1
11
12
13
14
Clutch
B
0.0250
0.0200
0.0150
0.0100
0.0050
0.0000
Average Stiffness (N/m)
*
Stage 11 ML
Stage 13 ML
Stage 11 AP
Stage 13 AP
Control
dnXDsh Injected
Developmental Stage

Table A2.2: The effects of a dn*XFz7* construct on tissue stiffness by clutch.

Clutch	Type	Stage	Direction	Average Stiffness (N/m) (Mean ± Standard Deviation)
16	Control	11	ML	0.0103 ± 0.0051
	Control	11	AP	0.00809 ± 0.0093
	Control	13	ML	0.0168 ± 0.0016
	Control	13	AP	0.0164 ± 0.0016
	dn*XFz7* injected	11	ML	0.00938 ± 0.00085
	dn*XFz7* injected	11	AP	0.00954
	dn*XFz7* injected	13	ML	0.0130
	dn*XFz7* injected	13	AP	0.0128 ± 0.00041
17	Control	11	ML	0.0122 ± 0.0014
	Control	11	AP	0.0135 ± 0.000068
	Control	13	ML	0.0193 ± 0.0037
	Control	13	AP	0.0132 ± 0.0045
	dn*XFz7* injected	11	ML	0.0134 ± 0.00092
	dn*XFz7* injected	11	AP	0.0139 ± 0.0017
	dn*XFz7* injected	13	ML	0.0137 ± 0.010
	dn*XFz7* injected	13	AP	0.0121 ± 0.0057
Average	Control	11	ML	0.0113 ± 0.0032
	Control	11	AP	0.0125 ± 0.0057
	Control	13	ML	0.0180 ± 0.0027
	Control	13	AP	0.0148 ± 0.0033
	dn*XFz7* injected	11	ML	0.0114 ± 0.0024
	dn*XFz7* injected	11	AP	0.0140 ± 0.0039
	dn*XFz7* injected	13	ML	0.0135 ± 0.0074
	dn*XFz7* injected	13	AP	0.0125 ± 0.0033

Figure A2.2: Average stiffness measured from dn*XFz7* injected embryos compared to sibling controls. (A) Average stiffness measured from dn*XFz7* injected embryos compared to sibling controls by clutch. Trends are difficult to determine due to high variation. At stage 11, average stiffness measured: 0.0103 ±0.0051 N/m in ML and 0.00809 ±0.0093 N/m in AP for control embryos, 0.00938 ±0.00085 N/m in ML and 0.00954 N/m in AP for dn*XFz7* injected embryos of clutch 16; 0.0122 ±0.0014 N/m in ML and 0.0135 ±0.000068 N/m in AP for control embryos, 0.0134 ±0.00092 N/m in ML and 0.0139 ±0.0017 N/m dn*XFz7* injected embryos of clutch 17. At stage 13, average stiffness measured: 0.0168 ±0.0016 N/m in ML and 0.0164 ±0.0016 N/m in AP for control embryos, 0.0130 N/m in ML and 0.0128 ±0.00041 N/m in AP for dn*XFz7* injected embryos of clutch 16; 0.0193 ±0.0037 N/m in ML and 0.0132 ±0.0045 N/m in AP for control embryos, 0.0137 ±0.010 N/m in ML and 0.0121 ±0.0057 N/m in AP for dn*XFz7* injected embryos of clutch 17. Error bars represent standard deviation. (B) Average stiffness measured from dn*XFz7* injected embryos compared to sibling controls across clutches. Trends are difficult to determine due to high variability; however, a significant increase in ML stiffness from stage 11 (blue) to stage 13 (green) not exhibited in dn*XFz7* injected embryos, 0.0114 ±0.0024 N/m to 0.0135 ±0.0074 N/m($P > 0.05$), is exhibited in control embryos, 0.0113 ±0.0032 N/m to 0.0180 ±0.0027 ($P < 0.05$). No significant differences are seen in AP stiffness from stage 11 (blue) to stage 13 (green) of control embryos, 0.0125 ±0.0057 N/m to 0.0148 ±0.0033 N/m($P > 0.05$), or of dn*XFz7* injected embryos, 0.0140 ±0.0039 N/m to 0.0125 ±0.0033 N/m ($P > 0.05$). Error bars represent standard deviation and '*' indicates significant differences ($P < 0.05$).

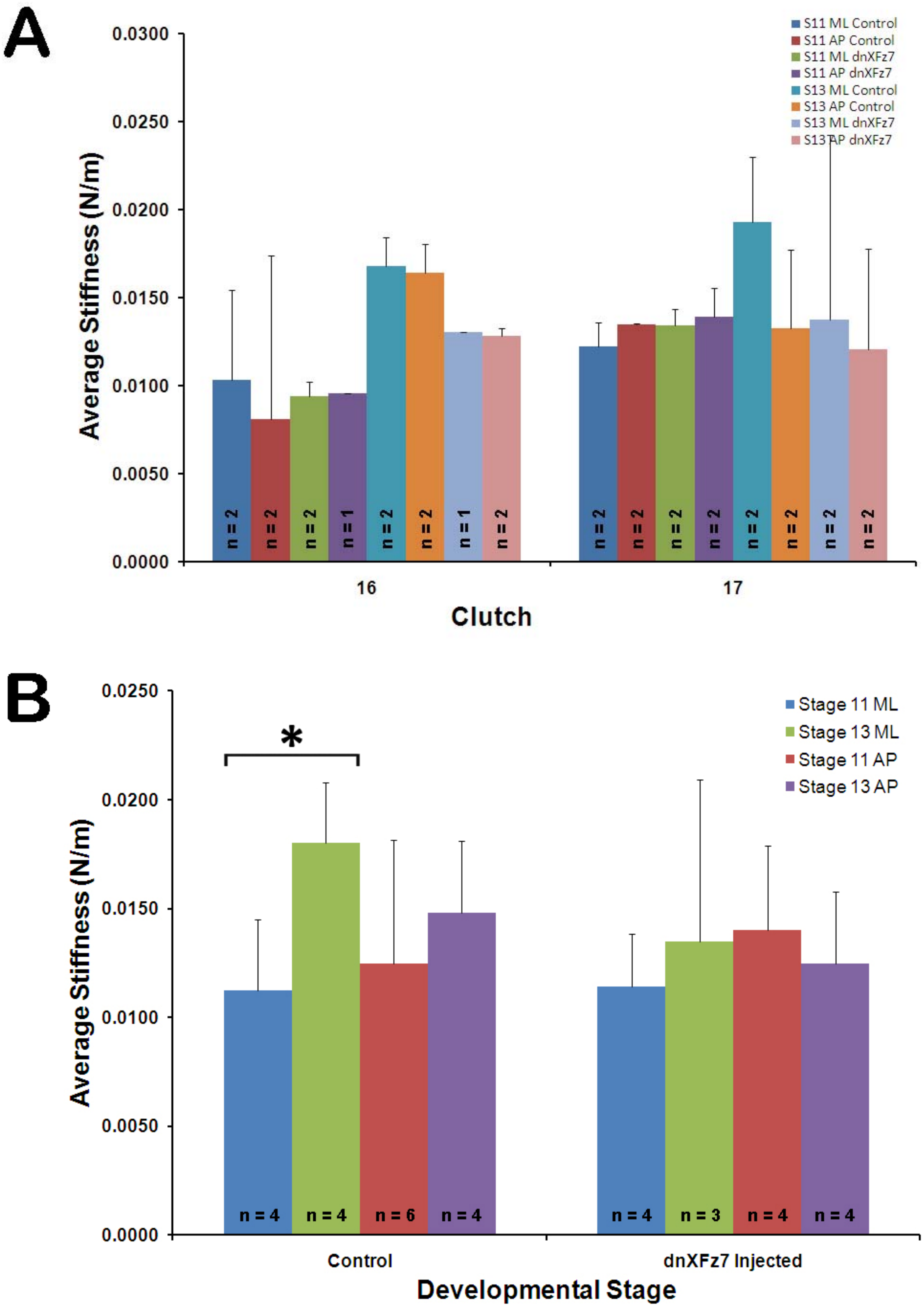
A
Average Stiffness (N/m)
0.0300
0.0250
0.0200
0.0150
0.0100
0.0050
0.0000
S11 ML Control
S11 AP Control
S11 ML dnXFz7
S11 AP dnXFz7
S13 ML Control
S13 AP Control
S13 ML dnXFz7
S13 AP dnXFz7
n = 2
n = 2
n = 2
n = 1
n = 2
n = 2
n = 1
n = 2
n = 2
n = 2
n = 2
n = 2
n = 2
n = 2
n = 2
n = 2
16
17
Clutch
B
Average Stiffness (N/m)
0.0250
0.0200
0.0150
0.0100
0.0050
0.0000
*
Stage 11 ML
Stage 13 ML
Stage 11 AP
Stage 13 AP
n = 4
n = 4
n = 6
n = 4
n = 4
n = 3
n = 4
n = 4
Control
dnXFz7 Injected
Developmental Stage

Table A2.3: The effects of a dn*XWnt11* construct on tissue stiffness by clutch.

Clutch	Type	Stage	Direction	Average Stiffness (N/m) (Mean ± Standard Deviation)
18	Control	11	ML	0.00994
	Control	11	AP	0.0199
	dn*XWnt11* injected	11	ML	0.0143 ± 0.0024
	dn*XWnt11* injected	11	AP	0.0139 ± 0.0075
19	Control	11	ML	0.00573 ± 0.0013
	Control	11	AP	0.00959 ± 0.00072
	Control	13	ML	0.0200 ± 0.0055
	Control	13	AP	0.0174 ± 0.0098
	dn*XWnt11* injected	11	ML	0.0169 ± 0.0026
	dn*XWnt11* injected	11	AP	0.0179 ± 0.0067
	dn*XWnt11* injected	13	ML	0.0159 ± 0.0028
	dn*XWnt11* injected	13	AP	0.0170 ± 0.0086
Average	Control	11	ML	0.0071 ± 0.0026
	Control	11	AP	0.0130 ± 0.0060
	Control	13	ML	0.0200 ± 0.0055
	Control	13	AP	0.0174 ± 0.0098
	dn*XWnt11* injected	11	ML	0.0156 ± 0.0026
	dn*XWnt11* injected	11	AP	0.0159 ± 0.0063
	dn*XWnt11* injected	13	ML	0.0159 ± 0.0028
	dn*XWnt11* injected	13	AP	0.0170 ± 0.0086

Figure A2.3: Average stiffness measured from dn*XWnt11* injected embryos compared to sibling controls. (A) Average stiffness measured from dn*XWnt11* injected embryos compared to sibling controls by clutch. Trends are difficult to determine due to high variation. At stage 11, average stiffness measured: 0.00994 N/m in ML and 0.0199 N/m in AP for control embryos, 0.0143 ±0.0024 N/m in ML and 0.0139 ±0.0075 N/m in AP for dn*XWnt11*injected embryos of clutch 18; 0.00573 ±0.0013 N/m in ML and 0.00959 ±0.00072 N/m in AP for control embryos, 0.0169 ±0.0026 N/m in ML and 0.0179 ±0.0067 N/m dn*XWtn11* injected embryos of clutch 19. At stage 13, average stiffness measured: 0.0200 ±0.0055 N/m in ML and 0.0174 ±0.0098 N/m in AP for control embryos, 0.0159 ±0.0028 N/m in ML and 0.0170 ±0.0086 N/m dnX*Wtn11* injected embryos of clutch 19. Error bars represent standard deviation. (B) Average stiffness measured from dn*XWnt11* injected embryos compared to sibling controls across clutches. Trends are difficult to determine due to high variability. There are no significant differences in ML stiffness from stage 11 (blue) to stage 13 (green) of control embryos, 0.0071 ±0.0026 N/m to 0.0200 ±0.0055 N/m($P > 0.05$), or of dn*XWnt11* injected embryos, 0.0156 ±0.0026 N/m to 0.0159 ±0.0028 N/m ($P > 0.05$). No significant differences are seen in AP stiffness from stage 11 (blue) to stage 13 (green) of control embryos, 0.0130 ±0.0060 N/m to 0.0174 ±0.0098 N/m($P > 0.05$), or of dn*XWnt11* injected embryos, 0.0159 ±0.0063 N/m to 0.0170 ±0.0086 N/m ($P > 0.05$). Error bars represent standard deviation.

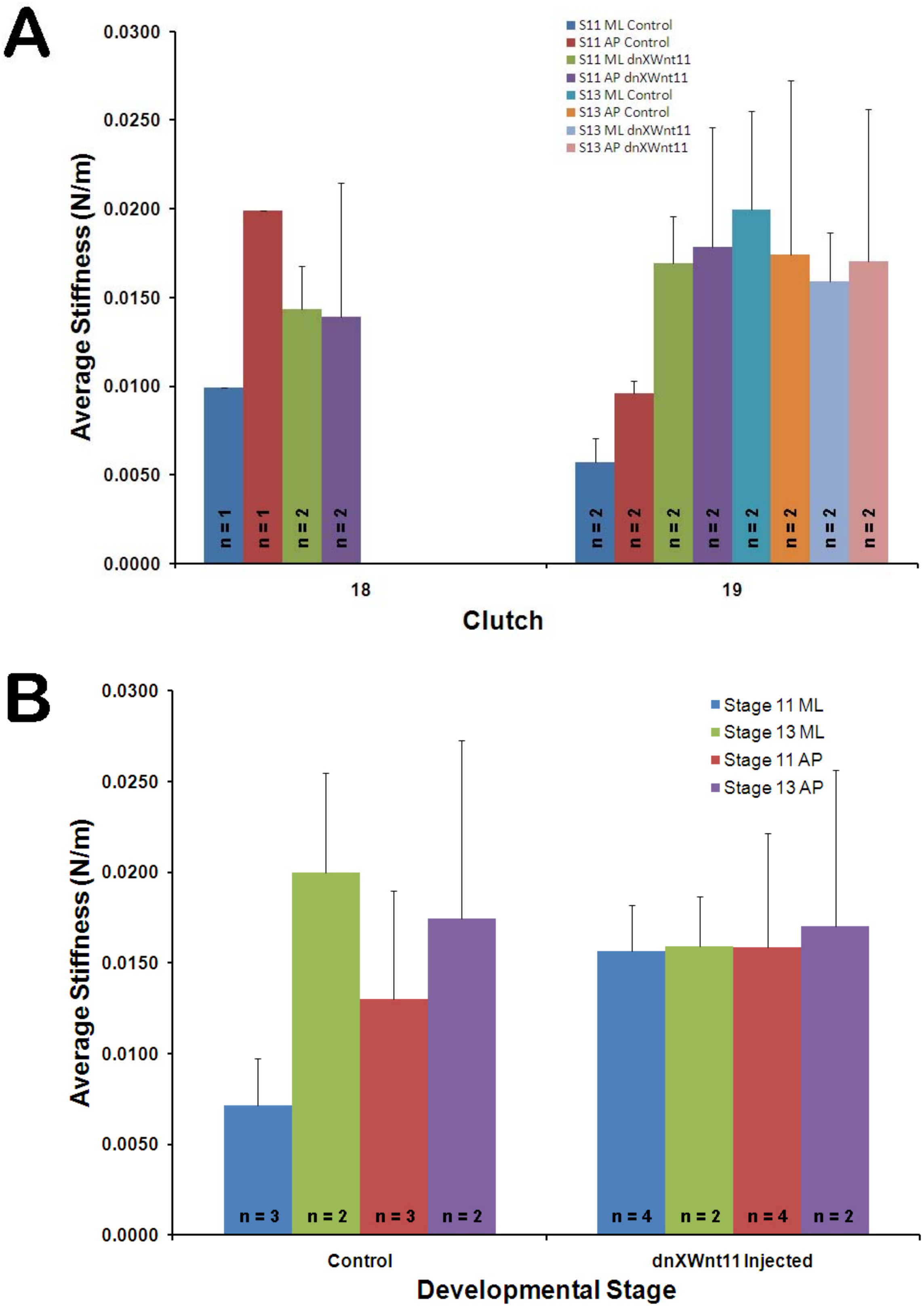
A
Average Stiffness (N/m)
0.0300
0.0250
0.0200
0.0150
0.0100
0.0050
0.0000
🟦 S11 ML Control
🟥 S11 AP Control
🟩 S11 ML dnXWnt11
🟪 S11 AP dnXWnt11
S13 ML Control
S13 AP Control
S13 ML dnXWnt11
S13 AP dnXWnt11
n = 1
n = 1
n = 2
n = 2
n = 2
n = 2
n = 2
n = 2
n = 2
n = 2
n = 2
n = 2
18
19
Clutch
B
Average Stiffness (N/m)
0.0300
0.0250
0.0200
0.0150
0.0100
0.0050
0.0000
🟦 Stage 11 ML
🟩 Stage 13 ML
🟥 Stage 11 AP
🟪 Stage 13 AP
n = 3
n = 2
n = 3
n = 2
n = 4
n = 2
n = 4
n = 2
Control
dnXWnt11 Injected
Developmental Stage

References

Barmchi, M.P., Rogers, S., and Häcker, U. (2005) DRhoGEF2 regulates actin organization and contractility in the *Drosophila* blastoderm embryo. *The Journal of Cell Biology* 168, 575-585

Bhanot, P., Brink, M., Samos, C.H., Hsieh, J.C., Wang, Y., Macke, J.P., Andrew, D., Nathans, J., and Nusse, R., (1996) A new member of the frizzled family from Drosophila functions as a Wingless receptor. *Nature* 382, 225-230

Brieher, B. and Gumbiner, B. (1994) Regulation of C-cadherin function during activin induced morphogenesis of *Xenopus* animal caps. *Journal of Cell Biology* 126, 519-527

Brodland, G.W. (2002) The Differential Interfacial Tension hypothesis (DITH): A Comprehensive Theory for Self-Rearrangement of Embryonic Cells and Tissues. *ASME Journal of Biomechanical Engineering* 124, 188-197

Brodland, G.W. (2006) Do lamellipodia have the mechanical capacity to drive convergent extension? *International Journal of Developmental Biology* 50, 151-155

Brodland, G.W. and Veldhuis, J.H. (2006) Lamellipodium-driven tissue reshaping: a parametric study *Computer Methods in Biomechanics and Biomedical Engineering* 9, 17-23

Brouns, M.R., Matheson, S.F., Hu, K., Delalle, I., Caviness, V.S., Silver, J.J., Bronson, T., and Settleman, J. (2000) The adhesion signaling molecule p190 RhoGAP is required for morphogenetic processes in neural development. *Development* 127, 4891-4903

Davidson, L.A. and Keller, R.E. (1999) Neural tube closure in *Xenopus laevis* involves medial migration, directed protrusive activity, cell intercalation and convergent extension. *Development* 126, 4547-4556

Djiane, A., Riou, J., Umbhauer, M., Boucaut, J., and Shi, D. (2000) Role of *frizzled 7* in the regulation of convergent extension movements during gastrulation in *Xenopus laevis*. *Development* 127, 3091-3100

Dzamba, B.J., Jakab, K.R., Marsden, M., Schwartz, M.A., and DeSimone, D.W. (2009) Cadherin adhesion, tissue tension, and noncanonical Wnt signaling regulate fibronectin matrix organization. *Developmental Cell* 16(3), 421-32

Elul, T. and Keller, R. E. (2000) Monopolar protrusive activity: A new morphogenic cell behavior in the neural plate dependent on vertical interactions with the mesoderm in *Xenopus*. *Developmental Biology* 224, 3-19

Ezin, A.M., Skoglund, P., and Keller, R.E. (2003) The midline (notochord and notoplate) patterns the cell motility underlying convergent extension of the *Xenopus* neural plate. *Developmental Biology* 256, 100-113

Ezin, A.M., Skoglund, P., and Keller, R.E. (2006) The presumptive floor plate (notoplate) induces behaviours associated with convergent extension in medial but not lateral neural plate cells of *Xenopus*. *Developmental Biology* 300, 670–686

Fanto, M., Weber, U., Strutt, D.I. and Mlodzik, M. (2000) Nuclear signaling by Rac and Rho GTPases is required in the establishment of epithelial planar polarity in the Drosophila eye. *Current Biology* 10, 979-988

Fanto, M. and McNeill, H. (2004) Planar polarity from flies to vertebrates. *Journal of Cell Science* 117, 527-533

Foty, R.A. and Steinberg, M.S. (2005). The differential adhesion hypothesis: a direct evaluation. *Developmental Biology* 278, 255-263

Franke, J., Montague, R., and Kiehart, D.P. (2005) Nonmuscle myosin II generates forces that transmit tension and drive contraction of multiple tissues during dorsal closure. *Current Biology 15*, 2208-2221

Fukata, M. and Kaibuchi, K. (2001) RHO-family GTPases in cadherin-mediated cell-cell adhesion. *Nature Reviews* 2, 887-897

Gardel, M.L., Nakamura, F., Hartwig, J.H., Crocker, J.C., Stossel, T.P., and

Weitz, D.A. (2006) Prestressed F-actin networks cross-linked by hinged filamins replicate mechanical properties of cells. *Proceedings of National Academy of Science* 103**,** 1762-1767

Habas, R., Kato, Y. and He, X. (2001) Wnt/Frizzled activation of Rho regulates vertebrate gastrulation and requires a novel Formin homology protein Daam1. *Cell* 107, 843-854

Habas, R., Dawid, I.B. and He, X. (2003) Coactivation of Rac and Rho by Wnt/Frizzled signaling is required for vertebrate gastrulation. *Genes and Development* 17, 295-309

Haigo, S.L., Hildebrand, J.D., Harland, R.M., Wallingford, J.B. (2003) Shroom induces apical constriction and is required for hingepoint formation during neural tube closure. *Current Biology* 13, 2125-2137

Itoh, I., Brott, B.K., Bae, G.U., Ratcliffe, M.J. and Sokol, S. (2005) Nuclear localization is required for Dishevelled function in Wnt/β-catenin signaling. *Journal of Biology.* 4, 3

Keller, R.E. and Danilchik, M. (1988) Regional expression, pattern and timing of convergence and extension during gastrulation of *Xenopus laevis*. *Development* 103, 193-209

Keller, R.E., Poznanski, A., Elul, T. (1999) Experimental embryological methods for analysis of neural induction in the Amphibian. *Methods in Molecular Biology* 97, 351-392

Keller, R.E., Davidson, L.A., and Shook, D.R. (2003) How we are shaped: The biomechanics of gastrulation. *Differentiation* 71, 171-205

Keller, R.E., Shook, D., Skoglund, P. (2008) The forces that shape embryos: physical aspects of convergent extension by cell intercalation. *Physical Biology* 5, 15007 (23pp)

Kinoshita, N., Sasai, N., Misaki, K., and Yonemura, S. (2008) Apical accumulation of Rho in the neural plate is important for neural plate cell shape change and neural tube formation. *Molecular Biology of the Cell* 19, 2289-2299

Krieg, M., Arboleda-Estudillo, Y., Puech, P.H., Kafer, J., Graner, F., Muller, D.J., and Heisenberg, C.P. (2008). Tensile forces govern germ-layer organization in zebrafish. *Nature Cell Biology* 10, 429-436

Kwan, K.M. and Kirschner, M.W. (2003) *Xbra* functions as a switch between cell migration and convergent extension in the *Xenopus* gastrula. *Development* 130, 1961-1972

Kolsch, V., Seher, T., Fernandez-Ballester, G.J., Serrano, L., Leptin, M. (2007) Control of *Drosophila* gastrulation by apical localization of adherens junctions and RhoGEF2. *Science* 315 (5810), 384-386

Lawson, A., Anderson, H., Schoenwolf, G.C. (2001) Cellular mechanisms of neural fold formation and morphogenesis in the chick embryo. *The Anatomical Record* 262, 153-168

Logan, C.Y. and Nusse, R. (2004) The Wnt signaling pathway in development and disease. *Annual Review of Cell and Developmental Biology* 20, 781-810

Malacinski, G.M., and Youn, B.W. (1981) Neural plate morphogenesis and axial stretching in "notochord-defective" *Xenopus laevis* embryos. *Developmental Biology* 88, 352-357

Marsden, M. and DeSimine, D.W. (2001) Regulation of cell polarity, radial intercalation and epiboly in *Xenopus*: Novel roles for integrin and fibronectin. *Development* 128, 3635-3647

Miller, J.R., Hocking, A.M., Brown, J.D., and Moon, R.T. (1999a) Mechanism and function of signal transduction by the Wnt/*β*-catenin and Wnt/Ca^{2+} pathways. *Oncogene* 18, 7860-7872

Miller, J.R., Rowning, Brian, A., Larabell, C.A., Yang-Snyder, J.A., Bates, R.L., and Moon, R.T. (1999b) Establishment of the dorsal-ventral axis in *Xenopus* embryos coincides with the dorsal enrichment of Dishevelled that is dependent on cortical rotation. *The Journal of Cell Biology* 146, 427-437

Moore, S.W. (1994) A fiber optic system for measuring dynamic mechanical properties of embryonic tissues. IEEE *Transaction in Biomedical Engineering* 41, 45-50

Moore, S.W., Keller, R.E., and Koehl, M.A.R. (1995) The dorsal involuting marginal zone stiffens anisotropically during its convergent extension in the gastrula of *Xenopus leavis*. *Development* 121, 3130-40

Ninomiya, H. and Winklbauer, R. (2008) Epithelial coating controls mesenchymal shape change through tissue-positioning effects and reduction of surface-minimizing tension. *Nature Cell Biology*. 10, 61-69

Rolo, A., Skoglund, P., and Keller R.E. (2009) Morphogenetic movements driving neural tube closure in *Xenopus* require myosin IIB. *Developmental Biology* 327, 237-338

Roszko, I., Sawada, A., and Solnica-Krezel, L. (2009) Regulation of convergence and extension movements during vertebrate gastrulation by the Wnt/PCP pathway. *Seminars in Cell and Developmental Biology* 20(8), 986-997

Sater, A.K., Steinhardt, R.A. and Keller, R.E. (1993) Induction of Neuronal Differentiation by Planar signals in Xenopus embryos. *Developmental Dynamics* 197, 268–280

Skoglund, P., Rolo, A., Chen, X., Grmbiner, B.M., and Keller, R.E. (2008) Convergence and extension at gastrulation require a myosin IIB-dependent cortical actin network. *Development* 135, 2435-2445

Shih, J. and Keller, R.E. (1992) Patterns of cell motility in the organizer and dorsal mesoderm of *Xenopus laevis*. *Development* 116, 915-930

Sive, H. (1996) Early development of *Xenopus laevis*; Course Manual. Cold Spring Harbor Laboratory Press, Cold Spring Harbor

Smith, J.L. and Schoenwolf, G. C. (1988) Role of cell cycle in regulating neuroepithelial cell shape during bending of the chick neural plate. *Cell and Tissue Research* 252, 491-500

Sumanas, S., Strege, P., Heasman, J. and Ekker, S.C. (2000). The putative Wnt receptor *Xenopus* frizzled-7 functions upstream of b-catenin in vertebrate dorsoventral mesoderm patterning. *Development* 127, 1981-1990

Tada, M. and Smith, J.C. (2000) *Xwnt11* is a target of *Xenopus Brachyury*: regulation of gastrulation movements via Dishevelled, but not through the canonical Wnt pathway. *Development* 127, 2227-2238.

Turner, C.M. and Adler, P.N. (1995) Morphogenesis of *Drosophila* pupal wings in vitro. *Mechanisms of Development* 52, 247-255

Trinkaus, J.P. (1984) Cells into Organs: Forces that Shape the Embryo. Prentice-Hall, Englewood Cliffs, NJ

Vincent, J.V. (1990) Structural biomaterials. Princeton: Princeton University Press.

von Dassow, M. and Davidson, L.A. (2007) Natural variation in embryo mechanics: Gastrulation in *Xenopus laevis* is highly robust to variation in tissue stiffness. *Birth Defects Research (Part C)* 81, 253-269

von Dassow, M. and Davidson, L.A. (2009) Natural variation in embryo mechanics: Gastrulation in *Xenopus laevis* is highly robust to variation in tissue stiffness. *Developmental Dynamics* 238, 2-18

Wallingford, J.B. and Harland, R.M. (2001) Xenopus dishevelled signaling regulates both neural and mesodermal convergent extension: Parallel forces elongating the body axis. *Development* 128, 2581-2592

Wallingford, J.B. and Harland, R.M. (2002) Convergent extension: The molecular control of polarized cell movement during embryonic development. *Developmental Cell* 2, 695-706

Wallingford, J.B. Fraser, S.E., and Harland, R.M. (2002) Convergent extension: the molecular control of polarized cell movement during embryonic development. *Deelopmental Cell* 2, 695-706.

Wallingford, J.B. (2005) Neural Tube Closure and Neural Tube Defects: Studies in Animal Models Reveal Known Knowns and Known Unknowns. *American Journal of Medical Genetics (Part C)* 135C, 59-68

Wallingford, J.B. and Habas, R. (2005) The developmental biology of dishevelled: An enigmatic protein governing cell fate and cell polarity. *Development* 132, 4421-4436

Wiebe, C. and Brodland, G.W. (2005) Tensile properties of embryonic epithelia measured using a novel instrument. *Journal of Biomechanics* 38, 2087-2094

Wong, L.L. and Adler, P.N. (1993) Tissue polarity genes of *Drosophila* regulate the subcellular location for prehair initiation in pupal wing cells. *The Journal of Cell Biology* 123, 209-221

Wong, H.C., Mao, J., Nguyen, J.T., Srinivas, S., Zhang, W., Liu, B., Li, L., Wu, D. and Zheng, J. (2000) Structural basis of the recognition of the dishevelled DEP domain in the Wnt signaling pathway. *Nat. Journal of Structural Biology* 7, 1178-1184

Yang-Snyder, J., Miller, J.R., Brown, J.D., Lai, C.J., and Moon, R.T. (1996) A frizzled homolog functions in a vertebrate Wnt signaling pathway. *Current Biology* 6, 1302-1306.

Youn, B.W. and Malacinski, G.M. (1981) Axial structure development in ultraviolet-irradiated (notochord-defective) amphibian embryos. *Developmental Biology* 83, 339-352

Zhou, J., Kim, H.Y., Davidson, L. (2009) Actomyosin stiffens the vertebrate embryo during crucial stages of elongation and neural tube closure. *Development* 136, 677-688

Zhong, Y., Brieher, W.M., and Gumbiner, B.M. (1999) Analysis of C-cadherin regulation during tissue morphogenesis with anactivating antibody. *The Journal of Cell Biology* 144, 351-359